Åbo Akademi

Anni Määttänen

PRINTED PLATFORMS FOR PAPER-BASED ANALYTICAL APPLICATIONS

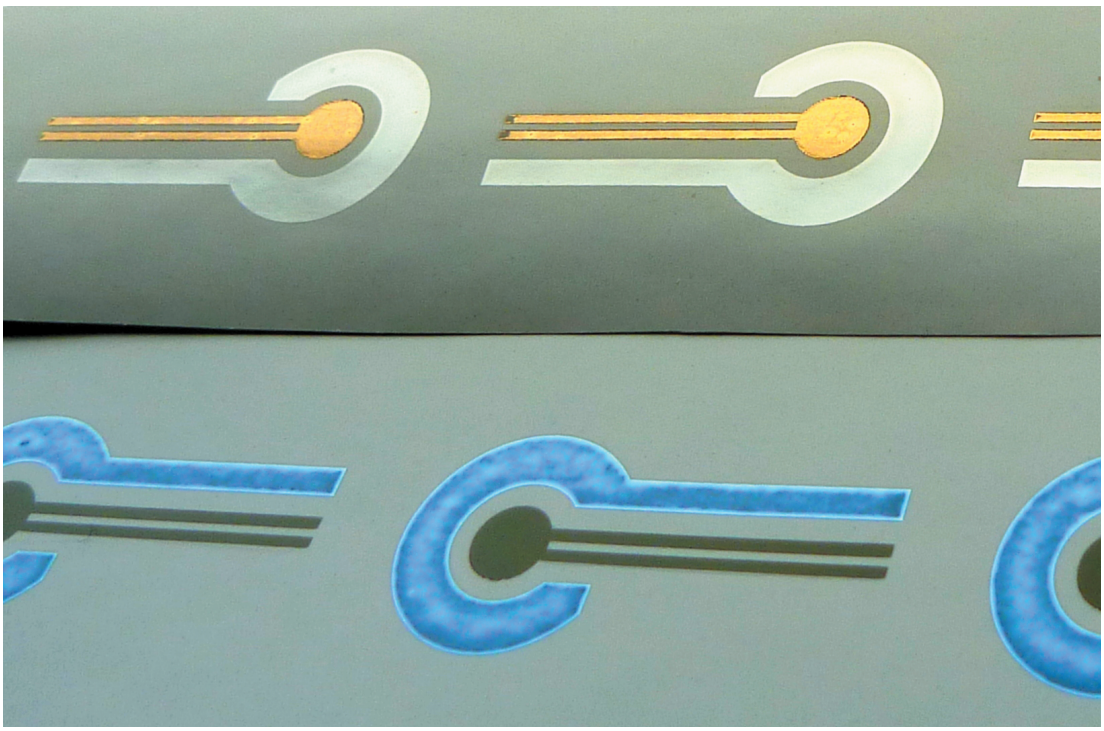

Anni Kaarina Määttänen

Born 1980 in Turku, Finland

Obtained her M.Sc. degree at
the University of Turku in 2007.
Joined the Laboratory of
Physical Chemistry in 2005.

PRINTED PLATFORMS FOR PAPER-BASED ANALYTICAL APPLICATIONS

Anni Määttänen

Laboratory of Physical Chemistry

Åbo Akademi University
Turku, Finland
2014

Supervised by

Professor Jouko Peltonen
Laboratory of Physical Chemistry
Åbo Akademi University, Turku, Finland

Co-supervised by

Dr. Petri Ihalainen
Laboratory of Physical Chemistry
Åbo Akademi University, Turku, Finland

Reviewed by

Professor Daniel Citterio
Department of Applied Chemistry
Keio University, Yokohama, Japan

and

Professor Hans-Erik Nilsson
Department of Electronics Design
Mid Sweden University, Sundsvall, Sweden

Opponent

Professor Daniel Citterio
Department of Applied Chemistry
Keio University, Yokohama, Japan

ISBN 978-952-12-3119-3
Painosalama Oy – Turku, Finland 2014

"A smile is a curve that sets everything straight"

Phyllis Diller

PREFACE

This Ph.D. Thesis is based on research carried out at the Laboratory of Physical Chemistry and Laboratory of Paper Coating and Converting of Åbo Akademi University. Many talented people have been involved in the work leading to my PhD thesis. I would like to acknowledge everyone for their contributions.

I am especially thankful for my supervisor Prof. Jouko Peltonen for hiring me, first as a summer & project worker, and later on after finishing my M.Sc. studies, as a PhD student. I am grateful for all the support and for the privilege I have had to work in the FunMat CoE project as well as in many other projects although they might have not always been directly linked to the topic of this thesis. I really appreciate the chances I got to attend conferences around the world, as far as in Canada and Mexico.

I wish to thank Dr. Petri Ihalainen for the excellent supervision and for the helpful discussions over the years as well as for sharing your expertise with me. It was a pleasure to plan and conduct experiments with you.

All the work done in groups be it in the lab or in a form of email conversations during a struggle to get a manuscript accepted, are the most memorable times. Thank you M.Sc. Ulriika Vanamo for the "Hurraa data" and times we spent at the Analytical Chemistry lab. I wish to thank M.Sc. Daniela Fors, Dr. Shaoxia Wang and M.Sc. Dimitar Valtakari for the productive co-operation and for all your help in many occasions.

Dr. Adyary Fallarero, Janni Kujala, Dr. Malena Skogman, Prof. Pia Vuorela et al., it was really exciting to characterize the living bacterial biofilms, my warmest thanks to you all for the pleasurable collaboration.

I wish to thank Dr. Petri Pulkkinen and Prof. Heikki Tenhu. I truly appreciate the precious and high quality gold nanoparticles you provided

for us. I wish to thank Dr. Roger Bollström for the co-operations and for your contributions to this work. I wish to thank M.Sc. Helka Juvonen for all the co-operations and for the investigations you carried out with the paper-based reaction arrays and biological samples.

I wish to express my thanks to Prof. Johan Bobacka, Dr. Himadri Majumdar, Prof. Ronald Österbacka, Prof. Martti Toivakka and all the co-authors of the supporting articles. Heartfelt thanks to the entire personnel at the Laboratory of Physical Chemistry and Laboratory of Paper Coating and Converting for creating a great working atmosphere.

The Academy of Finland and Tekes are acknowledged for financial support.

Reviewers Prof. Daniel Citterio and Prof. Hans-Erik Nilsson are thanked for their valuable suggestions for improving the thesis.

A sincere thank you and appreciation to all my friends and relatives for all the fun times together and for the help and encouragement you have given me.

Finally I would like to give my special thanks to my lovely parents and dear brother for always believing in me and being behind me in what I choose to do.

Turku, September 9, 2014

Anni Määttänen

CONTENTS

ABSTRACT

Paper-based analytical technologies enable quantitative and rapid analysis of analytes from various application areas including healthcare, environmental monitoring and food safety. Because paper is a planar, flexible and light weight substrate, the devices can be transported and disposed easily. Diagnostic devices are especially valuable in resource-limited environments where diagnosis as well as monitoring of therapy can be made even without electricity by using e.g. colorimetric assays. On the other hand, platforms including printed electrodes can be coupled with hand-held readers. They enable electrochemical detection with improved reliability, sensitivity and selectivity compared with colorimetric assays.

In this thesis, different roll-to-roll compatible printing technologies were utilized for the fabrication of low-cost paper-based sensor platforms. The platforms intended for colorimetric assays and microfluidics were fabricated by patterning the paper substrates with hydrophobic vinyl substituted polydimethylsiloxane (PDMS) -based ink. Depending on the barrier properties of the substrate, the ink either penetrates into the paper structure creating e.g. microfluidic channel structures or remains on the surface creating a 2D analog of a microplate. The printed PDMS can be cured by a roll-ro-roll compatible infrared (IR) sintering method. The performance of these platforms was studied by printing glucose oxidase -based ink on the PDMS-free reaction areas. The subsequent application of the glucose analyte changed the colour of the white reaction area to purple with the colour density and intensity depending on the concentration of the glucose solution.

Printed electrochemical cell platforms were fabricated on paper substrates with appropriate barrier properties by inkjet-printing metal nanoparticle based inks and by IR sintering them into conducting electrodes. Printed PDMS arrays were used for directing the liquid analyte onto the predetermined spots on the electrodes. Various electrochemical measurements were carried out both with the bare electrodes and electrodes functionalized with e.g. self assembled monolayers. Electrochemical glucose sensor was selected as a proof-of-concept device to demonstrate the potential of the printed electronic platforms.

SVENSK SAMMANFATTNING

Papperbaserade analysteknologier möjliggör en kvantitativ och snabb analys av analyter i många applikationer inom användningsområden såsom hälsovård och miljöövervakning. Kolorimetriska tester är speciellt värdefulla i miljöer med begränsade resurser, emedan de möjliggör att t.ex. diagnosoch terapikontroll kan genomföras utan elektricitet. Dessa lätta pappersbaserade testunderlag kan enkelt transporteras och förfogas efter användning för att t.ex. förhindra spridning av infektioner. Underlag som innehåller tryckta elektroder kan även kopplas till en elektrisk läsare. De möjliggör elektrokemisk detektering med förbättrad tillförlitlighet, känslighet och selektivitet jämfört med kolorimetriska tester.

I detta arbete utnyttjades olika rulle-till-rulle kompatibla tryckteknologier vid tillverkningen av kostnadseffektiva pappersbaserade underlag för sensorer. De underlag som var avsedda för kolorimetriska sensorer och mikrofluidik tillverkades genom mönstring av olika pappersubstrat med hydrofobt tryckmaterial baserat på polydimetylsiloxan (PDMS). Beroende på substratets barriäregenskaper så trängde PDMS antingen in i pappret och skapade t.ex. mikrofluidiska kanalstrukturer, eller stannade på ytan och skapade en tvådimensionell analog av en mikroplatta. Prestationsförmågan hos dessa underlag undersöktes genom att trycka glukosoxidasbaserat tryckmaterial på PDMS-fria reaktionsytor. Då glukosanalyt applicerades på en vit reaktionsyta ändrade sig färgen till purpur vars densitet och intensitet berodde på glukoslösningens koncentration. Tryckta elektrokemiska cellplattformer tillverkades på pappersubstrat med lämpliga barriäregenskaper. Elektroderna trycktes med ett material baserat på metallnanopartiklar och gjordes elektriskt ledande med infraröd strålning. Mångsidiga elektrokemiska mätningar utfördes med rena och funktionaliserade elektroder. En elektrokemisk glukossensor valdes till en 'proof-of-concept'-anording för att påvisa potentialen i de tryckta plattformerna.

LIST OF PUBLICATIONS

The following **Papers I–V** are concluded in the thesis and referred to in the text by their corresponding numbers.

I **Paper-based planar reaction arrays for printed diagnostics**

Anni Määttänen*, Daniela Fors, Shaoxia Wang, Dimitar Valtakari, Petri Ihalainen, Jouko Peltonen, *Sensors and Actuators B: Chemical, 160*, **2011**, 1404–1412.

II **Printed paper-based arrays as substrates for biofilm formation**

Anni Määttänen*, Adyary Fallarero, Janni Kujala, Petri Ihalainen, Pia Vuorela, Jouko Peltonen, *AMB Express, 4:32,* **2014,** 1-12.

III **Inkjet-printed gold electrodes on paper – functionalisation and characterisation**

Anni Määttänen*, Petri Ihalainen, Petri Pulkkinen, Shaoxia Wang, Heikki Tenhu, Jouko Peltonen, *ACS Appl. Mater. Interfaces*, *4*, **2012**, 955–964.

IV **Versatile characterization of thiol-functionalized printed metal electrodes on flexible substrates for cheap diagnostic applications**

Petri Ihalainen*, Himadri Majumdar*, **Anni Määttänen**, Shaoxia Wang, Ronald Österbacka, Jouko Peltonen, *Biochim Biophys Acta*, *1830*, **2013**, 4391–4397.

V **A low-cost paper-based inkjet-printed platform for electrochemical analysis**

Anni Määttänen*, Ulriika Vanamo, Petri Ihalainen, Petri Pulkkinen, Heikki Tenhu, Johan Bobacka, Jouko Peltonen, *Sensors and Actuators B: Chemical*, *177*, **2013**, 153–162.

CONTRIBUTION OF THE AUTHOR

The experimental work, analysis of results and writing of the first draft of the articles **I**, **II**, **III** and **V** in this thesis was carried out by the author with the following exceptions:

Paper I: Daniela Fors was responsible for the GOx ink formulation, Dimitar Valtakari for screen printing the GOx ink and Petri Ihalainen carried out the pH-sensitivity measurement.

Paper II: Pigment coated papers (Kaolin and PCC) were fabricated at the Laboratory of Paper Coating and Converting, Åbo Akademi University. The biofilms were grown and the colony forming units counted in Pharmaceutical Sciences, Department of Biosciences, Åbo Akademi University.

Paper III: Petri Pulkkinen was responsible for the synthesis and the TEM and TGA characterization of the gold nanoparticles, Shaoxia Wang for the XPS measurements and Petri Ihalainen for the surface potential measurements.

Paper IV: The author was responsible for the contact angle measurements, printing of the gold electrodes and participated in proof reading.

Paper V: The electrochemical measurements were carried out in collaboration with Ulriika Vanamo.

LIST OF SUPPORTING ARTICLES

S1 **Automating a 96-well microtitre plate model for *Staphylococcus aureus* biofilms: an approach to screening of natural antimicrobial compounds**

Malena Sandberg, Anni Määttänen, Jouko Peltonen, Pia M. Vuorela, Adyary Fallarero, *International Journal of Antimicrobial Agents*, *32*, **2008**, 233–240.

S2 **Living cells of *Staphylococcus aureus* immobilized onto the capillary surface in electrochromatography: a tool for screening of biofilms**

Jie Chen, Adyary Fallarero, Anni Määttänen, Malena Sandberg, Jouko Peltonen, Pia M. Vuorela, Marja-Liisa Riekkola, *Analytical Chemistry*, *80*, **2008**, 5103–5109.

S3 **Impact of surface defects and denaturation of capture surface proteins on nonspecific binding in immunoassays using antibody-coated polystyrene nanoparticle labels**

Tuomas Näreoja, Anni Määttänen, Jouko Peltonen, Pekka E. Hänninen, Harri Härmä, *Journal of Immunological Methods*, *347*, **2009**, 24–30.

S4 **A multilayer coated fiber-based substrate suitable for printed functionality**

Roger Bollström, Anni Määttänen, Daniel Tobjörk, Petri Ihalainen, Nikolai Kaihovirta, Ronald Österbacka, Jouko Peltonen, Martti Toivakka, Organic Electronics, *10*, **2009**, 1020–1023.

S5 **Wetting and print quality study of an inkjet-printed poly(3-hexylthiophene) on pigment coated papers**

Anni Määttänen, Petri Ihalainen, Roger Bollström, Martti Toivakka, Jouko Peltonen, *Colloids and Surfaces A: Physicochemical and Engineering Aspects*, *367*, **2010**, 76–84.

S6 **Enhanced surface wetting of pigment coated paper by UVC irradiation**

Anni Määttänen, Petri Ihalainen, Roger Bollström, Martti Toivakka, Jouko Peltonen, *Ind. Eng. Chem. Res*., *49*, **2010**, 11351–11356.

S7 **Printed sensor and electric field assisted wetting on a natural fibre based substrate**

Jarkko J. Saarinen, Petri Ihalainen, Anni Määttänen, Roger Bollström, Jouko Peltonen, *Nordic Pulp and Paper Research Journal, 26*, **2011**, 133–141.

S8 **Electrodeposition of PEDOT-Cl film on a fully printed Ag/polyaniline electrode**

Petri Ihalainen, Anni Määttänen, Ulriika Mattinen, Milena Stępień, Roger Bollström, Martti Toivakka, Johan Bobacka, Jouko Peltonen, *Thin Solid Films*, *519*, **2011**, 2172–2175.

S9 **Nano-scale mapping of mechanical and chemical surface properties of pigment coated surfaces by torsional harmonic atomic force microscopy**

Petri Ihalainen, Joakim Järnström, Anni Määttänen, Jouko Peltonen, *Colloids and Surfaces A: Physicochemical and Engineering Aspects*, *373*, **2011**, 138–144.

S10 **Inkjet printing of drug substances and use of porous substrates – Towards individualized dosing**

Niklas Sandler, Anni Määttänen, Petri Ihalainen, Leif Kronberg, Axel Meierjohann, Tapani Viitala, Jouko Peltonen, *Journal of Pharmaceutical Sciences*, *100*, **2011**, 3386–3395.

S11 **IR-sintering of ink-jet printed metal-nanoparticles on paper**

Daniel Tobjörk, Harri Aarnio, Petri Pulkkinen, Roger Bollström, Anni Määttänen, Petri Ihalainen, Tapio Mäkelä, Jouko Peltonen, Martti Toivakka, Heikki Tenhu, Ronald Österbacka, *Thin Solid Films*, *31*, **2012**, 2949–2955.

S12 Printed copper acetate based H_2S sensor on paper substrate

Jawad Sarfraz, Anni Määttänen, Petri Ihalainen, Miriam Keppeler, Mika Linden, Jouko Peltonen, *Sensors and Actuators B: Chemical, 173,* **2012***,* 868–873.

S13 Porous silicon micro- and nanoparticles for printed humidity sensors

Tero Jalkanen, Ermei Mäkilä, Anni Määttänen, Jaani Tuura, Martti Kaasalainen, Vesa-Pekka Lehto, Petri Ihalainen, Jouko Peltonen, Jarno Salonen, *Applied Physics Letters 101*, **2012**, 263110.

S14 Influence of Surface Properties of Coated Papers on Printed Electronics

Petri Ihalainen, Anni Määttänen, Joakim Järnström, Daniel Tobjörk, Ronald Österbacka, Jouko Peltonen, *Ind. Eng. Chem. Res.*, *51*, **2012**, 6025–6036.

S15 Top layer coatability on barrier coatings

Roger Bollström, Mikko Tuominen, Anni Määttänen, Jouko Peltonen, Martti Toivakka, *Progress in Organic Coatings, 73*, **2012**, 26–32.

S16 Application of paper-supported printed gold electrodes for impedimetric immunosensor development

Petri Ihalainen, Himadri s. Majumdar, Tapani Viitala, Björn Törngren, Tuomas Näreoja, Anni Määttänen, Jawad Sarfraz, Harri Härmä, Marjo Yliperttula, Ronald Österbacka, Jouko Peltonen, *Biosensors, 3,* **2013**, 1–17.

S17 Low-cost reduced graphene oxide based conductometric nitrogen dioxide sensitive sensor on paper

Jukka Hassinen, Jussi Kauppila, Jarkko Leiro, Anni Määttänen, Petri Ihalainen, Jouko Peltonen, Jukka Lukkari, *Analytical & Bioanalytical Chemistry, 405,* **2013***,* 3611–3617.

S18 **Printed Hydrogen sulfide gas sensor on paper substrate based on polyaniline composite**

Jawad Sarfraz, Petri Ihalainen, Anni Määttänen, Jouko Peltonen, Mika Lindén, *Thin Solid Films, 534,* **2013**, 621–628.

S19 **Biocompatibility of printed paper-based arrays for 2-D cell cultures**

Helka Juvonen, Anni Määttänen, Patric Laurén, Petri Ihalainen, Arto Urtti, Marjo Yliperttula, Jouko Peltonen, *Acta Biomaterialia*, *9*, **2013**, 6704–6710.

S20 ***Staphylococcus aureus*** **biofilm susceptibility to small and potent $\beta^{2,2}$-amino acid derivatives**

Dominik Ausbacher, Adyary Fallarero, Janni Kujala, Anni Määttänen, Jouko Peltonen, Morten B. Strøm and Pia M. Vuorela, *Biofouling, 30,* **2014**, 81–93.

S21 **An impedimetric study of DNA hybridization on paper-supported inkjet-printed gold electrodes**

Petri Ihalainen, Fredrik Pettersson, Markus Pesonen, Tapani Viitala, Anni Määttänen, Ronald Österbacka, Jouko Peltonen, *Nanotechnology*, *3*, **2013**, 1–17.

S22 **A printed H_2S sensor with electro-optical response**

Jawad Sarfraz, Petri Ihalainen, Anni Määttänen, Tina Gulin, Janne Koskela, Carl-Eric Wilen, Ari Kilpelä, Jouko Peltonen, *Sensors and Actuators: B Chemical*, *191*, **2014**, 821–827.

S23 **Enhanced protein adsorption and patterning on nanostructured latex-coated paper**

Helka Juvonen, Anni Määttänen, Petri Ihalainen, Tapani Viitala, Jouko Peltonen, *Colloids and Surfaces B: Biointerfaces, 118,* **2014***,* 261–269.

1. INTRODUCTION AND OUTLINE

Increasing efforts are being devoted to the development of sensors and assays to better diagnose and treat various illnesses at the point of care (POC).[1,2] The diagnosis of infections or diseases can be based on the detection of the infectious agent itself or on the detection of a specific antibody produced by the immune system when being exposed to certain microorganisms or viruses, or on the measurement of a level of a certain analyte in a physiological sample.[3] Symptoms are naturally important signs of diseases, but making the right diagnosis can be difficult e.g. in cases of an infant patient or a rare disease, or simply because of an inaccessible doctor. This results in a compelling need for equipment-free diagnostics and portable hand-held readers that can be integrated with electrochemical POC devices especially in resource-limited locations such as in developing countries or on the field, at home or even in space shuttles.[4]

Paper was among the first materials that were considered for use in low-cost sensors. The use of litmus paper for the determination of acidity of the sample during the early 1800's is probably the most famous example.[5] Paper provides a potential substrate for equipment-free diagnostic applications since its porous structure enables the transport of samples via capillary action and eliminates the need of e.g. pumps.[2] The direction of the liquid flow from the sample zone to the detection zone can be controlled e.g. by introduction of hydrophobic materials or barrier structures on the fiber matrix of the paper. Other requirements set for point-of-care (POC) devices, i.e. affordability, sensitivity, specificity, user-friendliness, rapidness, robustness and deliverability to end-users, can all be met by using paper as a sensor substrate.[6] Printing is increasingly used as means for low cost fabrication of various devices on paper substrates. The physicochemical properties of paper substrates can be readily adjusted by various coating and printing procedures. This allows the use of paper substrates even in applications where good barrier properties against organic solvents and water are needed e.g.

when nanoparticle-based inks are used for the fabrication of electrochemical sensors. Besides capillary action the reactants can be directed to the detection zone by controlling the wetting of a paper surface and thereby creating specific reaction arrays. The reaction arrays can be constructed by printing a predetermined pattern of a hydrophobic material such as vinyl-substituted polydimethylsiloxane (PDMS) -based ink onto a coated paper substrate. The development of such reaction arrays is reported in **Paper I**.

Microbiology is another research area that could benefit from the use of low-cost paper-based platforms. When the platforms are printed on different paper substrates, the influence of e.g. polarity and roughness on the adsorption of biomaterials and the formation of bacterial biofilms can be studied. Such an approach was taken in **Paper II** in which the substrate-dependent formation of bacterial biofilms was studied. It is nowadays established that biofilms formed by *Staphylococcus spp*. account for more than a half of infections associated with prosthetic devices. However, most of the antibiotics used today have been developed to act against dividing phase planktonic bacteria and there is a real need for substrates that prevent biofilm formation and for compounds that can selectively act on staphylococcal biofilms.

Flexibility of the paper substrates enables harnessing of high-speed and high-throughput printing processes for the roll-to-roll mass fabrication of planar reaction areas, electronic components and platforms for POC devices as well as e.g. the high-throughput screening of antimicrobial agents. Modern inkjet printers can be regarded as ideal tools for the fabrication of these devices as the printers can be equipped with several print heads and are thus suitable for both the creation of the patterned substrates and for dispensing multiple chemical reagents or potential antimicrobial agents into the reaction zones all in one print run thus dramatically reducing the production costs and time.[7] **Papers III–V** report on different electrochemical sensor platforms, starting from plain gold electrodes and proceeding to more advanced systems utilizing self-assembly of biomolecules as well as electrochemical polymerization.

2. AIMS OF THE STUDY

The main aim of this thesis was to develop new fabrication procedures for obtaining low-cost paper-based platforms appropriate for e.g. electrochemical analysis, bacterial biofilm formation and screening of potential antimicrobial agents, colorimetric assays, and microfluidic diagnostics. Consequently, the objective was to verify the performance of the platforms by carrying out assays and demonstrations showing that the printed platforms perform as expected and that they have commercial potential.

Efforts were devoted firstly to optimizing the roughness, conductivity and purity of the inkjet-printed electrodes in order to fabricate high-quality application platforms for e.g. self-assembly of biomolecules and electrochemical growth of conducting polymers. A second important goal was to obtain a functional printable ink with a fast curing/drying time that could be used for controlling the wetting properties of the print substrate by creating patterned arrays and channel structures. Such patterned surfaces were used for directing the analyte solution onto predetermined regions.

A related aim was to develop coated paper grades engineered for printing of biomaterials. Such paper substrates would preferably have good adhesion but yet be smooth, isotropic and inert. The substrates should be suitable both for printable electrically functional materials and for biomolecule adsorption with potential applications in biofilm formation and diagnostics.

3. BACKGROUND AND LITERATURE REVIEW

3.1. Paper-based platforms for bioassays and electrochemical analyses

3.1.1. Microplates and their paper-based planar alternatives

Compared to the typical labware such as Test-tubes, Petri dishes and Erlenmayer flasks that were created around 1850, plastic microtiter plates are a relatively new invention, first described about hundred years later.[8] Standardization of the 96-well plates[9] was important for research allowing various analyses with different equipment to be carried out with the same plates. In addition, automation, plate washers, robotic hands etc. have had a huge impact e.g. on high-throughput screening in biomedical research.[10] Despite of all the above mentioned advantages there are also some concerns related to the use of plastic plates. One is the amount of plastic waste produced. Although some bacteria have been found to be able to use polystyrene as a sole carbon source[11] and turn styrofoam (expanded polystyrene) into biodegradable plastic[12], the request for using more environmentally friendly materials or solutions is always in place.

A paper-based planar alternative for the traditional plastic micro plates was described by Carrilho et al. in 2009.[13] The principle of the planar plate is that the liquids are absorbed into the hydrophilic paper-based zone areas where they are confined due to the hydrophobic barriers that surround the zones throughout the total paper thickness preventing cross-contamination. A photolithographic technique involving several steps as illustrated in Fig. 3.1 was used to fabricate the microzone plates. First the whole sheet of paper (Whatman-brand chromatography paper (Chr 1) or Whatman #1 filter paper) is impregnated with the light-sensitive photoresist and dried. Then the sheets are exposed to ultraviolet (UV) light through a mask with transparent areas to cross-

link only the wanted areas i.e. the barrier structures making them insoluble to the developer. Then the sheets are washed and dried. The problem with this procedure is that the whole piece of paper is exposed to the photoresist and since uncontrolled cross-linking may occur it will decrease the flow rate of aqueous fluids and e.g. plasma treatment may be necessary in some particular experiments.

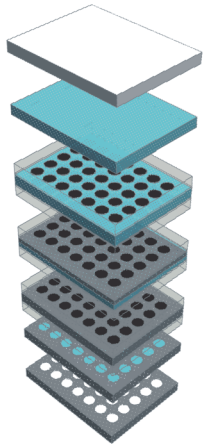

Paper
Apply SC photoresist and
dry under a fume hood (25°C, 1-2 min)
Align a mask and insert glass slides on both sides
Expose to UV light (30 s)
Turn over and expose to UV light (30 s)
Remove the mask and the glas slides
Develope by washing with xylenes and methanol and dry

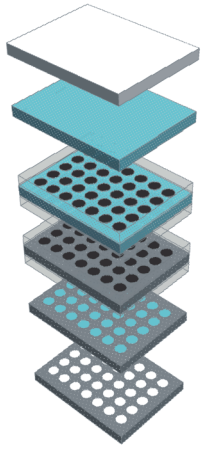

Paper
Apply SU-8 photoresist and
dry with a hot plate (95°C, 5 min)
Align a mask and insert glass slides on both sides
Expose to UV light (15 s, 600 W)
Remove mask and glass slides
Bake (135°C 5 min)
Develope by washing with acetone (5 ml/1 min),
rinse with 70% isopropanol and dry

Fig. 3.1. Procedures for patterning paper using SC (cyclized poly(isoprene) derivative) and SU-8 (a photoresist based on bisphenol A diglycidyl ether resin)[14] photoresist materials.

Paper-based reaction plates bring about several advantages related to e.g. expenses and speed of operations:

i) The plates can be fabricated from inexpensive materials.

ii) Assays can be carried out by using small sample volumes and reagent amounts.

iii) Evaporation of water from the paper wells is about 20 times faster than from the plastic wells due to the high surface-to-volume ratio of paper thus speeding up the assays.

iv) Immobilization of e.g. antigens on macroporous paper grades with high surface-to-volume ratio is fast compared to the 120 min or overnight immobilization steps used in conventional enzyme linked immunosorbent assay (ELISA) protocols.[15]

v) The thin and flexible plates allow printing of reagents on the reaction wells, including possibility for roll-to-roll processing.

vi) Simple shipping, mailing and storage are possible due to the small plate size.

vii) Paper with a high optical contrast is especially suitable for colorimetric detection even by naked eye. Assays can be also conducted with a microplate reader or for example by analysing the readouts with the help of a desktop scanner or camera.

viii) Easy and safe disposal of biohazardous waste by incineration.

ix) Sample preparation for e.g. surface analyses by atomic force microscopy (AFM) is much simpler for flat paper-based substrates compared to plastic 96-well plates which need to be cut into pieces in order to access the bottom of the well.[S1,S3,S19,S20]

Inertness is a prerequisite for a microfluidic substrate to exclude any substrate effects on the analytical results. Similarly the samples and reagents should not influence the substrate. Commercially available

Whatman chromatography paper (Chr 1) is typically used in applications as it yields good results due to its mechanical strength and resistance to tearing even when wet. It also lacks additives that could interfere with the reactions and its capacity to absorb liquids is high (e.g. 11 ± 1 μL cm^{-2} of deionized water).[16,17] Although being a heterogeneous substrate a reasonably uniform structure of the pure cellulose based Chr 1 yields to low variability in the transmittance (index of refraction, n = 1.54–1.62) and is another advantage that makes this paper a suitable choice also in transmittance based colorimetric detection.[18] The costs and times required to prepare a single plate on a Chr 1 with the photolithographic technique was reported to be $0.92 and 16 min with a SU-8 photoresist material and $0.45 and 24 min with a SC photoresist, respectively (Fig. 3.1.). By a large-scale fabrication the production times and costs could be naturally further reduced.[19]

Another material that has been often used as a ”paper” substrate in point of care devices is a nitrocellulose (NC) membrane.[4,20,21]

A totally different method for the fabrication of non-porous and water-resistant platforms for diagnostics was introduced by Orelma et al. in 2012.[22] Nanofibrillated cellulose films based on wood fibers were first oxidized to convert the primary hydroxyl groups to carboxyl groups thereby also lowering the non-specific adsorption. The carboxyl groups were then converted to amine-reactive by EDC / NHS (1-ethyl-3-[3-dimethylaminopropyl]carbodiimide hydrochloride / (N-hydroxysuccinimide) surface activation. Inkjet printing was carried out for the immobilization of antihuman immunoglobulin G (IgG). Advantages of such immunoassay platforms are their sustainable nature, generality and non-toxicity.

3.1.2. Microfluidic paper-based analytical devices

A microfluidic platform, that by definition provides an easily combinable set of fluidic unit operations such as fluid transport and fluid metering, paves a generic and consistent way for miniaturization,

integration, automation, and parallelization of (bio-)chemical processes.[23] Major application areas for the microfluidic platforms are found in *in vitro* diagnostics, drug discovery, biotechnology (e.g. on-line process monitoring in fermentation-based food industry) and ecology (e.g. agricultural and water analysis).[23]

Although initially not used for assay purposes, the first paper-based microfluidic device was developed by Müller et al. in 1949.[24] Chromatographic experiments combined with optical analyses were performed conveniently and rapidly with paraffin wax patterned filter paper. The wax barriers were prepared by pressing a heated metal stamp over a piled filter paper and paraffined paper causing a wax transfer to the wanted areas.

The first report on the utilization of the spontaneous capillary driven flow in a porous support for immunoassay purposes is from 1978 by Glad and Grubb who studied the capillary migration of antigen solutions in porous strips with attached antibodies that specifically influence the migration of the antigen solution.[25] Cellulose and cellulose acetate substrates were also tested but were found to have drawbacks such as nonspecific protein binding and fragility.

Since the introduction of the microfluidic paper-based analytical device (μPAD) by Martinez et al.[26], it has become an attractive platform for e.g. point-of-care diagnostic applications and environmental analyses. Its merits are in its low cost, portability and ability to conduct multiple or parallel assays simultaneously with minimal reagent consumption and without any external liquid pumping or equipment. In addition to the photolithographic technique, several fabrication methods have been described in literature in a search of an easy and inexpensive method for the application of barrier patterns on paper.[5,27] The barriers have been generally constructed by applying hydrophobic materials, albeit a totally different concept for the creation of patterns exists too, e.g. the physical shaping of paper by computer-controlled knife, explored by Fenton et al.[28]

The chemical treatments of paper can be roughly divided into two approaches. In the more complicated techniques, the paper is first made totally hydrophobic and the hydrophilic channels are subsequently created by e.g. washing away certain regions that were covered by a mask during UV treatment[26], plasma treating the wanted areas using a metal mask[29], or inkjet-printing an "etching" solvent dissolving the hydrophobic material[7] or by CO_2 laser treatment[30]. In the more straightforward methods the hydrophobic material is directly applied on the hydrophilic paper e.g. by an inkjet printer[31,32], screen printer[33], x-y-plotter[34], wax printer[35], flexographic printing[36] or by dipping the paper into wax[37].

The fabrication methods of the microfluidic devices are compared in Table 1. In many of the methods relatively time consuming heating or drying steps are required that make the mass-production more challenging.

Table 1. Comparison of the paper patterning methods

Fabrication method	hydrophobic material	hydrophilisation	channel [µm]	patterning	UV/heat treatment	ref
metal stamp press	paraffin	no		wire melter	yes	24
photolitography	SU-8 2010	washing/plasma	186 ± 13	mask for UV	95°C, 5 min x2	26,38
wax printing	wax	no	516 –1000	printing	110–150°C, 0.5-5 min	19,35
knife	no	no	< 1000	knife	no	28
inkjet	alkyl ketene dimer (AKD)	no	300	printing	100°C, 8 min	31,39
flexo	polystyrene	no	500	printing plate		36
laser	hydrophobic paper	CO_2 laser	62 ± 1	computer controlled laser treatment		30
inkjet	polystyrene, 2 h soaked	toluene	550	inkjet printing	15 min drying at RT	7
wax screen-printing	wax	no	650, 1300	screen mesh	100°C, 1 min	33
vacuum plasma	AKD	plasma		mask	100°C, 5-45 min	29
x,y plotter	PDMS in Hexane	no	~ 1 000	printing	70°C, 1 h	34
hot press	parafilm® “M”	no	~ 1 000	polycarbonate film mask	>60°C, 1 min, 200 psi	40
wax dipping	wax	no	639 ± 7	iron mold mask	hot plate 120-130°C, 1s	37
inkjet	actylate composition	no	272 ± 19	printing	UV curing, 1 min	32

The liquid (analyte) transport in the random fiber network of a paper channel occurs via capillary action.[41] Attractive forces between the water molecules and other hydrophilic interfaces, e.g. fibers containing –OH groups, but also the interfacial pressure difference at the meniscus within a pore are the driving forces for the capillary penetration, also called wicking.[42] The speed of the liquid transport can be adjusted in various ways by adjusting various parameters: the length and structure of the hydrophilic channel, the degree of hydrophilicity of the paper substrate, the average pore size and pore size distribution of the substrate and the properties of the transported liquid such as surface tension and viscosity. The Washburn equation (Eq.3.1)[43] has been shown to be a good first order approximation for the penetration distance in a porous media:[31]

$$l = \sqrt{\frac{\gamma r \cos\theta}{2\eta} t} \tag{3.1}$$

where l is the liquid penetration distance in the paper matrix, r is the equivalent capillary pore radius of paper, γ and η are the surface tension and viscosity of the liquid, θ is the contact angle and t is the time of penetration.

In order to be able to conduct complex (bio)chemical assays with minimal end-user input and external instrumentation the control of liquid flow in the channels is important. The liquid flow can be for instance accelerated by sandwiching the paper substrate between polyester films[44] or delayed by printing dissolvable barriers[45] or a number of baffles in the channels[21]. The timing between sequential reactions can be controlled by the use of several inlets[4,45,46] and dissolvable barriers[20] to deliver the reagents to the test zone at different times e.g. to improve the detection limit and amplify the signal.

3.1.3. Electrochemical platforms

As a response to the growing need to perform rapid 'in situ' analyses to improve patient outcomes, a clear trend in analytical chemistry has been the development and miniaturization of electrochemical platforms. Disposable printed electrodes are considered as alternatives for conventional electrodes.[47–49] Like a conventional electrochemical cell, a typical printed three-electrode system consists of a working electrode (WE), a counter electrode (CE) and a reference electrode (RE) as shown in Fig. 3.2.

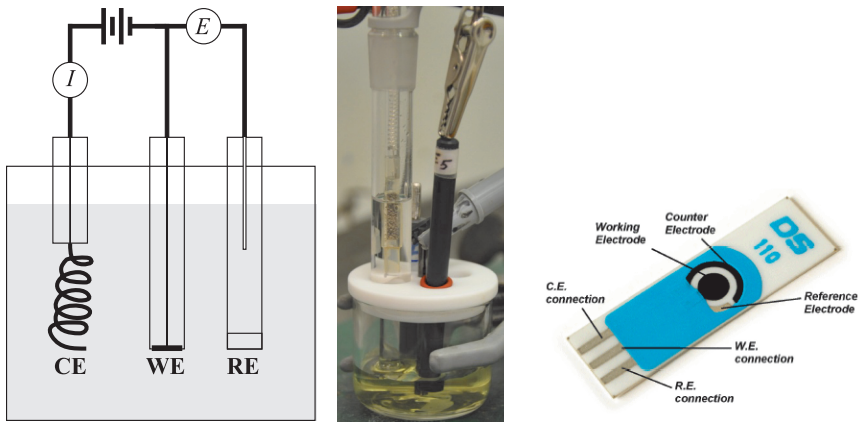

Fig. 3.2. a) A schematic representation of the connections and measurements in an electrochemical cell, b) photograph of a conventional electrochemical cell c) photograph of commercial analogous planar tree-electrode system on a ceramic substrate.[50]

The paper-based electrochemical devices or electrochemical Micro-Paper-based Analytical Devices, EμPADs[51] are usually fabricated by screen printing the electrodes and by patterning the high hydrophilic/hydrophobic contrast patterns or microfluidic channels either by photolithography or wax printing.[51,52,53] The curing steps involved in the fabrication of the paper-based screen-printed electrodes are typically 30–60 min at 60–100°C. In comparison, the temperatures

can rise up to 800°C when commercial electrodes printed on ceramic substrates are cured. Additional heat treatment (60°C, 30 min) is usually applied to cure the protective polymer dielectric material needed to define the electrode area.[52,53,54] Recently, inkjet printing has been demonstrated as an alternative way of producing nanoporous gold electrode arrays on cellulose membranes with the self-catalytic growth of patterns into conducting layers.[55]

Numerous benefits can be related to the use of electrochemical platforms in point of care systems. One of the key benefits is the easy modification of the electrodes, which enables nearly unlimited sensor designs and analyte selection, e.g. for early infection detection.[56] Internal standards have also been incorporated in test stripes to avoid calibration before the actual sample analysis.[57] In addition, electrochemical measurements are relatively unaffected by the sample composition and colour compared to optical systems.[58] For example whole blood, that contains a number of target analytes,[59] can be directly used without any sample clean up prior to measurement. Chen et al. determined uric acid from human whole blood using square wave voltammetry and screen-printed strip consisting of carbon WE and CE and silver pseudo-reference electrodes on a polypropylene substrate.[60]

The unique properties of gold make it the preferred choice as a working electrode material when high performance and safety critical applications are in question. The high conductivity and resistance to corrosion and tarnishing are the main reasons for the good reliability of the gold electrodes. Other benefits are good biocompatibility (compared to e.g. silver[61]) and the versatility of biological moieties that can be attached on gold surfaces simply by using e.g. thiolated linkers, electrodeposition or physical immobilization.[62,63,64,65,66]

Gold nanoparticles have been widely studied for their unique properties to modify the electrochemical behaviour of e.g. screen printed carbon electrodes and for the possibilities they bestow for further functionalisation.[56,67,68,69,70,71] Even commercial gold nanoparticle-modified electrodes are nowadays available.[50]

If necessary, the planarity and versatility of the device architectures enable for instance the use of a paper substrate as a separator[72] or colorimetric detection in combination with the electrochemical detection.[73] Furthermore, coupling of microfluidic systems to a printed electrochemical platform is possible.[70]

3.2. Detection mechanisms in analytical devices

3.2.1. Colorimetric assays

Colorimetric assays are invaluable in many remote health care settings and field analysis locations where it is impossible to maintain or access a fully equipped laboratory. The main benefit of a colorimetric assay is that the visual readouts are typically rapidly generated and can be interpreted by semiskilled nonprofessionals without any information about the symptoms.

Various clinically relevant metabolites have been detected using paper-based sensor platforms (Table 2). Constant efforts are also devoted to design novel tests e.g. for the diagnosis of foodborne pathogens[74] and viral diseases such as dengue fever[20], malaria[4] and viral gastroenteritis[75] that have a potential to infect a large number of people. Table 2 comprises some examples of the quickly growing list of analytes that have been detected in real samples or which have been used as model analytes in artificial samples to validate the performance of the developed μPADs.

Table 2. Analytes detected with μPADs.

Analyte	Reference
glucose	7,19,26,37,38,76
lactate	76
uric acid	1,76
cholesterol	19
heavy metals	77,78
human serum albumin (HSA)	7
bovine serum albumin (BSA)	19,26,37,38
H^+ (pH)	7
phosphatase	29
horse radish peroxidase	35
nitrite	79
human chorionic gonadotropin (hCG)	21
antibody (human anti-HIV-1)	80
rabbit IgG	80
malaria protein Pf HRP2	4

Paper-based colorimetric assays are typically based on enzymatic reactions. The general detection principle for a number of analytes is such that in a 1st step an oxidative enzyme specifically catalyzes the oxidation of the substrate (analyte) and H_2O_2 is generated as a by-product (Eq.3.2-3.5). In the 2nd step the produced hydrogen peroxide reacts with one or more chromophores forming a colorful complex (Eq.3.6).[81]

1st

$$\text{Glucose} + O_2 \xrightarrow{\text{Glucose oxidase}} \text{gluconolactone} + H_2O_2 \quad (3.2)$$

$$\text{Uric acid} + O_2 + 2H_2O \xrightarrow{\text{Uricase}} \text{allantoin} + H_2O_2 + CO_2 \quad (3.3)$$

$$\text{L-Lactate} + O_2 \xrightarrow{\text{Lactate oxidase}} \text{Pyruvate} + H_2O_2 \quad (3.4)$$

$$\text{Cholesterol} \xrightarrow{\text{Cholesterol oxidase}} \text{4-Cholesten-3-one} + H_2O_2 \quad (3.5)$$

$$2^{nd}\quad H_2O_2 + \text{4-aminophenazone} + \text{phenol} \xrightarrow{\text{Peroxidase}} \text{p-(benzoquinone)monoiminephenazone} + H_2O \tag{3.6}$$

To be more precise, the initial step in the first reaction (Eq.3.2) is the conversion of the flavin adenine dinucleotide (FAD) center of the enzyme into its reduced form ($(FAD)H_2$) by glucose. $(FAD)H_2$ then reduces oxygen to form H_2O_2.[82]

It is not always necessary to add and store all the needed chemical reagents and enzymes in the detection zones of the paper devices prior to the addition of the analyte. The properties of pathogenic bacteria to e.g. excrete or produce species-specific enzymes on the growth media or exterior of the cell, respectively, can be utilized for detection purposes. Compared to the conventional culture methods, faster detection of bacteria can be achieved by the use of substrates that change colour in presence of the produced enzymes as demonstrated by Jokerst et al. in 2012.[74]

Enzymes and colour changing substrates are highly useful as they can be utilized also for the detection of antigens. This requires the preparation of enzyme-labeled antibodies. Several methods have been developed for the fabrication of enzyme-antibody conjugates e.g. the glutaraldehyde method (Eq.3.7).[83]

$$\begin{aligned} &\text{Enzyme–}NH_2 + \text{CHO–}CH_2\text{–}CH_2\text{–}CH_2\text{–CHO} \rightarrow \\ &\text{Enzyme–N=CH–}CH_2\text{–}CH_2\text{–}CH_2\text{–CHO} \xrightarrow{+\ \text{Antibody}-NH_2} \\ &\text{Enzyme–N=CH–}CH_2\text{–}CH_2\text{–}CH_2\text{–CH=N–Antibody} \end{aligned} \tag{3.7}$$

The well-known enzyme-linked immunosorbent assay (ELISA) is an example of a technology that utilizes enzyme-labeled antibodies.[84,85,86] Diagrams of popular ELISA formats are shown in Fig. 3.3.

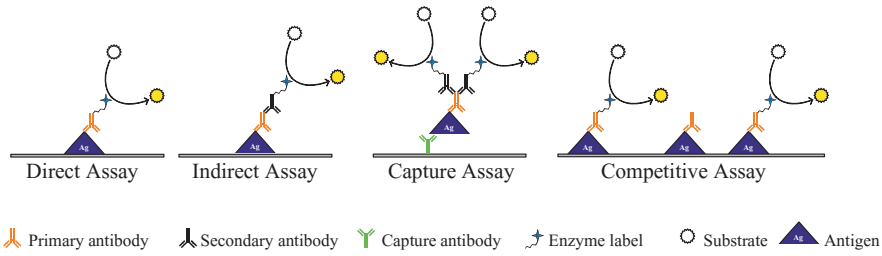

Fig. 3.3. A schematic illustration of popular ELISA formats.

The key step in all the formats is the attachment of the antigen on the assay plate. Two strategies can be used. The antigen can be immobilized on the plate with or without a capture antibody. By using a capture antibody the test antigen does not have to compete with all the other proteins present e.g. in a serum sample when binding to the surface.

When a solution of primary antibodies is added they bind specifically to the antigen. In case of direct assay the primary antibody has been labeled by an enzyme. In the indirect and sandwich formats the secondary antibodies are the ones that have an enzyme-label and they bind with the primary or also so called detecting antibody. Finally an enzymatic substrate is added. The substrates can be chromogenic which change colour in the presence of the enzyme to give a detectable signal. Also fluorescent or chemiluminescent substrates are used. Washing and blocking steps are crucial in the assays to avoid e.g. the binding of primary antibodies on the well surface or the binding of secondary antibodies on the primary antibodies not specifically bound to an antigen which would lead to false-positive signal.

Unlabeled primary antibodies might be present in a serum sample. When such serum sample is added on the well with an antigen coating together with a solution of enzyme-labeled primary antibodies a competitive ELISA is in question as both antibodies compete for antigen binding. The higher the concentration of the unlabeled primary antibodies in the serum the lower is the signal from the labeled primary antibodies.

Advantages of the direct assay are the fewer steps required, making it faster than the other formats. Also cross-reactivity of the secondary antibody is eliminated by the use of only a single antibody. Advantages of the indirect assays over the direct assays are that the sensitivity is increased because each primary antibody contains several epitopes where the labeled secondary antibodies can bind and thus amplify the signal. Other strategy that has been used for signal amplification is the use of avidin-biotin binding.[87] Apilux et al. recently developed an inkjet-printed device that is capable of performing ELISA-based analysis quantitatively in one step.[21] The input edge of the device was simply dipped in the analyte solution and its flow towards the reagents at different locations was controlled by channel structures for timing the correct reaction sequence. The colour change was observed relatively rapidly, within 25 min, compared to paper-based ELISA carried out in separate steps (51 min) or conventional ELISA (213 min).[80] The obtained limit of detection (0.81 ng/mL) for human chorionic gonadotropin (hCG) hormone was also lower than the detectable levels in conventional pregnancy test stripes showing the potential of the inkjet-printed paper-based device for a variety of clinical and environmental assays.

Enzymes can be used also for the monitoring of heavy metal concentrations in drinking waters and other environments. Hossain and Brennen recently demonstrated the use of inkjet-printed colorimetric β-galactosidase (B-GAL) -based paper sensors for the monitoring of carcinogenic heavy metal levels in waters without the need of expensive external instrumentation.[78] The development of this kind of sensors is very important due to the severe healthy risks of the metal contaminated waters for many organs.

In dye-based protein assays, the binding capabilities of proteins can be utilized. Human serum albumin (HSA) for instance is a major transport protein in blood binding reversibly to a large number of compounds, e.g. fatty acids and cortisol. The high affinity of some dyes, e.g. bromocresol green (BCG) and tetrabromophenol blue (TBPB) for albumin enable

their use as indicators in colorimetric assays detecting e.g. protein concentrations in urine.[88,89] Accurate determination of protein concentration is important since abnormally high concentration of albumin in urine is a sign of physiological dysfunction. The reaction between the dye and the protein changes the apparent acid dissociation constant (pK_a) value of the indicator dye resulting in the colour change.[90] To prevent any colour changes from happening due to a change in pH, the protein solutions are buffered to maintain a certain pH.[91] Therefore the intensity of the formed colour (Eq.3.8) is directly proportional to the concentration of the protein and can be visually or instrumentally analysed.

$$\text{Albumin} + \text{BCG} \xrightarrow{\text{pH 4.3}} \text{Albumin-BCG Complex (blue-green)} \qquad (3.8)$$

Rapid determination of the blood type of a patient is important in medical situations where emergency blood transfusion is needed.[39,92] To eliminate the possibility of misinterpretation of colorimetric assays e.g. due to the influence of varying lightning conditions on the results, Li et al. presented a device that reports the results "in writing" instead of a colour change.[39] To get the blood type results in writing, the paper was first patterned with hydrophobic alkenyl ketene dimer leaving letter-shaped areas (A, B, I and X) unprinted. Inside these hydrophilic reaction areas they printed antibodies (anti-A to the letter A, anti-B to letter B, anti-D to letter I and a mixture of anti-A and anti-B to letter X). The blood sample was then applied on top of all the reaction areas and haemagglutination reactions occurred in reaction areas where antigens on the surface of the red blood cells reacted with the corresponding printed antibodies. The agglutinated red blood cell lumps were not easily removed from the fiber matrix in the subsequent washing step unlike the unreacted blood sample thus revealing the test results. Permanent water insoluble ink patterns (O and –) were also printed to enable the determination of all eight possible blood groups (AB+, A+, AB–, A–, B+, O+, B– or O–).

3.2.2. *Electrochemical techniques and assays*

Electroanalytical methods are divided into different categories depending on the experimental variable which is controlled and which is observed. As current and potential cannot be controlled simultaneously, techniques where the potential of the electrode is controlled are called voltammetric methods and techniques where the current is controlled are called galvanostatic methods. Potentiometry on the other hand is a more passive technique where potential is measured under the conditions of no flowing current.

Electrochemical analyses are typically consistent, reproducible, sensitive and selective provided that the measuring parameters and conditions have been properly optimized.[15,52] There is however a limitation related to the electro-activity of the analytes that determines whether they can be detected. The compound under investigation must be able to either i) undergo a facile reduction or oxidation reaction, ii) catalyze some oxidation-reduction process, or iii) be converted into a species that can undergo reduction or oxidation.[93] When a positive potential relative to the reference electrode is applied an oxidation reaction is supported and vice versa[94] as schematically represented in Fig. 3.4.

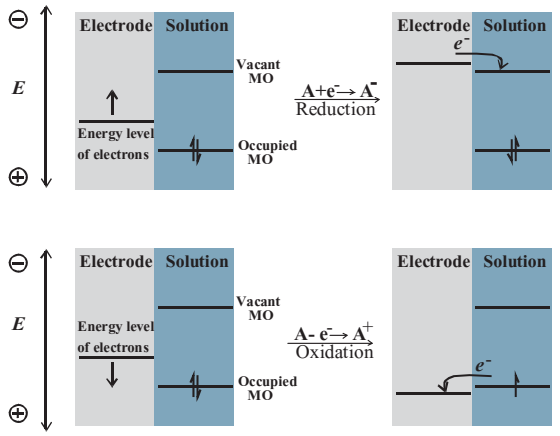

Fig. 3.4. A schematic illustration of a reduction and an oxidation of a species A in solution. The vacant and occupied molecular orbitals (MO) shown are the lowest and highest for species A, respectively.[95]

Although several model analytes[96,97] and some clinically relevant analytes[47,98] can be analysed with bare electrodes, typically promoters, mediators or electrode modification are needed to allow facile oxidation-reduction reactions at electrodes. Many biological macromolecules have a complex three-dimensional structures and a thick insulating protein shell surrounding the electroactive center that restrict their access to the electrode surface. As a result, the electron transfer to the electrode is slow even with large overpotentials. Unfortunately also many smaller molecules, e.g. glucose[99] and hydrogen peroxide[100], are analytes that require large overpotentials for the oxidation or reduction to occur on bare electrodes. Large overpotential is generally avoided since it lowers the sensitivity and specificity as well as increases the risk for interfering molecules.[82,101,102] The reaction products may also adsorb on the electrode surface preventing further reactions.[98,99] Therefore, to gain selectivity and to lower the required potential applied, a number of methods have been developed for the modification of the electrodes. In addition to the use of e.g. ion selective membranes, common strategies involve enzymes mainly for their high inherent specificity. The immobilization strategies can be classified in different ways, but typical categories are: adsorption, cross-linking, covalent binding and entrapment.[47,103,104,105,106] Also e.g. self assembled monolayers (SAMs) have been studied as platforms for enzyme immobilization on electrode surfaces.[107,108]

Since the direct electron transfer between the electrode and an enzyme is slow, as previously mentioned, mediated electron transfer is typically used. Mediators are usually nonphysiological redox couples, e.g. Fe^{2+}/Fe^{3+}, which reduce the potential of electron transfer. Taking glucose as an example analyte, the utilization of a mediator for a bienzymatic biosensor is shown in Schema 1.[109] The mediators can be simply dissolved in solution. When being immobilized on the electrode surfaces mediators bring about both economical and ecological advantages. In addition, long stabilization times that may occur for dissolved redox mediators are avoided.[110]

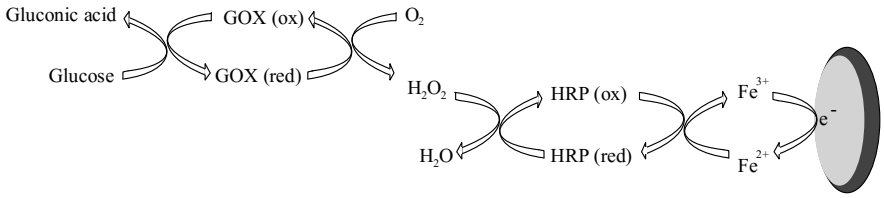

Schema 1. Mediated bienzymatic glucose detection at an electrode.

Voltammetric techniques are routinely used to gather information about analyte concentration or electrochemical reactions in analytical chemistry as well as for investigating novel modified electrodes. To carry out the experiments, a potentiostat is connected to the voltammetric cell and used to control the potential on the working electrode (WE) with respect to the potential of the reference electrode (RE) simultaneously while the current flowing between the counter electrode (CE) and WE is measured (Fig. 3.2.a).[111]

To ensure a stable potential at the RE, a CE is used to minimize the current that flows through the RE, because it might cause a potential drift. The area of the CE is usually larger than that of the WE to ensure good electron flow. The three electrodes are immersed in an unstirred solution containing the analyte(s) under investigation and a supporting electrolyte (electrochemically inert salt e.g. KNO_3 or KCl dissolved in water) for increased conductivity and to diminish the effect of the electric field on the motion of the analyte.[112]

Some typical voltage versus time curves that are used in the electrochemical measurements are shown in Fig. 3.5. Amperometric (Fig. 3.5.a) and chronoamperometric measurements (Fig. 3.5.b and 2.5.c) are relatively simple and can be used in commercial hand-held electrochemical readers which are integratable with printed EμPADs[51] thus narrowing the gap between laboratory and field analysis.

The chronoamperometric detection principle is shown below with D-lactate as an example target analyte.[113]

$$\text{D-lactate} + NAD^+ \rightleftarrows \text{pyruvate} + NADH + H^+ \quad (3.9)$$

$$Med_{ox} + NADH \longrightarrow NAD^+ + H^+Med_{red} + 2e^- \quad (3.10)$$

$$Med_{red} \xrightarrow{(E>E^{o'})} Med_{ox} + 2e^- + H^+ \quad (3.11)$$

In the first step the oxidized nicotinamide adenine dinucleotide (NAD^+) cofactor part of the active site of D-lactate dehydrogenase enzyme is reduced and D-lactate is transformed in puryvate (Eq.3.9). Usually two-enzyme systems are utilized to shift the equilibrium of this enzymatic reaction to the product side, but Avramescu et al. incorporated Mendola's blue mediator for this purpose as well as for reducing the overpotential of the oxidation of NADH (Eq.3.10).[113] The final step is the electrochemical reoxidation of the mediator at a proper potential ($E > E^{o'}$) at the working electrode (Eq.3.11) i.e. crossing of an electron(s) through the electrode/solution interface which is a measurable quantity.

Cyclic voltammetry (Fig. 3.5.g) is however possibly the most widely used of the voltammetric measurements. A characteristic shape of a diffusion limited cyclic voltammogram is shown in Fig. 3.6. Although the I vs E curve is rather inconveniently asymmetric, a lot of general information about the electrochemical behaviour of the analyte can be drawn from its shape by e.g. calculating parameters such as peak current (I_p), peak separation (ΔE_p) and formal reduction potential of the reversible redox couple ($E^{o'} = (E_{pa}+E_{pc})/2$) (**Paper V**). The step techniques are usually preferred when quantitative information is of primary importance as the detection limits e.g. for square wave voltammetry (Fig. 3.5.f) may be on the order of nanomolar concentrations due to the lesser contribution of capacitive charging current.[114]

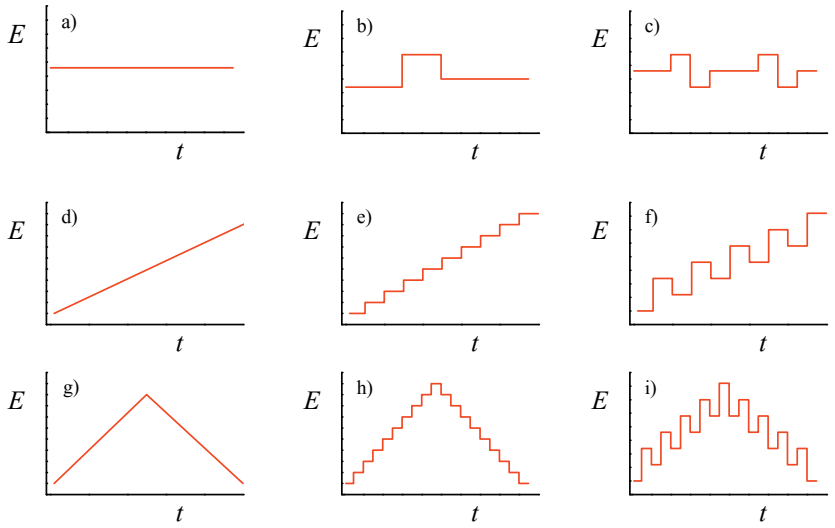

Fig. 3.5. a) amperometry, b) double potential step chronoamperometry, c) triple potential step chonoamperometry, d) linear sweep voltammetry, e) staircase voltammetry, f) square wave voltammetry, g) cyclic voltammetry and h) cyclic staircase voltammetry and i) cyclic square wave voltammetry.[115,116]

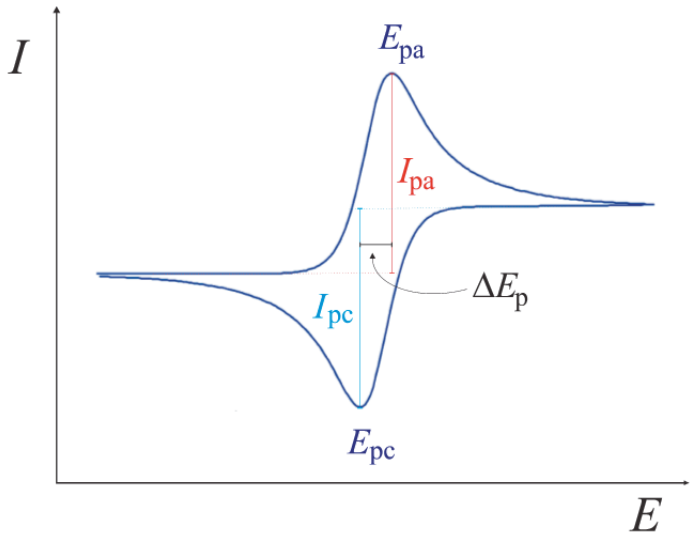

Fig. 3.6. A typical shape of a diffusion limited cyclic voltammogram and the definitions of the parameters that are used to describe the electrochemical reactions at the electrodes.

The scanned potential range is selected so that the formal potential of the analyte is within the potential range. During the forward scan the current first increases till the potential reaches the oxidation potential of the analyte and then decreases when the flux of the reactant to the WE is too slow due to the grown diffusion layer. During the reverse scan, the inverse process occurs if an electrochemically reversible redox couple is in question. The peak current, I_p, is described by the Randles-Sevcik equation (Eq.3.12) (**Paper V**):

$$I_p = (2.69 \times 10^5) n^{3/2} A D^{1/2} c v^{1/2} \quad (3.12)$$

where n is the number of electrons participating in the redox process, A is the electrode area [cm^2], D is the diffusion coefficient [cm^2/s], c is the concentration [mol/cm^3] of analyte and v is the scan rate [V/s]. The theoretical difference between the oxidation and reduction peaks (ΔE_p) is 59 mV for a reversible reaction with one-electron transfer (n = 1) occurring at 25°C.[117] Theoretically the ratio of the peak currents should be equal to unity for a totally reversible redox couple (Eq.3.13) (**Paper V**):

$$\left| \frac{I_{pa}}{I_{pc}} \right| = 1 \quad (3.13)$$

Many of the protocols and detection principles discussed earlier in the colorimetric assays section (*3.2.1.*) can be adapted to electrochemical measurements carried out with printed electrodes simply by using suitable electrochemical substrates. Amperometry, chronoamperometry and cyclic voltammetry for example have been used as detection mechanisms in combination with ELISA.[15,66,118] Salam et al.[66] demonstrated the chronoamperometric detection of *Salmonella typhimurium* by using an electrochemical immunosensor with 3,3',5,5'-tetramethylbenzidine dihydrochloride (TMB)/H_2O_2 as the enzyme mediator/substrate system (Fig. 3.7). First TMB (Red) is enzymatically oxidized to TMB (Ox) (Eq.3.14) and subsequently it reduces back to

TMB (Red) at the printed gold electrode (Eq.3.15).[119] The proposed system is a promising, rapid and sensitive method for on-site detection of pathogenic contaminants.

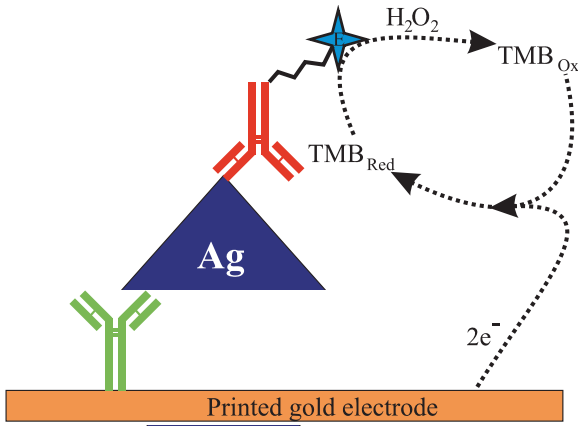

Fig. 3.7. The detection principle of an electrochemical immunosensor for salmonella (Ag = salmonella cell).

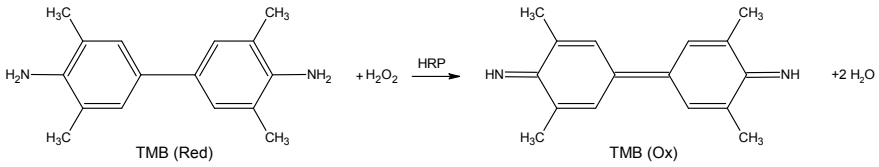

(3.14)

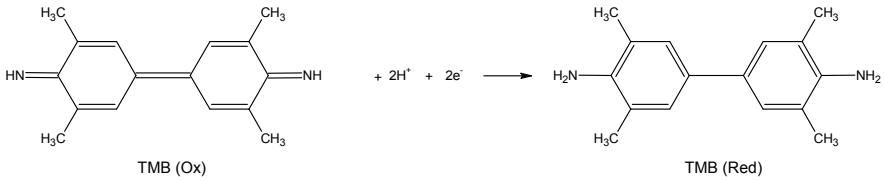

(3.15)

Li et al. presented a low-cost paper-based electrochemical ELISA that was suitable for sensitive medical diagnosis or pathogen detection in developing countries[15] (Fig. 3.8.).

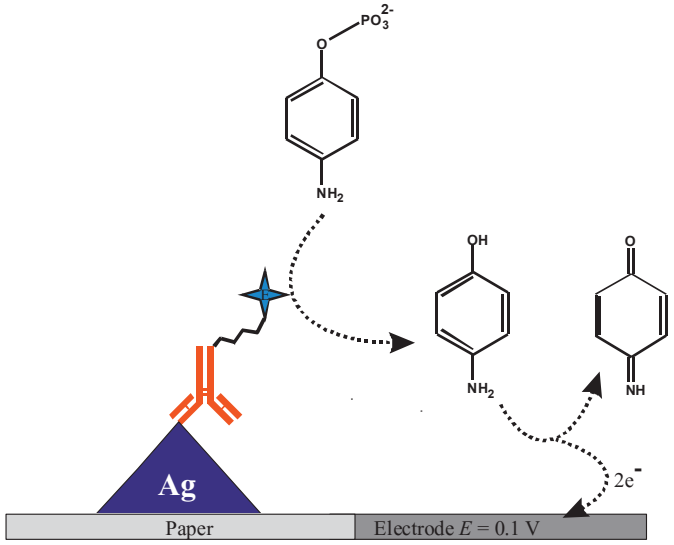

Fig. 3.8. The detection principle of an electrochemical ELISA (model antigen, Ag = IgG).

A clever and nearly universal electrochemical platform was proposed by White et al.[120] for the quantitative multiplexed detection of specific antibodies. Current standard methods used for the detection of antibodies such as ELISA and Western blots are relatively slow. Therefore electrochemical assays are relevant for not only diagnosis but also for prevention and treatment of many illnesses both in the developed and developing countries. In the approach by White et al. gold working electrodes were modified with thiolated deoxyribonucleic acid (DNA) anchor strands that have a methylene blue redox reporter at the 3' terminus. The complementary strand with an antibody binding epitope at the 5' terminus was then introduced to form the duplex strand. In the absence of the antibody, the methylene blue is able to approach the electrode surface and participate in the electron transfer but as soon as the specific antibody binds to the epitope a reduction in the electron transfer is observed. By square wave voltammetry measurements the platform was shown to detect antibodies at concentrations as low as 500 pM. The proposed electrochemical DNA antibody sensor platform performed well with undiluted blood samples, small sample volumes

and gave results within minutes and required no washing steps. It thus appears to be a platform with great potential for point of care devices.

Another area in clinical analysis that could benefit from a simple electrochemical platform is the simultaneous determination of multiple tumor markers, because single tumor marker detection has been criticized for high rate of false positives and negatives.[121,122] In order to simultaneously detect multiple targets in a sample Fen-Ying Kong et al. developed a novel strategy that was based on a single sensing electrode having differently functionalized branches. The system was also label-free, reagentless and utilized single channel operation, all of these being factors that are beneficial considering point of care devices.

Potentiometry is gaining increasing interest for its applicability as a detection method in low cost electrochemical sensors.[123] An equation that relates the potential of an electrochemical cell in nonstandard conditions to the activity of the cell components, i.e. the Nernst equation, is highly useful for electrochemistry. It can be developed by inserting the following expressions (Eq.3.16-3.17)

$$\Delta G = -nFE \tag{3.16}$$

$$\Delta G^{o} = -nFE^{o} \tag{3.17}$$

into the thermodynamic relationship for Gibbs free energy (3.18) and by dividing both sides with $-nF$.[111]

$$\Delta G = \Delta G^{o} + RT\ln Q \tag{3.18}$$

$$E = E^{o} - (RT/nF)\ln Q \tag{3.19}$$

In the Nernst equation (Eq.3.19), E = non-standard cell potential (the maximum potential between two electrodes), E^{0} = standard state cell potential ($E^{0} = E_{\text{cathode}}{}^{0} - E_{\text{anode}}{}^{0}$), R = universal gas constant, T = absolute temperature, n = number of electrons exchanged in the reaction, F = Faraday's constant and Q = reaction quotient.

Keeping in mind that ln(x) = log(x)/log(e) = 2.3log(x), the following simplified form (Eq.3.20) can be written that is valid at 25°C.

$$E = E^{o} - 0.059/n * \log Q \tag{3.20}$$

For a general half reaction (a ox + n e^- → b red) the reaction quotient is defined as (Eq.3.21) or (Eq.3.22) as it is convenient (although not possible in every conditions) to replace the activities (**a**) with concentrations.

$$Q = (\mathbf{a}_{red})^b/(\mathbf{a}_{ox})^a \tag{3.21}$$

or

$$Q = [red]^b/[ox]^a \tag{3.22}$$

A typical form of the Nernst equation is therefore obtained, which can be used for e.g. estimating the concentration ratio of the reduced and oxidized species at the electrode surface during CV measurements (Eq.3.23) (**Paper V**).[117]

$$E = E^{o} - 0.059/n * \log([red]^b/[ox]^a) \tag{3.23}$$

A pH meter is a well known instrument that utilizes a potentiometric measurement. A pH meter measures the potential difference between the measuring electrode and the reference electrode which are separated by a special glass membrane. The Nernst equation can be applied (Eq.3.24)

$$E = \text{constant} + 2.3RT/F * \log \mathbf{a}H^+_{(solution)} \tag{3.24}$$

Using the definition for pH (Eq.3.25) and a temperature of 25°C an equation which reveals the theoretical slope (59 mV/pH) of *E* vs pH plot for an electrode with a Nernstian behaviour is obtained (Eq.3.26) (**Paper V**).[124]

$$pH = -\log(\mathbf{a}H^+) = -\log[H^+] \tag{3.25}$$

$$E = \text{constant} - 0.059\ \text{pH} \tag{3.26}$$

Electrochemical impedance spectroscopy (EIS) measures the ability of a circuit to impede the flow of a current (I).[125] Thus impedance (Z) and the total resistance (R_{eq}) are identical (Eq.3.27) when a voltage source e.g. a battery that creates a potential difference (E) and produces direct current (dc) is connected in a simple circuit that contains a resistor or resistors (R_1, R_2, R_3) connected in series (Eq.3.28) or parallel (Eq.3.29) (Fig. 3.9).

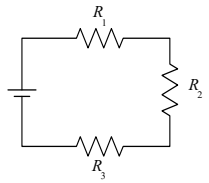

$$Z = R_{eq} = \frac{E}{I} \tag{3.27}$$

$$R_{eq} = R_1 + R_2 + R_3 \tag{3.28}$$

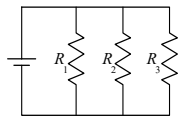

$$\frac{1}{R_{eq}} = \frac{1}{R_1} + \frac{1}{R_2} + \frac{1}{R_3} \tag{3.29}$$

Fig. 3.9. Resistors connected in series and parallel.

Compared to resistance, impedance is a more general circuit parameter and can be calculated for circuits that include also other components than resistors, for example inductors and capacitors, while alternating current (ac) is applied. Impedance is defined as (Eq.3.30)

$$Z = \frac{E_t}{I_t} = \frac{E_0 \sin(\omega t)}{I_0 \sin(\omega t + \phi)} = \frac{E_0 \sin(2\pi f t)}{I_0 \sin(2\pi f + \phi)}, \tag{3.30}$$

where E_t (potential at time t) is the excitation signal, E_0 is the amplitude of the signal and f is frequency [Hz] and I_t is the response signal, ω is radial frequency, I_0 is the amplitude and ϕ is the phase shift (Fig. 3.10).

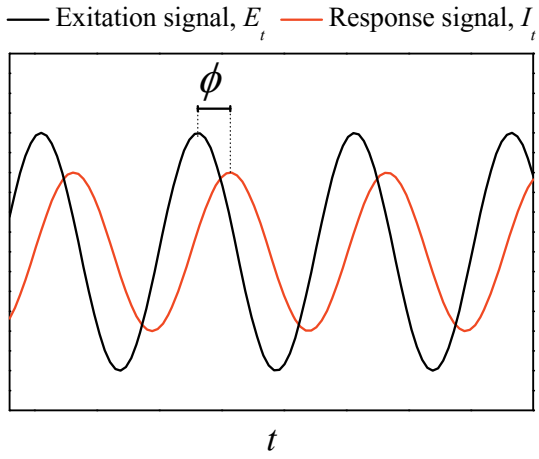

Fig. 3.10. The applied sinusoidal ac exitation potential E_t and sinusoidal current response signal I_t of the electrochemical cell.

Impedance is also defined as the sum of the real impedance (resistance) and the imaginary part (reactance) (**Papers IV and V**) (Eq.3.31)

$$Z = Z' + iZ'' \tag{3.31}$$

Thus the Z' and Z'' values cannot be summed directly. One way to present impedance data is to plot $-Z''$ values on the imaginary y-axis and Z' values on the real x-axis to give a complex-plane impedance plot, often termed a Nyquist plot.[125] The vector Z can be calculated with the help of Pythagoras sentence if Z' and Z'' are known. Or if the phase angle is known, the basic trigonometric functions (3.32-3.33) may be also utilized (Fig. 3.11.b).

$$Z' = Z\cos\phi \tag{3.32}$$

$$Z'' = Z\sin\phi \tag{3.33}$$

EIS measurements are typically used to get information about an interface, for example to evaluate the performance of a coating (**Paper IV**) or to study corrosion systems.[125,126,127,128] For a purely capacitive and perfect coating, the circuit model is shown in Fig. 3.11.a. The Nyquist

plot for such a system would be a strait vertical line. The solution resistance can be estimated from the intercept of the curve with the x-axis. For real coatings modeling is a powerful tool which can be used for finding an equivalent circuit that would give corresponding EIS results. The Randles equivalent circuit is often used as the starting point for modeling. The circuit is composed of the electrolyte resistance (R_s), the charge transfer resistance (R_{ct}) and the double layer capacitance (C_{dl}). The corresponding Nyquist plot is shown in Fig. 3.11.b. The disadvantage of Nyquist plot is that one can not tell the frequency range used in the measurements. On the other hand, for example the R_s and R_{ct} values are easily determined from the intercepts of the semicircle with the x-axis (Eq.3.34-3.35):

$$R_s = \lim_{f \to \infty} |Z| \tag{3.34}$$

$$R_s + R_{ct} = \lim_{f \to 0} |Z| \tag{3.35}$$

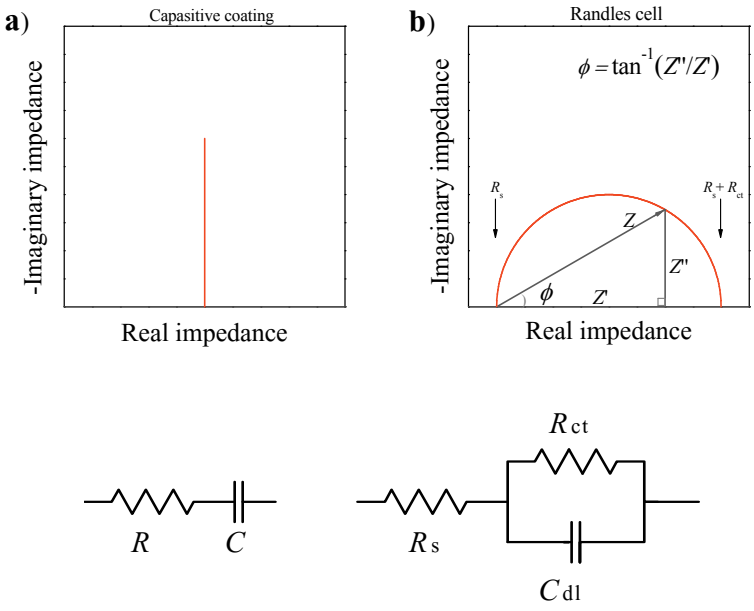

Fig. 3.11. Nyquist plots and circuit models for a) a perfect capacitive coating and b) Randles cell.[131]

Benefits of EIS are that it is a label-free and nondestructive detection method e.g. for determining DNA hybridization, the influence of binding of electrochemically inert antibodies and antigens on the impedance of the system.[127,129,S16,S21] The Randles model for example was shown to be applicable for modeling the impedance data of dust mite antigen biosensors.[130] Especially the ΔR_{ct} parameter correlated well with the analyte concentrations showing the potential of EIS as a detection method for low-cost and high sensitivity sensors.

Also capacitance measurements have been used for the direct detection of antibody-antigen interaction.[132] Bataillard et al. carried out capacitance measurements in simple buffers using a custom made electrochemical three-electrode cell and found that as binding events on the functionalized electrode occur, the thickness of the dielectric layer increases which results in a decrease in the capacitance.

3.2.3. Microplate readers

Carrilho et al.[13] established the use of a standard microplate reader showcasing the usefulness of the paper-based devices as worthy alternatives for plastic plates. A microplate reader is essentially a cuvette-based spectrophotometer transferred to typically a 96-well format.[133] Sophisticated readers are able to measure e.g. absorbance, fluorescence and time-resolved fluorescence.

When absorbance measurements are carried out with opaque filter papers, the transmittance of the light needs to be enhanced e.g. by using a mineral oil or other liquid with a refraction index matching the refraction index of cellulose. A paper substrate becomes more translucent as the air gaps between the fibers become filled with the index-matching fluid and scattering thus reduced.

In order to be able to use the conventional plate readers successfully for fluorescence measurements, the autofluorescence properties of the paper substrate need to be adequately low for obtaining a good signal to

background level thus enabling also the detection of low analyte concentrations. With the choice of a proper label, e.g. europium (III) or terbium (III) that forms a fluorescent chelate with a long fluorescence decay time[134] problems related to substrates could be circumvented by using a time-resolved detection mode.

Microplate readers as well as sensors that utilize chemiluminescence (CL)[135,136] or electrochemiluminescence (ECL)[137,138] as the detection method may well gain importance in future as they provide added selectivity, sensitivity and a wide dynamic concentration response range.

3.3. Adsorption of biomaterials

3.3.1. Proteins

Adsorption is an extensively studied phenomenon that occurs when a solid surface is exposed to an aqueous solution containing e.g. proteins.[139] However, there is a lack of consensus related to this complex process.[140,141] Some research groups consider the adsorption as an irreversible attachment of proteins on the surface and thus often perform rinsing steps to remove the weakly bound proteins to form a thin (2D) protein layer.[140] Other groups on the other hand count also the weakly bound proteins near the surface as part of the (3D) interphase that separates the bulk solution and the solid substrate.[140] The adsorption of proteins and their fate have fundamental importance to a broad field of science.[142,143,144]

The conventional explanation for the low protein adsorption on hydrophilic surfaces is that in order to adsorb, the proteins must replace the water molecules that are adsorbed at the surface. Depending on the hydrophilicity of the solid substrate this dehydration step requires different amount of energy.[140] When the water contact angle is ~ 65° or lower the dehydration becomes energetically so unfavorable that

accumulation of proteins on the surface from the bulk phase is not occurring.[141] Proteins have been shown to adsorb also on the very smooth muscovite mica surface, which is a highly hydrophilic substrate. The adsorption is however extraordinary involving an ion-exchange mechanism.

A compensating factor that has been said to be a driving force for adsorption is then again the entropy gain that is achieved when the adsorbed water molecules are released from the surface and from the hydrophobic parts of the protein that come into contact with the surface. Also structural changes that occur in the protein may increase its conformational entropy and thus enhance adsorption affinity.[145,146]

Critical aspects considering many of the applications are the degree of protein coverage, the orientation in which the protein is adsorbing on the substrate and whether or not the proteins retain their functionality after adsorption.[147,148] The amount of adsorbed proteins, adsorption strength and the degree of their conformational change upon adsorption has been shown to depend on various factors. External factors include e.g. temperature, pH, ionic strength and buffer composition and concentration of the protein solution. At high protein concentration and temperature the surface will be saturated typically more rapidly leading to higher amount of adsorbed proteins. The rapid and pronounced adsorption does not leave time nor space for the proteins to spread on the surface. Another factor that influences the speed of adsorption is the pH of the solution, which influences the charges at the surfaces. When the charges are opposite the adsorption is also faster. However at a pH which equals the isoelectric point of the protein, highest packing density is usually obtained because the electrostatic repulsion between the proteins is at a minimum.[149] The ionic strength of the protein solution has an influence that is dependent on the proteins. When the surface and the protein are oppositely charged, increasing ionic strength hampers adsorption. When the charges of the proteins and the surface have the same sign the dissolved ionic species in the solution shorten the range of

the electrostatic interactions between the protein and the surface, thus enhancing adsorption.

The properties of protein that have an influence on the adsorption include structural stability, size, composition and surface charge. Proteins that have the capability to change their structure upon adsorption are so called soft proteins.[150] The higher the surface-protein contact area becomes the higher is the gain in free energy and also the strength of adsorption. Therefore larger proteins typically adhere stronger on the substrate than small proteins. Large conformational changes or denaturation however might affect the functionality of some proteins.[150,151]

There are naturally various surface properties like for instance surface polarity, surface charge, surface free energy, surface topography, the hydrophobicity and hydrophilicity and the presence of specific chemical groups on the surface, that have an influence on protein adsorption [139,152, 153,154,155,156] Non-polar, high surface tension and charged surfaces tend to be adsorbing proteins more strongly than polar, low surface tension and uncharged surfaces, respectively.[139,157] The nanoscale morphology has been shown to increase the saturation uptake and the amount of adsorbed proteins not merely due to the increased surface area but also via the geometrical arrangement of proteins on the surface.[158,159]

Significant efforts have been devoted in order to decrease protein adsorption on e.g. medical implant surfaces and catheters since the conformational changes occurring in the proteins may trigger inflammation, coagulation and foreign body response.[143] Poly(ethylene glycol) (PEG) modified surfaces are considered as highly protein-repellent materials due to the steric repulsion and excluded –volume effects between the protein and the PEG modified surface. PEG and oligo(ethylene glycol) functionalized surfaces contain OH groups that are capable to form hydrogen bonds. Interestingly also the elimination of functional groups that include hydrogen bond donor moieties has been observed to be an effective way to prevent protein adsorption.[157]

3.3.2. Bacteria

Bacteria prefer to adhere on available surfaces and form microbial communities rather than exist as nomadic free floating cells.[160] This is perhaps because of the usually better abundance of nutrients near solid surfaces[161], the solid surface may also itself be a nutrient source.[162] The surface attached bacteria are embedded in a self-produced biofilm matrix consisting of extracellular polymeric substance (EPS) which provides a protection against adverse environmental conditions thus offering good survival possibilities. Consequently bacterial adsorption, colonization, development to mature biofilms and finally the dispersion and dissemination of bacteria cause significant risks to biofilm-associated infections that may lead to morbidity and even death.[163,164] Although it is possible to temporarily clean the surface of e.g. a prosthetic device before an operation, the ability of bacteria to inhabit tissue and medical implants e.g. through hematogenous spreading from infections elsewhere in the body[165] causes a serious healthcare issue[166, 167,168] especially due to the high antibiotic resistance of biofilms. Therefore it is important to gain detailed knowledge about the factors that have an influence on the bacterial adhesion, biofilm formation and their various survival strategies[160,169,170], and furthermore development of either acute or chronic infections[171]. Such knowledge enables the design of more effective antimicrobials that kill or inhibit the spreading of micro-organisms.[172] Equally important is the development of durable engineered antimicrobial surfaces for orthopedics, dentistry and other applications requiring high hygiene in challenging conditions.[173,174] On the other hand, search for effective materials for retention of micro-organisms e.g. in soil or removal of them is important to prevent waste waters from contaminating ground water supplies.[175]

The factors that influence the bacterial adhesion or irreversible interaction between the bacteria and the substrate can be categorized into three groups: physical, chemical and microbiological.[176] One important physical factor related to the substrate is its surface roughness that increases the effective (real) surface area and thus provides more

adhesion sites especially when the surface irregularities are of the size comparable to the bacterium thus increasing the bacterium-substrate contact area. Also the shear forces (generally higher shear rates are considered to result in decreasing the number of attached bacteria) are lower at certain shadowed areas which may reduce the desorption rate at those spots and thus increase adhesion.[177] Organic matter, e.g. proteins, usually adsorbs rapidly on clean surfaces and forms a so called conditioning film that has been shown to play a role in the adhesion of bacteria.[178] The irreversible adherence of bacteria is also linked to the production of EPS and biofilm formation[179], which is enhanced e.g. if glucose is readily available[180]. The biofilm surface may also provide a suitable surface for further adsorption of bacteria.[181] Rode et al.[180] carried out a broad study of the effect of e.g. temperature on the biofilm formation with several strains of *S. aureus. S. aureus* is a common pathogen in humans and animals. The study showed that it is critical to investigate several strains before drawing general conclusions regarding biofilm formation since the strain to strain variation was considerable.

pH of the solution is a chemical factor which influences the surface charges of both the substrate and the bacteria and has an influence on the adsorption. Adsorption is favored when the surface and the bacteria have opposite charges.[182] If the surface and the bacteria are both negatively charged the presence of charged ions that are usually found in liquids neutralize both the solid surface and the bacteria by accumulating on the surface and forming a double layer the thickness of which depends on the ionic strength of the solution. As a result the attractive van der Waals forces may become higher than the repulsive electrostatic forces and bacteria may attach on the solid surface.

A typical microbiological factor that influences bacterial adhesion is the hydrophobicity of the organism, which may change depending on the growth conditions.[183,184] It has been shown that hydrophobic organisms prefer to adhere on hydrophobic materials. On the other hand hydrophilic surfaces are more attractive for some bacteria. Therefore superhydrophobic substrates have been shown to be good candidates in

a search for surfaces where bacterial contamination would be minimal.[185] Other strategies involved in the adhesion of bacteria are the production of surface appendages (e.g. flagella) that allow them to overcome the electrostatic repulsive forces when approaching a surface[186] and chemotaxis that controls flagellar motion and allows them to find an environment that provides the necessary energy supply[187].

3.3.3. Thiols

Thiolation of metal surfaces (Au, Pt, Pd, Ag, Cu and Hg) is a spontaneous process due to the fact that the free energy of the interface between the metal and the ambient environment decreases as a consequence of the formation of a self-assembled monolayer (SAM) of thiols from solution.[64,188] There are several reasons for gold being the most often used metal surface in the investigations of SAMs of alkanethiols; for example the strong and energetically favorable interaction between gold and thiol groups and the availability of gold surfaces (thin films, patterned structures, colloids etc.). Gold is an inert metal and non-toxic to cells, and the SAMs on gold are stable for periods of days to weeks also in complex liquid media.[189]

The adsorption and reorientation behaviour of various thiols has been intensively studied to gain insight of the attachment modes.[190–194] Cohen-Atiya and Mandler[195] proposed a detailed mechanism for the formation of a covalent bond between the metal surface and sulphur (Fig. 3.12).

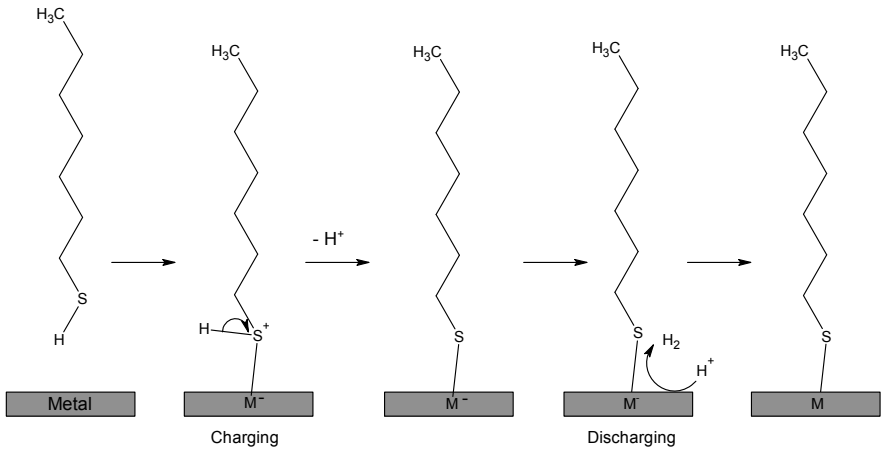

Fig. 3.12. Adsorption of thiols on metal surfaces.[195]

The potentiometric measurements suggested that initially a negative charge is transferred from the thiol group to the gold surface as the H-S bond breaks. After that a discharging process occurs where protons from the solution reduce at the electrode and eliminate the accumulated negative charge on the surface.

Possible application areas for SAMs are numerous since the chain length and the terminal group of the adsorbed molecules can be varied according to requirements. SAMs have been used to carry out fundamental wetting studies.[188] More recently SAMs have been incorporated for immobilization of biological molecules or as recognition elements in biosensors.[108,196] They are also useful as model surfaces for studying the adsorption of cells and proteins.[197,198]

The high binding affinity of thiols on silver nanoparticles has been utilized in a laber-free colorimetric detection of biological thiols e.g. cysteine (amino acid).[199] Thiolation is also utilized in the stabilization of gold nanoparticle suspensions to enable their use as inks for the fabrication of printed conducting tracks[200] and in nanomedicine[201,202,203].

3.4. Printing and coating techniques

3.4.1. Inkjet printing

The tendency of a liquid stream to break up into individual droplets (Fig. 3.13.) was experimentally studied by Plateau[204] in 1873 and later analytically explained by Rayleigh[205] in 1878. The droplet formation is a consequence of perturbations that cause instability to the liquid column when the length of the column exceeds its diameter by a factor of about 3.13. In addition, the surface tension drives the liquid to surface area minimization, achieved by the formation of spherical droplets.[204,205] This phenomenon was exploited in the first patented inkjet-printer.[206]

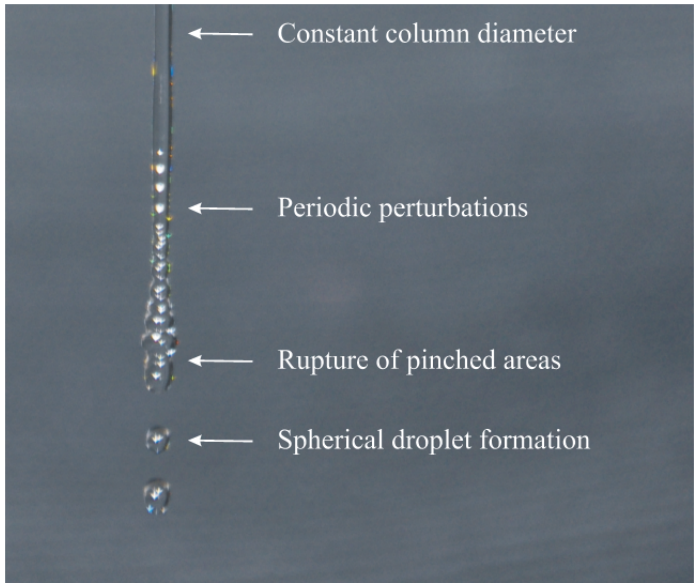

Fig. 3.13. A photograph showing the droplet formation that occurs while water drains from a spigot.

A more controllable way for forming droplets with uniform size and spacing was introduced by Sweet in 1960s.[207] The method was based on an applied pressure wave that broke the liquid stream into droplets. Since then, the development of inkjet printing technology has been

immense. The advantages of inkjet-printing technology have made it a commonly used method for modern industrial applications. Especially the digital pattern generation and its fast modification together with the noncontact nature and high resolution[208] are significant benefits that allow the method to be used in a wide range of applications such as discovery of new drugs[209], printing of medical and pharmaceutical ingredients[210,S10], printing of electronic components and devices[211,212] and fabrication of 3D objects[213,214] for e.g. rapid prototyping or even for new body parts in the future.

Various technologies have been developed for the droplet generation that are based either on a continuous formation of charged drops and their deflection in order to create the print pattern (continuous inkjet printing, CIJ) or on a drop-on-demand (DOD) mode where drops are jetted only when needed.[215]

In DOD method the ink is held in the chamber due to the surface tension of the fluid and a meniscus resides at the nozzle orifice until the droplet is ejected. In piezoelectric printers the droplet is squeezed out as a result of the changing dimensions of a piezoelectric element (Fig. 3.14.a). In thermal printers the droplet is ejected due to the pressure increase caused by a bubble formation at the heating element (Fig. 3.14.b). Therefore in contrast to the CIJ method, neither fluid recirculation nor charging of the droplets is required making the method far less complex than the CIJ. In DOD also the risk of contamination that may occur during ink recirculation is avoided making it likely a better option for biosensor applications.[216] Out of the various methods for droplet creation, the thermal and piezoelectric technologies are nowadays the dominating ones. Advantages of the piezo technology are the high printing speed because the ink requires no heating. This also eliminates the risk of damaging biological fluids by heating. Excellent accuracy in the amount of printed ink can be obtained as electrical charge is used to precisely control the piezoelectric element that drives the liquid from the reservoir through the orifice.

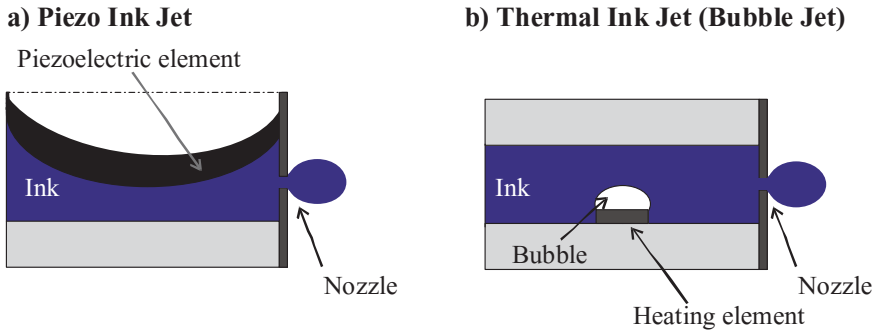

Fig. 3.14. Drop formation process of a a) piezo and b) thermal ink jet.

Durability of the print heads and the lower power consumption compared to the thermal system are factors that make piezo-inkjet a more environmentally friendly option.[217] Other advantages of the piezo heads are that the actuating waveform can be flexibly modified and that high boiling point solvents can be used.[218]

In order to perform high quality jetting, a perfect droplet creation is needed. There are several factors that influence the printability; mainly the physicochemical properties, e.g. particle size, viscosity and surface tension of the fluid and the electrical conditions (waveform) which often require optimization.

A parameter called the inverse Ohnesorge number (Oh^{-1}) can be used for estimating the printability of liquids or e.g. for selecting a cartridge with an optimal nozzle size if possible. It is defined as the ratio of the Reynolds number (N_{Re}) to the square root of the Weber number (N_{We}) thus relating viscosity, inertial and surface tension effects (Eq.3.36).

$$Oh^{-1} = \frac{N_{\mathrm{Re}}}{\sqrt{N_{\mathrm{We}}}} = \frac{\frac{va\rho}{\eta}}{\sqrt{\frac{v^2 a\rho}{\gamma}}} = \frac{\sqrt{a\rho\gamma}}{\eta} \tag{3.36}$$

where v, a, ρ, γ and η are the velocity of the drop, radius of the nozzle, the density, the surface tension and the viscosity of the fluid,

respectively. Jang et al.[219] determined experimentally the printability range to be Oh^{-1} = 4 – 14 and Meixner et al.[220] defined it to be 1 – 10. Too low values result in filament formation decreasing the print resolution and too large values on the other hand may not support droplet formation or lead to satellite drop formation. A solvent system with an intermediate Oh^{-1} value of about 7 can be obtained e.g. by mixing ethyl alcohol and ethylene glycol (volume fractions: 0.75:0.25).[219]

Disadvantages of inkjet-printing are e.g. the possibility for nozzle clocking during printing. Storage of the ink cartridges may cause a drying out of the cartridge. The printability window is rather narrow.[221] The viscosity is recommended to be within 1-40 mPa·s (preferably ca 10 mPa·s) and surface tension within 20-50 mN/m (preferably ca 30 mN/m). Also any particles in the ink should be about 100 times smaller than the nozzle diameter (21 μm, DMC-11610).[222]

3.4.2. Flexographic printing

The original concept of using rubber plates for printing was patented by J. A. Kinsley in 1853. However, the first flexographic printing press was built much later in UK by Bibby, Baron and Sons in 1890. The principle of the flexographic printing process closely resembles the oldest printing process called letterpress with the exception that the typically metallic types used in the letterpress were replaced by e.g. rubber plates. Printing on a wide range of materials and on challenging substrates such as corrugated paperboard and curved packages and containers became possible with the flexible relief plates. The use of mechanically engraved anilox rolls for metering the ink amount is considered as the central part of the modern printing process.[223] Later technological improvements in the manufacturing of both the anilox rolls and printing plates, have made flexographic printing a versatile and fast growing conventional printing technique with a promising forecast.[224] Recently EskoArtwork introduced the HD Flexo, which combines high resolution

plate manufacturing and excellent screening technology thus improving the print quality significantly.[225]

The modern flexographic printing process is schematically illustrated in Fig. 3.15. One advantage of flexographic printing lies in its roll-to-roll compatible nature and high speed printing of e.g. functional materials for transistors and solar cells.[226,227,228]

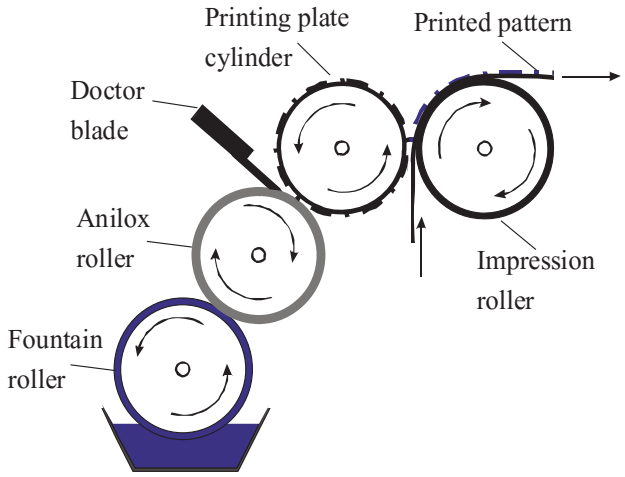

Fig. 3.15. Representation of the modern flexographic printing process.

Application of the ink from the ink pan on the anilox roll is done by the rotating rubber-covered fountain roller. The excess ink can be removed either by a doctor blade or by adjusting the pressure and speed of the rolls so that only the ink in the engraved cells in the anilox roll is transferred further to the raised image areas on the ink-receptive plate. From the cells the ink is transferred on the raised image areas on the printing plate. The ink is further transferred on the print substrate when it travels through the nip between the rotating printing plate cylinder and impression cylinder.

One of the benefits of flexography is its capability to operate with a variety of inks and substrates. A suitable viscosity range (50-500 mPa·s) is broad compared to e.g. inkjet printing (1-40 mPa·s)[229]. The properties of the anilox rolls as well as the printing plates can be adjusted to

facilitate optimal print quality for various inks such as water-based, UV-curable or oil-based. The properties of the anilox roll (line count, engraving angle, cell shape and the transferred volume) are especially important when printing conductive inks by a single pass.[230]

A schematic picture of the configuration of the laboratory scale printability tester used in this work is shown in Fig. 3.16.

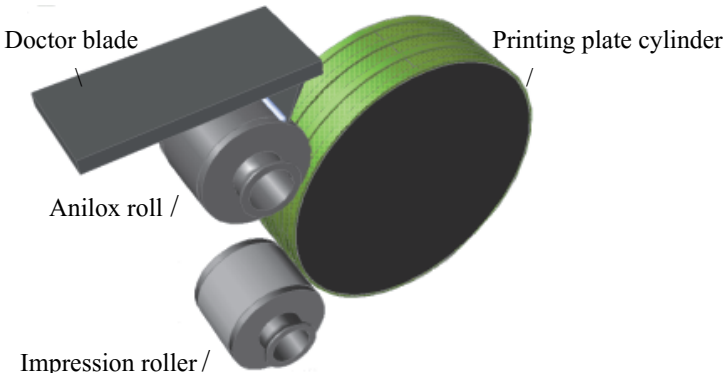

Fig. 3.16. Schematic illustration of the laboratory scale printability tester used in this study (**Papers I, II** and **V**).

3.4.3. Screen printing

The idea of using a stencil for patterning purposes is ancient. One of the earliest still remaining paintings created using leaves as stencils are located on Fiji.[231] Over the years the stencils have become more and more sophisticated. Silk fabric stencils were first used in China during the Song dynasty period over 1000 years ago. However, the screen-printing process and the use of silk fabric as the stencil were patented by Samuel Simon in UK in 1907. The number of factors influencing the print quality in screen printing is fairly large.[232] Stencil development and print quality optimization are in central role because higher and higher resolution and defect free prints are demanded.[233–235] Nowadays, the

stencils typically consist of nylon, polyester or metal. The principle of screen printing is shown in Fig. 3.17. (**Paper I**).

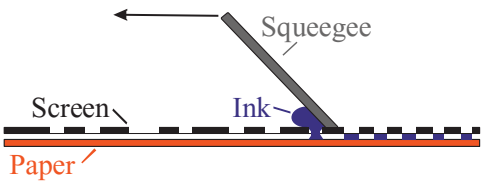

Fig. 3.17. Screen printing principle.

Traditionally, screen printing is used when viscous (500-50000 mPa·s) [229] inks are used and thick print layers are needed by one pass to e.g. ensure good conductivity. Noble metal electrodes for electrochemical sensor applications have been fabricated for decades by screen printing.[54,236] In addition, very thin, only several tens of nanometers thick, layers can be printed by screen printing if dilute solutions and fine stencils with high mesh counts (i.e. smaller mesh openings) are used.[237]

3.4.4. Reverse gravure coating

Reverse gravure coating method was developed for obtaining a reliable and reproducible way for coating smooth, uniform and thin coating layers.[238] The method is even suitable for coating a hydrophobic surface with a water-based formulation containing pigments (**Papers II–V**), something that would be cumbersome to carry out with e.g. a blade coater.[S15]

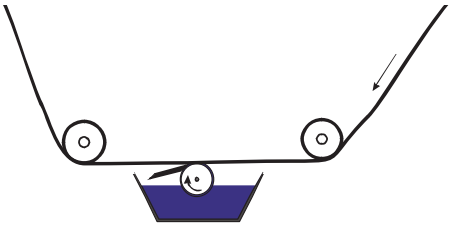

Fig. 3.18. Schematic illustration of the reverse gravure coating technique.

Fig. 3.18 shows a schematic illustration of the reverse gravure (RG) coating technique. The engraved cylinder is partially submerged in a pan that contains the coating solution. A blade is used to remove the excess coating, thus a predetermined amount of coating is applied on the paper. In addition to the engraving specifications, the coating thickness can be adjusted by the speed of rotation. The rotation direction is the opposite to the travel direction of the paper substrate, thus the coating is applied on paper in a shearing manner producing generally smoother coatings than obtained with film splitting methods. The absence of a backing roll reduces many nip-induced defects such as web breaks.

3.5. Print substrates and factors that influence adsorption and print quality

3.5.1. Roughness

Roughness of a paper substrate is an important factor affecting print quality. In conventional graphic printing the inks are deposited for visual purposes and both roughness and gloss of the paper substrate play a role for the pleasantness of the reading experience.[239] In printed functionality the deposited inks bring added value through a particular new functionality. The role of roughness may be drastic because the whole device or sensor performance may be impaired or short-circuited due to too large roughness.

Surface profilometers can be used for the characterization of isotropic surfaces and large length scale roughness, but they may fail to give reliable results for anisotropic substrates and surfaces with nanometer scale features. Usually papers that are intended to be used as substrates for printing of e.g. thin and smooth layers of nanoparticle-based inks are coated papers and relatively smooth. Such samples require high resolution surface characterization techniques such as AFM to be able to

analyse the information that contributes significantly to the function of the surface.

In addition to visual inspection, the AFM images can be analyzed for obtaining statistical information about the topography of the samples. Several roughness parameters are available for providing numerically representative information about the surfaces. The S_{dr} roughness parameter gives the real surface area (Fig. 3.19) as percentual increase compared to the flat projected area (Eq.3.37) (**Papers II, IV** and **V**). The measured surface area is sensitive to the image resolution. The most reliable S_{dr} value for a surface is therefore usually obtained from relatively small scale AFM topographs measured with high amount of pixels. For a totally flat surface, the factual surface area and the area of the xy plane are the same yielding an S_{dr} value of 0 %.

$$S_{dr} = \frac{\text{real surface area} - \text{projected area}}{\text{projected area}} \cdot 100\% \tag{3.37}$$

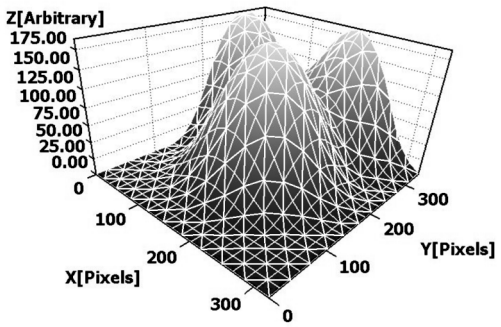

Fig. 3.19. The real surface area is obtained by calculating the total area of all the triangles formed over the texture.

The root mean square roughness (S_q) (**Papers I–V**) gives the standard deviation of the height values. The disadvantage of the S_q parameter is that it gives no information about the lateral distribution or height asymmetry of the surface features. For example the two model surfaces in Fig. 3.20. have exactly the same S_q value although the other sample contains peaks that are quite far away from each other and the other

sample consists of humps that are not as high but are more densely located. The S_q value is also dependent on the image size especially if the surface contains features like cells[240] or peaks (Fig. 3.20). A considerably lower S_q value would be obtained if the image area would be selected in an unrepresentative way so that such a peak would be excluded from the image.

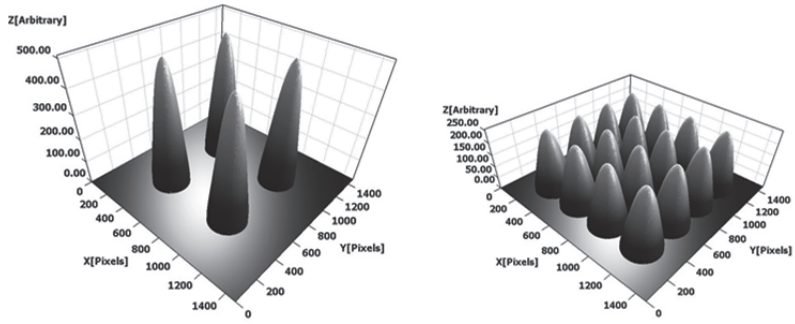

Fig. 3.20. Two model surfaces with different Z-range but same S_q value.

Before the roughness analysis is carried out for the measured images, usually fitting or filtering to some degree is required.[241,242] Typically, at least the tilt in the image caused e.g. by the sample not being horizontally placed is removed by subtracting a fitted first order polynomial function (cf. Fig. 3.21.a and 3.21.b).

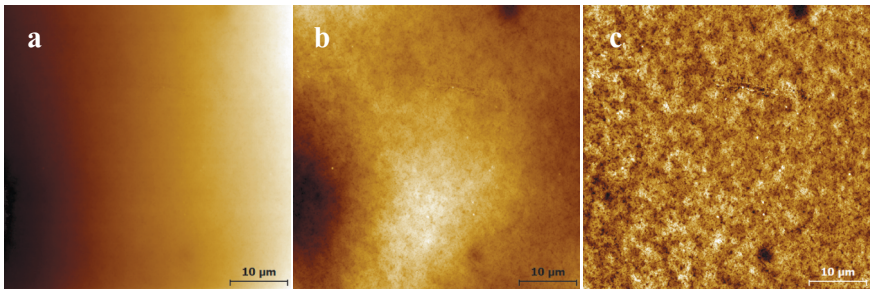

Fig. 3.21. An example of image processing: a) raw topographical image of Latex 2 sample with z-range 2601 nm, b) the same image after polynomial and LMS fitting, z-range 461 nm and c) after fitting and Gaussian (ISO 11562) filtering with relative cut off 1/5, z-range 305 nm.

In addition, coated paper substrates often contain waviness (or macro roughness). Filtering provides a way of separating the waviness that is superimposed with roughness (cf. Fig. 3.21.b and 3.21.c). Filtering also provides a way to reduce the scale-dependence of roughness as S_q can be presented as a function of a correlation length.

The dependence between two random variables (e.g. y and x that may be for example the height and length) can be determined by calculating the correlation coefficient r_c (Eq.3.38).

$$r_c = \frac{\sum_{i=1}^{n}(x_i - \bar{x})(y_i - \bar{y})}{\sqrt{\sum_{i=1}^{n}(x_i - \bar{x})^2 \sum_{i=1}^{n}(y_i - \bar{y})^2}} \tag{3.38}$$

A value of +1 corresponds to a perfect linear correlation and a value of –1 to a perfect linear anti-correlation. In a corresponding manner it is possible to determine the autocorrelation function (ACF), which is the similarity between a variable y(x) and the same variable after a shift y(x+τ) (for example a time delay τ or a shift in position).

The ACF for analyzing e.g. a roughness profile is defined as

$$ACF(\tau) = \frac{1}{x-\tau}\int_0^{x-\tau} y(x)y(x+\tau)dx \tag{3.39}$$

The areal ACF that is needed for analyzing a 3D surface topography is defined as

$$ACF(\tau_x, \tau_y) = \frac{\frac{1}{(z_x - \tau_x)(z_y - \tau_y)}\int_0^{z_x-\tau_x}\int_0^{z_y-\tau_y} z(x,y)z(x+\tau_x, y+\tau_y)dxdy}{S^2} \tag{3.40}$$

where S^2 is the variance of the z variable, S_q^2 in case of surface topographical analysis. If the shift τ is zero, the ACF has its maximum value, one. As the shift increases the ACF value typically decreases

approaching theoretically 0.[243] When the ACF has decreased for example to a value of 0.5, the horizontal shift gives the correlation length (T_{50}). A correlation length corresponding to a decay to a value of e^{-1} (T_{37} or S_{cl37}) was used in this study. The correlation lenght can be considered as the length for which single height readings for a random surface become statistically independent of one another.[244]

By filtering the AFM topographical images with different cut off values (i.e. by subtracting various length scale waviness), the roughness (S_q) can be calculated as a function of T_{37}.

If anisotropic samples containing e.g. organized linear structures are in question, the correlation length is different for different directions. Perpendicular to the surface lay the correlation length is much smaller than in the direction parallel to the lay. Parameter S_{tr37} gives information about the strength of the texture and it is defined as the ratio of the fastest to slowest decay to 37% of the autocorrelation function. Therefore it may be convenient to calculate instead the average correlation length T_a which is defined as

$$T_a = \frac{\frac{S_{cl37}}{S_{tr37}} + S_{cl37}}{2} \tag{3.41}$$

Detailed analysis of the evolution of roughness as a function of correlation length has been used for estimating the required pressure needed during flexographic printing in order the relief plate to get into contact with the deepest valleys of the substrate.[245] This kind of roughness analysis could be useful also when considering the amount of ink needed for printing thin and continuous films.

3.5.2. Contact angle and surface energy

Contact angle (CA) measurements of sessile droplets offer a convenient, inexpensive and perhaps the most surface sensitive method for obtaining information about a sample (**Papers I–IV**). CA measurements are frequently carried out for indirect measurement of the surface energy of the substrates for predicting e.g. adhesion between a substrate and an ink. A general rule of thumb is that the surface energy of a solid should be at least 7-10 mN/m higher than the surface tension of the ink or the coating paste in order for the print/coating quality to be acceptable, e.g. with no unwanted dewetting.[246] Modern CA instruments utilize a high-speed camera and a computer for analyzing the shapes and contact angles of the droplets. Several assumptions are made when the CA values are used for determining the surface energy of the solid samples. For example, it is assumed that the droplet spreads symmetrically in all directions and that only gravity and interfacial tension are shaping the droplet and not for example inertia.[247] Young's equation[248] (Eq.3.42), that is valid for an ideally flat, horizontal, rigid, chemically homogeneous, insoluble and nonreactive surface, may be used to express the relationship between the contact angle and the three interfacial tensions according to

$$\gamma^{SV} = \gamma^{SL} + \gamma^{LV} \cos\theta \tag{3.42}$$

where γ^{SV} is the solid-vapor interfacial tension (surface tension of the solid), γ^{SL} is the solid–liquid interfacial tension and γ^{LV} is the liquid-vapor interfacial tension (surface tension of the liquid). The interfacial tensions shown as vectors in Fig. 3.22 represent the forces that act upon the liquid at the three-phase contact line. The Young's equation states that at equilibrium the horizontal forces acting on the opposite directions are in balance.

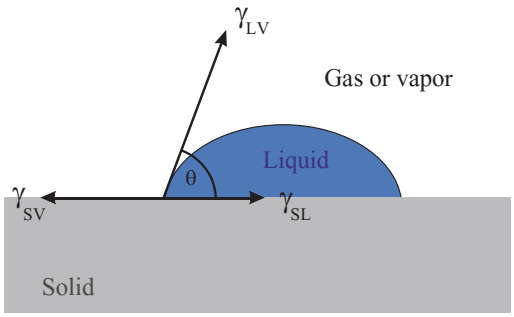

Fig. 3.22. The components of interfacial tension between solid and a liquid, γ^{SL}, between solid and vapor, γ^{SV}, and between liquid and vapor, γ^{LV}.

In order to solve γ^{SV} and furthermore to divide it into a polar and dispersive components, Owens, Wendt, Rabel and Kaelble[249,250] used the equations 3.43-3.44 and 3.45 (similar to the one introduced by Girifalco and Good[251]) and combined them with Young's equation to get equations 3.46-3.47.

$$\gamma^{LV} = \gamma^{LV(p)} + \gamma^{LV(d)} \tag{3.43}$$

$$\gamma^{SV} = \gamma^{SV(p)} + \gamma^{SV(d)} \tag{3.44}$$

$$\gamma^{SL} = \gamma^{SV} + \gamma^{LV} - 2\left(\sqrt{\gamma^{SV(d)} \cdot \gamma^{LV(d)}} + \sqrt{\gamma^{SV(p)} \cdot \gamma^{LV(p)}}\right) \tag{3.45}$$

$$\gamma^{SV} = \underbrace{\gamma^{SV} + \gamma^{LV} - 2\left(\sqrt{\gamma^{SV(d)} \cdot \gamma^{LV(d)}} + \sqrt{\gamma^{SV(p)} \cdot \gamma^{LV(p)}}\right)}_{\gamma^{SL}} + \gamma^{LV}\cos\theta \tag{3.46}$$

$$\gamma^{SV} = \gamma^{SV} + \gamma^{LV} - 2\left(\sqrt{\gamma^{SV(d)} \cdot \gamma^{LV(d)}} + \sqrt{\gamma^{SV(p)} \cdot \gamma^{LV(p)}}\right) + \gamma^{LV}\cos\theta \tag{3.47}$$

By taking the γ^{LV} as the common factor, the equation can be simplified and transformed into a general first order equation (Eq.3.48).

$$\underbrace{\frac{(1+\cos\theta)\gamma^{LV}}{2\sqrt{\gamma^{LV(p)}}}}_{\text{y}} = \underbrace{\sqrt{\gamma^{SV(p)}}}_{\text{slope}} \cdot \underbrace{\sqrt{\frac{\gamma^{LV(p)}}{\gamma^{LV(d)}}}}_{\text{x}} + \underbrace{\sqrt{\gamma^{SV(d)}}}_{\text{intercept}} \tag{3.48}$$

By measuring contact angles with at least two liquids with known dispersive and polar components and the total surface tension, the dispersive and polar components of the solid surface energy can be determined. Alternatively, as suggested by Rabel, CA measurements can be carried out with several liquids and the slope of the plot y versus x gives the square of the surface energy of the solid and the dispersive component of the surface energy of the solid is obtained from the square of the y-axis intercept. When the polar and dispersive components of a given solid are known, a so-called wetting envelope can be created that can be used for determining the wetting behaviour of liquids with known polar and dispersive components.[252]

Wenzel's model[253] was used for taking into account the roughness of the substrates on the measured contact angles (**Paper II**). The S_{dr} parameter values obtained from the AFM topographical measurements were used for obtaining the roughness factor, *r*

$$r = \left(1 + \frac{S_{dr}}{100}\right) \tag{3.49}$$

that is needed for correcting the apparent contact angles for roughness by the Wenzel's equation[253,254]:

$$\cos\theta_a = r\cos\theta_r \tag{3.50}$$

where θ_a is the measured equilibrium contact angle and θ_r is the contact angle for a smooth surface. The Owens-Wendt method, where the

total surface energy (γ_s) is determined as the sum of the polar (γ_s^p) and dispersive (γ_s^d) components was used for the surface energy determination in **Paper II**.[249] The values of surface tension components suggested by van Oss et al. were used for the probe liquids.[255,256]

4. MATERIALS AND METHODS

4.1. Print substrates

In **Paper I**, printing of the planar reaction arrays was demonstrated on various commercial substrates with varying barrier properties. Whatman Filter paper (cellulose, Grade 1) and Steri-Pak LF indicator test sheets were selected for their high permeability and water absorbing capacitance; surface sized copy paper (Optitext, Stora Enso, Finland) for its low cost, abundance and intermediate water absorbance; a typical coated paper, Lumiart (Stora Enso, Finland) for its relatively slow water and air permeance; and a non-wettable and flexible plastic polyethylene terephthalate (PET, Mylar®A, Dupont Teijin Films Europe, Luxembourg)) film for its excellent barrier properties.

In **Paper II**, the planar reaction arrays were exposed to liquid media and bacteria culturing for long periods of time and therefore paper substrates with good barrier properties were used.[S4,S5] Four different types of laboratory coated papers including two latex blend coated substrates (Latex 1, Latex 2) and two mineral pigment coated substrates (Precipitated calcium carbonate (PCC) and Kaolin) were fabricated. A basepaper coated with ground calcium carbonate (GCC, 90 g/m^2) was used as a substrate for all the coated grades. The Latex 1 coating consisted of a 2:3 blend of a film-forming styrene acrylate (SA) latex with low glass transition temperature (T_g) and a nonfilm-forming high-T_g polystyrene plastic pigment (particle size 100 – 200 nm). For the Latex 2 coating a low-T_g film forming styrene butadiene (SB) latex was used, blended with the same high-T_g polystyrene plastic pigment as in Latex 1, with a mixing ratio 3:2. The latex coatings were reverse gravure coated on the basepaper. In case of the pigment coated papers, a smoothing layer was first blade-coated on the basepaper, then a barrier coating was coated on top of the smoothing layer and finally a top coating was coated on top of the barrier layer. The mineral pigment – based thin top coatings included 7 pph of styrene butadiene latex as a

binder and carboxymethyl cellucose (CMC) as a thickener.[S5] The latex-based coatings were IR-sintered for approximately 1 min in order to thermally modify the topography to gain a bimodal structure with an increased surface area and improved adhesion for biomaterials.[S23] The pigment-based substrates were calendered at a nip pressure and temperature of 50 bars and 70°C and Latex 1 and Latex 2 substrates at 70 bars and 35°C, respectively. Printed and cured PDMS surfaces and traditional 96-well plates made of polystyrene were used as reference substrates in the biofilm forming studies.

In the **Papers III–V**, a paper substrate coated with kaolin pigments was used owing a relatively low roughness and good barrier properties against organic and aqueous solvents. Atomically flat mica with an evaporated gold layer, polyethylene naphthalate (PEN) and glass substrates were used as reference substrates in **Papers III**, **IV** and **V,** respectively.

A polyethylene terephthalate film (PET, Mylar®A, DuPont Teijin Films) and recently furher developed coated paper substrates were also used as reference substrates and some data is presented in chapter 5. A Latex 3 substrate (unpublished) was prepared by applying the same coating recipe that was used for Latex 2 on a PCC coated paper using either a K Control Coater (RK Print-coat Instrument Ltd, UK) with a coating rod 16M and coating speed 3 m/s or a reverse gravure coater. A multilayer curtain coated (MLCC) paper substrate was manufactured at Metso's Pilot machine (OptiCoater, Järvenpää, Finland).[S12,257,S22] The top coating layer (5 g/m^2) consisted of Basonal 2020.5 (6 pph, BASF, GER) styrene-butadiene latex, Barrisurf FX (70 pph, Imerys Minerals Ltd, UK) and Alphatex (30 pph, Imerys Minerals Ltd, UK) kaolin pigments. A synthetic thickener (HPV 56, DOW, CH) was used to adjust the viscosity to 350 mPa·s and a surfactant, Lumiten I-SC (Basf, GER), to adjust the surface tension to 37 mN/m. The barrier layer (10 g/m^2) consisted of Barrisuft HX (Imerys Minerals Ltd, UK) kaolin pigments blended with Aquaseal 2077 (50 pph, Paramelt B.V., NL) ethylene acrylic latex. Carboxymethyl cellulose (Finnfix 10, CPKelco) was used

to adjust the viscosity to 350 mPa·s and Lumiten I-SC (Basf, GER) to adjust the surface tension to 35.8 mN/m. Lumipress (115 g/m^2, Stora Enso) was used as the base paper.

4.2. Ink formulations

The flexographically printed PDMS-based ink used in **Papers I, II**, **III** and **V**, consisted of a 100:2.5:1 wt% blend of vinyl-substituted polydimethylsiloxane (Dehesive®920): Catalyst OL: crosslinker V24 (Wacker Chemie). The crosslinker-component (e.g. 0.5 g) was first slowly added into Dehesive®920 (20 g) and then mixed for 5 min at room temperature. Next 0.2 g of the catalyst-component was slowly added to the mixture and the ink was further stirred for 10 min. Crosslinking was completed by heating (Fig. 4.1) either in an oven or by IR treatment approximately 10 s.

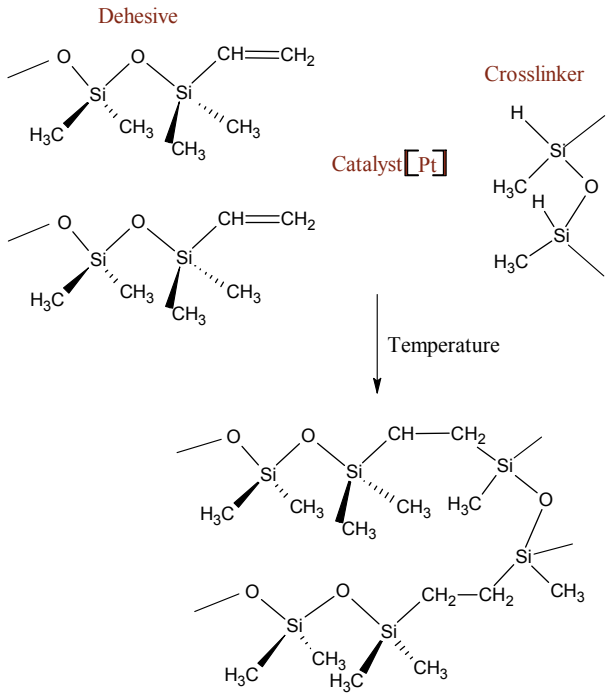

Fig. 4.1. Crosslinking of the PDMS ink. [258]

In **Papers I** and **III,** the PDMS ink was modified to be suitable for inkjet printing by diluting the Dehesive®920 component (dynamic viscosity: 500 mPa·s[259]) with xylene (mixture of isomers) (Dehesive®920: Xylene, 2:3 vol.).

The enzymatic ink used in **Paper I** consisted of polyvinyl alcohol (PVA, Mowiol® 10-89), starch, potassium iodide (KI), molybdic acid and glucose oxidase (GOx). Viscosity of an aqueous PVA solution (4%) at 20°C is 9-11 mPa·s[260] making the ink suitable for screen printing. Also the activity of e.g. a laccase enzyme has been shown to be well maintained in (PVA).[261]

The thiol-capped gold nanoparticles (size 3-5 nm) that were used to prepare the AuNP-based ink (**Papers III**–**V**) were obtained from the University of Helsinki.[S11] The particles were synthesized following the procedure reported by Hostetler et al.[262] The AuNPs (15 wt.%) were dispersed in xylene (mixture of isomers) with a boiling point of ~ 140°C, viscosity of <1 mPa·s and surface tension of ~ 30 mN/m.

In **Papers IV** and **V**, a commercial silver nanoparticle (AgNP) ink was used (SunTronic U5603, 20 wt.%). The particle size of the AgNPs was 30–50 nm and they were dispersed in ethylene glycol/ethanol/glycerol solution. Unpublished printing tests were carried out with SunTronic Jet silver U5714 (40 wt.%).

4.3. Surface Characterization Methods

4.3.1. Atomic Force Microscopy (AFM)

Atomic Force Microscope was patented and introduced in 1986 by Binnig et al.[263,264] The significant advantage of AFM compared to its forerunner scanning tunneling microscope (STM)[265] is that with AFM various kinds of samples can be imaged, unlike with the STM, the drawback of which was the limitation to analysis of only conducting or

semiconducting samples. STM and AFM belong to the family of scanning probe microscopes (SPM) that create an image of a surface by using a physical probe that scans the sample.

Fig. 4.2. shows a schematic representation of the components and the working principle of an AFM. Typically a sharp needle-like tip that is attached to a cantilever is set to oscillate using a piezocrystal in the cantilever holder. While the tip is oscillating and probing the surface the sample is accurately moved by a piezoelectric scanner in x, y and z directions. Interaction forces (repulsive/attractive) between the tip and the sample tend to bend the cantilever, and also change the amplitude and phase angle of the oscillation. These changes are used to provide information about the surface. The cantilever deflection can be monitored by focusing a laser at the end of the cantilever from where it is reflected to a photodiode. With a help of a feedback loop between the piezoelectric scanner and the photodiode, the oscillation amplitude can be kept constant during scanning by adjusting the sample position in z-direction. The position of the piezoelectric scanner is recorded typically 512 or 1024 times during each scan sweep to provide the topographic data. The changes in the phase angle (difference between the oscillation of input and response signal) at different positions of the sample give information about the local compositional variations e.g. in adhesion and viscoelasticity of heterogeneous samples.[266] This mode was used in **Papers I–V**.

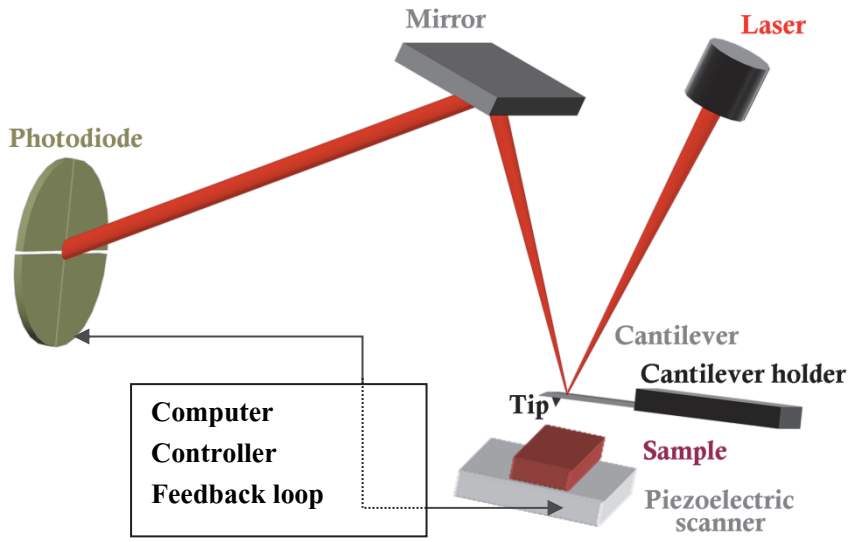

Fig. 4.2. The principle of an AFM instrument.

The imaging mode measuring surface potential (SP) was used in **Papers III** and **IV**. The method is a combined two-pass technique. The topography is measured using TappingMode and this topographical information is used for tracking the probe at a constant height (ca. 20 nm) above the surface during the surface potential measurement. As the tip travels above the surface it experiences a force whenever there is a potential difference between the tip and the sample. The voltage applied to the tip is adjusted so that the sample and the tip have the same potential. A surface potential map for a sample is obtained by plotting the voltage applied to the tip during the x-y scanning.

The number of different SPM modes has increased during the years. One of the most recent innovations is the PeakForce QNM™ (quantitative nanomechanical mapping) that is mapping the material properties (modulus, dissipation and deformation) and adhesion between the tip and the sample at high resolution simultaneously with the topography of the surface.[267,268] The mode is based on measuring force curves at a non-resonant mode, typically with a frequence of 2 kHz. The novelty of this mode is that the z-position is not modulated by a

triangular wave like in conventional force curve measurements but with a sine wave. Since force curves are measured and analysed at each point, the force is accurately controlled which protects the tip and the sample from damage. A Nanoscope V AFM (Multimode TM series, Digital Instruments, Veeco Metrology Group, Santa Barbara, CA) was used for the SP and PeakForce QNM™ measurements and Ntegra Prima (NT-MDT, Russia) for topographical and phase measurements. The experimental details are given in **Papers I–V**.

4.3.2. X-ray photoelectron spectroscopy (XPS)

XPS is a surface characterization method where the sample is irradiated with a well defined beam of x-rays (photons).[269] The collisions between the photons and the electrons in the sample result in electrons being emitted from the sample with a specific kinetic energy depending on the binding energy of the electrons. The binding energies vary according to the element in question and the neighboring chemical bonds. Thereby information about the chemical composition of the sample can be obtained. The binding energies are calculated using equation 4.1

$$E_{\text{binding}} = h\upsilon + E_{\text{kinetic}} - \phi_s \tag{4.1}$$

where $h\nu$ is the photon energy (for aluminium x-ray source 1486.6 eV), E_{kin} is the kinetic energy of the emitted electrons and ϕ_{s} is the spectrometer work function.

Although the x-ray photons penetrate relatively deep inside the sample, the probability of the electron emission decreases fast as a function of depth making the technique fairly surface sensitive. The detected photoelectrons come from the top 10 nm.[269] The XPS measurements for this thesis (**Papers III** and **IV**) were carried out using a PHI Quantum 2000 scanning spectrometer.

4.3.3. Contact angle measurements

The contact angle measurements were carried out using a CAM 200 contact angle goniometer (KSV instrumetns Ltd., Helsinki, Finland). Usually a drop of 1-3 μL was gently deposited on the sample surface and the contact angle was measured as a function of time. The measured equilibrium contact angle values were obtained at the point where the diameter of the drop in contact with the surface, contact angle and drop volume remained constant.

4.4. Printing and Coating Techniques

4.4.1. Inkjet printing

Inkjet printing in this thesis (**Papers I**, **III**, **IV** and **V**) was carried out using a piezoelectric drop-on-demand Dimatix™ Materials Printer (DMP-2800, FUJIFILM Dimatix, Inc. Santa Clara, USA). A replaceable cartridge (DMC-11610) with a 10 pL nominal drop volume was used. A firing voltage of 27 V and 18 V was used for printing of the gold and silver inks, respectively. A custom waveform and a firing frequency of 2 kHz were used to ensure reproducible droplet formation. The print patterns were designed by the Dimatix Drop Manager pattern generator software supplied together with the printer when images consisting of simple block patterns were printed with a constant and standard drop spacing (DS) value (e.g. DS 5, 10, 15, 20, 25, 30, 35 or 40 μm). Equation 4.2 gives the number of dots in a simple rectangle print pattern

$$\text{Number of dots} = \left(\frac{X}{DS}+1\right)\left(\frac{Y}{DS}+1\right) \tag{4.2}$$

where X and Y are the dimensions of the printed rectangle and DS is the drop spacing.

Fig. 4.3 presents the number of dots as a function of DS when X = Y = 1000 µm. The difference in the printed ink amount for example between the two lowest standard DS values (5 µm and 10 µm) is relatively high.

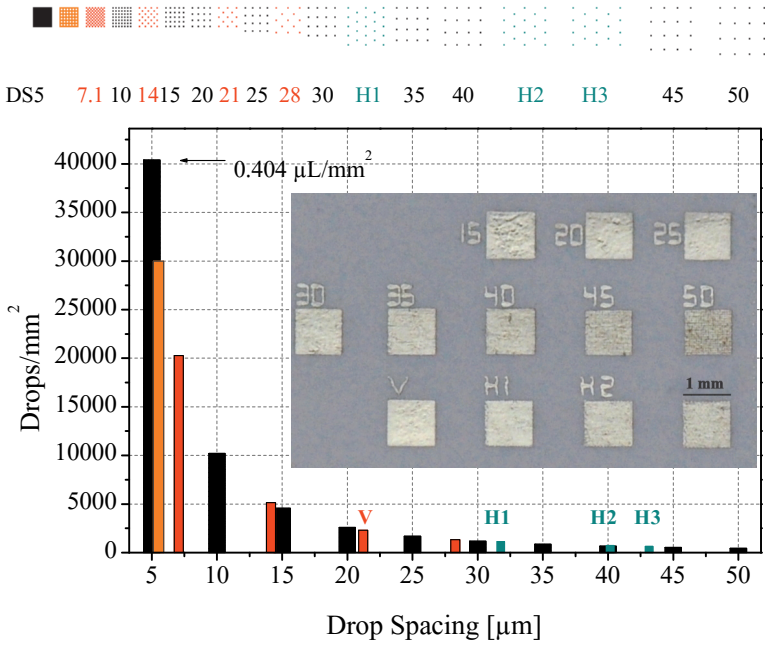

Fig. 4.3. Dot patterns and the number of printed drops as a function of DS for a print design pattern with an area of 1 mm2. Also shown is a photograph of the silver squares printed with different DS values and specific patterns.

Microsoft Paint and the Gnu Image Manipulation Program (GIMP) were used for creating print patterns with intermediate ink amounts (some examples are shown in colour, Fig. 4.3.) allowing fine tuning of the amount of the printed ink. Also when round patterns or areas with varying drop spacings were printed simultaneously (**Paper III**), Microsoft Paint or GIMP programs were found to be convenient for designing the patterns. The digital photograph inset (Fig. 4.3) shows that the print quality of all the squares at the bottom row (V, H1, H2, H3 patterns) appears optically rather homogeneous when comparing to the patterns printed with the standard DS values. The H2 pattern appears

slightly lighter than DS35 and H3 slightly lighter than DS 40, although the ink amounts used in the hexagonally printed areas were lower.

4.4.2. Flexographic printing

The flexographic printing jobs were carried out with a laboratory scale printability tester (IGT Global Standard Tester 2, IGT Testing Systems, The Netherlands) (Fig. 3.16) at a temperature of 23 °C and relative humidity (RH) of 50%. An anilox roll with a cell angle of 45°, cell volume of 20 mL/m^2 and a line count of 40 l/cm was used. The patterned photopolymer printing plates (Ohkaflex, thickness 1.7 mm) were purchased from Espoon Painolaatta, Finland. The following printing parameters were used: printing speed: 0.5 m/s, pressure between the anilox roll and the printing plate: 100 N, pressure between the printing plate and substrate: 50 N. In addition, a demonstration of roll-to-roll manufacturing of the printed planar reaction arrays (**Paper I**) was carried out by a custom build hybrid printer[270,271] using a Ohkaflex photopolymer printing plate, an anilox with a cell volume of 30 mL/m^2 and a printing speed of approximately 7 m/min.

4.4.3. Screen printing

Screen printing in **Paper I** was carried out by using a TIC SCF-260B screen printer (Technical Industrial Co. Ltd., Hong Kong) equipped with a 380 Mesh screen fabric (Sefar PET 1500 150/380-34, Sefar, Switzerland). The nominal thread diameter in the plain weave was 34 µm, mesh opening 23 µm, mesh thickness 55 µm and theoretical ink volume 6.7 mL/m^2. Printing settings were precision adjusted using vernier calipers and the horizontal average sweep rate of the squeegee was 200 mm/s.

4.4.4. Reverse gravure coating

Reverse gravure coatings were carried out either by a commercial MiniLabo coater (Yasui Seiki Co., Japan) or a custom-build reverse gravure unit in a custom-built roll-to-roll hybrid printer.[272]

4.4.5. Thiolation of the electrodes

Self-assembled monolayer experiments in **Papers III–V** were conducted using 1-octadecanethiol (ODT, Fluka Chemica). Prior to the thiolation, the gold electrodes were cleaned with air plasma flow (PDC-326), Harrick) for 2 min, rinsed with acetone and absolute ethanol and dried with nitrogen gas. The silver electrodes were cleaned by rinsing with absolute ethanol and acetone. The SAMs were formed by exposing the electrodes to a solution containing 5 mM of ODT in ethanol for 0.5–2 h at room temperature. After the thiolation the electrodes were rinsed with absolute ethanol and dried with nitrogen gas.

4.5. IR sintering

An IR drier consisting of three 30 cm long 2 kW strip light bulbs (IRT systems, Hedson Technologies AB, Sweden) was used for the offline sintering of the silver and gold electrodes, curing of the PDMS ink and for the thermal modification of the Latex-based samples. The online curing of the PDMS ink was done using two 500 W infrared sintering units (HQE500, Ceramicx, IRL).

4.6. Biofilm formation and CFU counts

In **Paper II**, the paper substrates patterned with PDMS were used as substrates for biofilm formation studies using *Staphylococcus aureus*

(ATCC 25923) as the model biofilm-forming bacteria. First the bacteria were cultured in Tryptic Soy Broth (TSB) under aerobic conditions at 37°C and 200 rpm. The paper platforms with four wells were then placed into plastic 6-well plates and 5 mL of bacterial suspension with a concentration of colony forming units (CFU) of 10^6 CFU/mL was added. The biofilms were allowed to form for 18 h. To quantify the susceptibility of the different paper substrates to biofilm formation, the cells were scraped off the substrates using sterile plastic sticks. The bacterial aggregates were then dispersed using an ultrasonic bath and the disaggregated biofilms were serially diluted, spread onto Tryptic Soy Agar (TSA) plates and incubated at 37°C overnight. Viable bacterial cell densities were quantified and expressed as CFU/cm^2.

4.7. Electrochemical analysis equipments

4.7.1. Voltammetric measurements

In order to evaluate the performance of the paper-based platforms with inkjet-printed golden working and counter electrodes and an Ag/AgCl quasi reference electrode, cyclic voltammetry (CV) experiments were performed. An Autolab General Purpose Electrochemical system (AUT20.FRA2-Autolab and AUT30.FRA2-Autolab, Eco Chemie, B.V., the Netherlands) was used. Potassium ferri(III)cyanide/ferro(II)cyanide ($K_3/K_4[Fe(CN)_6]$) solution in 0.1 M KCl was used as a model analyte solution while verifying the performance of the printed paper-based electrochemical platforms. Five CV cycles with a potential range between −0.3 and 0.6 V (vs. Ag/AgCl reference electrode) were recorded at different scan rates (20–500 mV/s) and analyte concentrations in unstirred conditions with an analyte volume of approximately 0.1–0.5 mL. The magnitudes of the anodic and cathodic peak currents during the fifth cycle were analyzed by the GPES software supplied with the Autolab instrument. Corresponding measurements

were carried out in a conventional electrochemical cell where the WE was a gold disk (A_{WE} = 1.936 mm^2), the counter electrode was a glassy carbon rod and the reference was either a commercial Ag/AgCl/3 M KCl reference electrode (Metrohm) or a disk-shaped Ag/AgCl quasi-reference electrode. The electropolymerization of aniline was carried out by cycling the potential between −0.2 and +0.7 V (vs. Ag/AgCl) at a scan rate of 50 mV/s in an acidic aqueous solution containing 0.1 M freshly distilled aniline monomer and 0.5 M HCl.

4.7.2. Potentiometry

Potentiometric pH measurements were done with a Lawson EMF16 Interface potentiometer (Lawson Labs, Inc.) (**Paper V**).

4.7.3. Electrical Resistance Measurements

A Keithley 2100 Digital Multimeter (Keithley Instruments Inc., Cleveland, USA) was used for measuring the resistance (R) of the printed electrodes and for determining the electrical resistivity (ρ) of the printed materials (Eq.4.3) (**Paper III**).

$$\rho = R\left(\frac{Wd}{L}\right) \tag{4.3}$$

In equation 4.3 ρ is the resistivity [Ωm], W is the width [m], d is the thickness [m] and L is the length [m] of the printed line.

4.7.4. Electrochemical Impedance Spectroscopy Measurements

Impedance measurements in **Paper IV** were carried out using a Gamry 600 impedance spectrometer. A buffer solution (pH 7.4) was used as the electrolyte solution and the frequency range during the measurements

was from 1 MHz to 1Hz. The amplitude of the ac-signal was 20 mV and the dc-potential was 100 mV. The capacitance value that was automatically calculated by the analyzing software (Eq.4.4) was plotted as a function of frequency and used for demonstrating the influence of the insulating SAM.

$$C_{real} = -\frac{Z'}{\left((Z')^2 + (iZ'')^2\right) 2\pi f A} \tag{4.4}$$

Impedance measurements in **Paper V** were carried out using the Autolab instrument. 0.1 M KCl was used as the electrolyte solution and the frequency range during the measurements was from 10 kHz to 0.01 Hz. The amplitude of the ac-signal was 10 mV. The dc-potential of the EIS measurements corresponded +0.2 V vs. Ag/AgCl/3 M KCl.

5. RESULTS AND DISCUSSION

The main results of the thesis are presented in the **Papers I–V** and this chapter is a summary of them. In addition, extended analysis and unpublished supporting results are presented.

5.1. Properties of the print substrates

The apparent contact angles, S_{dr} values of the substrates and roughness corrected contact angle values of the probe liquids are listed in Table 3. The polar and dispersive surface energy components and the total surface energy of the print and reference substrates are also included in Table 3 (**Paper II**). The main differences in the surface energies between these paper substrates arise from the differencies in the polar component values. Generally, a high amount of polar substances with dipole moments such as hydroxyl (-OH) groups gives rise to a high polar component value. Good examples of substances with high polar components are cellulose and hydroxy-terminated SAMs (e.g. 4′-hydroxy-4-mer- captobiphenyl with a surface energy of ~67 mN/m[273]). Also kaolinite ($Al_2(Si_2O_5)(OH)_4$) and calcite ($CaCO_3$) minerals that are used in the paper coatings have high surface energies and polar component values. The dispersive and polar surface energy components calculated for pure kaolinite are 67.6 mN/m and 103.4 mN/m, respectively.[274] The γ^d value for calcium carbonate has been reported to be 103.3 mN/m[275] and the total surface energy 200 mN/m[276]. In practice the pigments are treated with dispersing agents, e.g. sodium polyacrylate (NaPA), to facilitate more stable dispersions and lower viscosity in the coating pastes.[277] For example the surface treatment of calcium carbonate with stearic acid ($CH_3(CH_2)_{16}CO_2H$, 90% coverage) has been shown to lower the dispersive surface energy component to a value of approximately 29 mN/m, which is between the values that are observed for surfaces that are composed of alkyl chains: CH_2: 35 mN/m; CH_3: 24 mN/m.[275]

Taking into account that the pigment coated papers also include SB latex which at least partly covers the pigments[S9], the lower surface energy values obtained for the pigment coated papers compared to pure pigments are reasonable. Information about the possible additives, e.g. surfactants that the commercial latex suspensions may contain was not available. The Wenzel's model (Eq.3.50) yields quite nicely similar roughness corrected contact angle values and surface energy values for the MLCC samples calendered two and three times although the apparent contact angle values vary quite much. This shows that substrates with similar chemistry may have rather different wetting properties purely arising from different roughness. For $MLCC_{2x}$ the difference between the apparent and the roughness-corrected contact angle for water is as large as 25 degrees. Further calendering decreases the difference to 17 degrees (sample $MLCC_{3x}$), which is logical due to decreased roughness.

Table 3. Apparent contact angles, S_{dr} values of the substrates and roughness corrected contact angle values of the probe liquids, polar and dispersive surface energy components and the total surface energy of each print and reference substrate.

	Apparent contact angles				Roughness corrected contact angles		
Substrate	H_2O [°]	DIM [°]	EG [°]	S_{dr} [%]	H_2O [°]	DIM [°]	EG [°]
PCC	93 ± 3	30 ± 1	30 ± 2	42.0	92	52	52
Kaolin	56 ± 2	36 ± 1	34 ± 1	25.0	64	50	48
Latex 1	84 ± 1	52 ± 1	73 ± 1	1.6	84	52	73
Latex 2	72 ± 3	41 ± 2	55 ± 2	10.0	74	47	59
$MLCC_{2x}$	15	54.5	16.5	25.6	40	62	40
$MLCC_{3x}$	25[257]	57[257]	29[257]	22.7	42	63	45
PET	84[S5]	31[S5]	54[S5]	0.8	84	32	55
96-well Plate	80 ± 1	37 ± 2	53 ± 2	0.3	80	37	53
PDMS	114 ±1	92 ± 2	96 ± 1	0.1	114	92	96

Surface energy components and the total surface energy			
Substrate	γ^p [mN/m]	γ^d [mN/ m]	γ^{tot} [mN/m]
PCC	1.4	34.7	36.1
Kaolin	12.2	29.9	42.1
Latex 1	3.4	27.8	31.2
Latex 2	6.6	31.3	37.9
$MLCC_{2x}$	30.9	21.3	52.2
$MLCC_{3x}$	29.6	20.6	50.2
PET	1.7	40.8	42.5
96-well Plate	3.2	38.2	41.4
PDMS	0.6	11.7	12.3

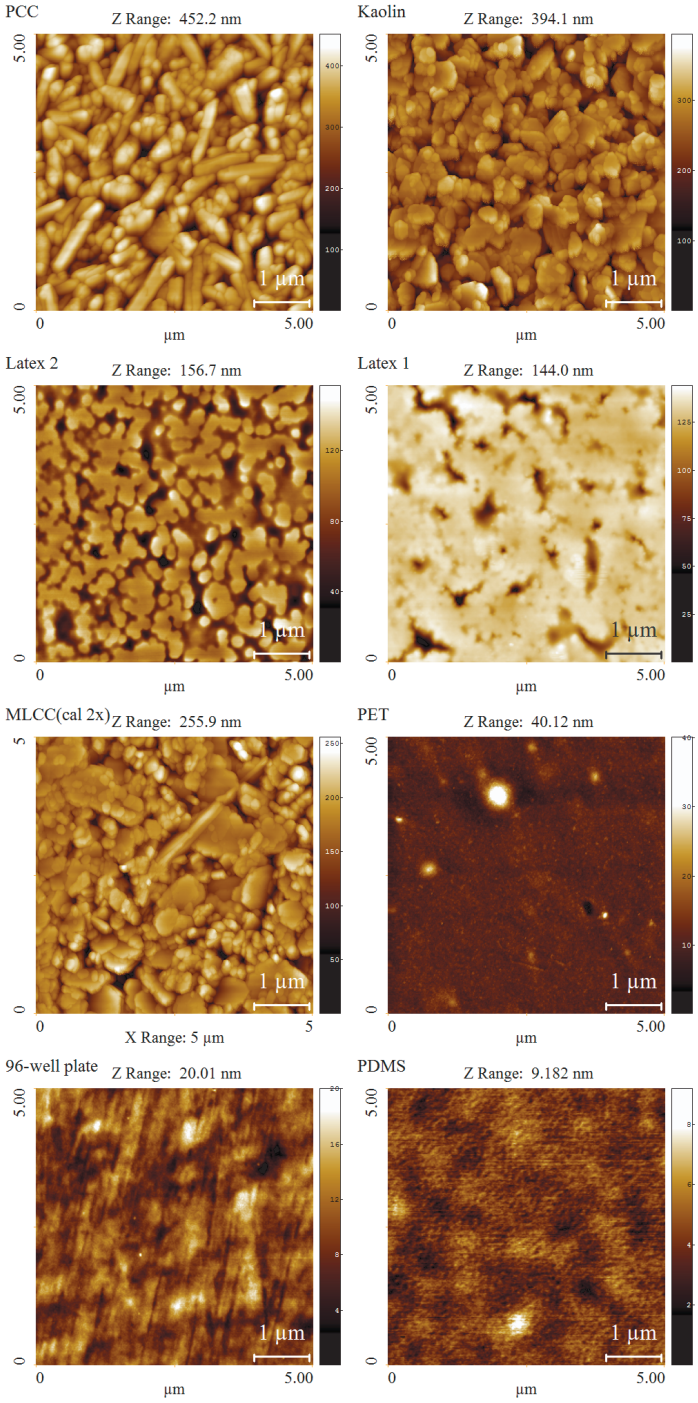

Fig. 5.1. AFM topographical images of the studied Coated papers and reference substrates (MOD. from **Paper II**).

Fig. 5.1 shows typical small scale (5 μm × 5 μm) AFM topographical images of the coated paper substrates and the reference substrates used in this thesis. The pigment-based coatings are clearly the roughest among the studied samples with the highest z-range and S_{dr} values (Table 3). The topograph of the $MLCC_{2x}$ sample represents the surface after being calendered twice. The pigment-based surfaces consist of randomly oriented rod-like PCC pigment particles or platy Kaolin pigments bound together by the SB latex.[S9]

The IR-treated latex-based surfaces consist of flat top areas abruptly interrupted by grooves and recesses. The result is a quite column-like surface morphology, especially in case of Latex 2. The structured morphology is a result of deformation and local coalescence of phase separated hard polystyrene particles within the film forming SB layer.[278] The nonporous plastic PET sheet appears otherwise smooth, but it contains relatively high surface peakedness. The surface texture of the 96-well plate is generated by the molding process. The PDMS surface is clearly the smoothest with no apparent surface features.

Fig. 5.2 shows the S_q vs T_a graphs for the coated paper samples and reference substrates calculated from the topographical images. The data calculated for the copy paper is not included because the values were well beyond the y-scale of Fig. 5.2 (from 299 nm up to 1156 nm). The samples with a pigment coating (Kaolin, PCC and Lumiart) are considerably rougher at short wavelength values compared to the other samples. The maximal image size of 100 μm × 100 μm obtained with the AFM is not quite large enough to show whether the curves are about to reach a saturation value (length scale-independent roughness). Such saturation was observed for the PET substrate and the polystyrene 96-well plate, whereas a considerable increase in the S_q value at longer length scale values was observed for the Latex 1 and 2 samples.

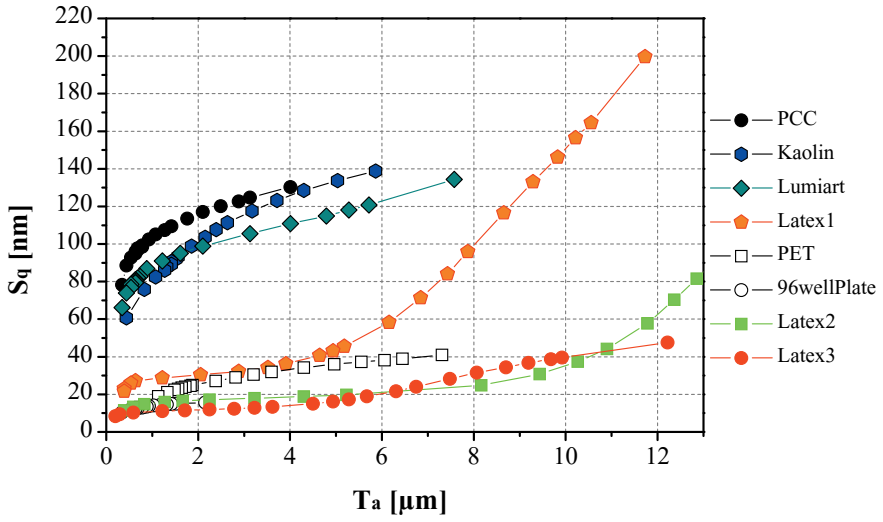

Fig. 5.2. S_q vs. T_a curves calculated from large scale AFM topographical images (100 µm × 100 µm) of coated papers and reference substrates.

The curves for Latex 1 and Latex 2 appear to show an intersection point (around correlation lengt values T_a = 5.5 µm and T_a = 9 µm, respectively). The S_q value at the intersection point (denoted as $\sigma_{sl,\ max}$ in S14) has been considered as a good approximation for the maximum roughness of the short length scale features and has been shown to correlate linearly with the resistance of printed wires, i.e. the smaller the $\sigma_{sl,\ max}$ value, the smaller the resistance.[S9] The macro-roughness at the long length scale values for the Latex 1 and 2 samples is most probably arising from the roughness of the basepaper. This is because the S_q vs T_a curves calculated for the Latex 2 and 3 samples with the same coating on different basepapers are rather similar at the short T_a values, but at longer length scales the S_q for the Latex 2 sample increases much more rapidly compared to the Latex 3 sample.

The optical micrographs (Fig. 5.3.) reveal the same thing, i.e. the Latex 3 sample appears really smooth whereas Latex 2 appears to have waviness in the structure.

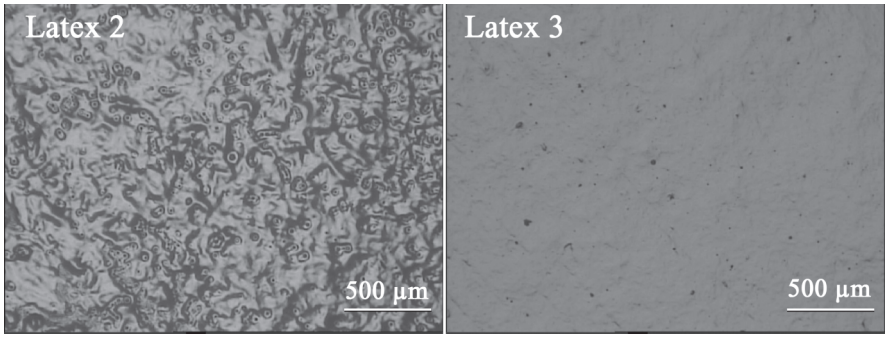

Fig. 5.3. Optical migrographs of Latex 2 and Latex 3 samples.

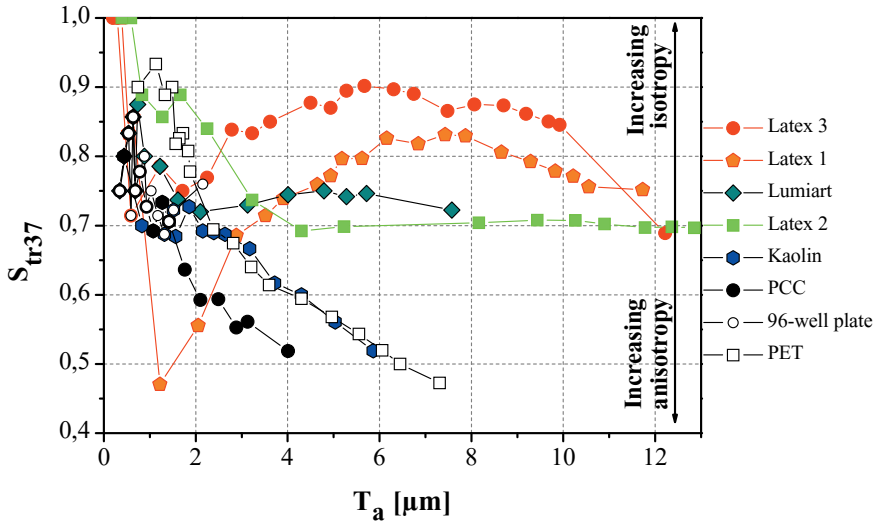

Fig. 5.4 S_{tr37} vs T_a curves calculated from large scale AFM topographical images (100 µm × 100 µm).

Fig. 5.4 shows the S_{tr37} vs T_a graph (calculated from the 100 µm ×100 µm topographical images). The Lumiart, Latex 2 and Latex 3 samples remain commendably close or above the S_{tr37} level of 0.7 meaning that the degree of isotropy is high on a broad range of correlation length scale values.[279] On the other hand, the laboratory scale pigment coated PCC and Kaolin samples that were calendered with a higher nip

pressure than the Latex-based coatings contain stripes from the calendering process and therefore have rather low S_{tr37} values and can be considered to be anisotropic. The steps formed on the calendering process are not very well defined or sharp, but at some locations are however relatively high, suggesting that they might cause a pinning of an advancing ink-surface contact line that has been shown to be considerable for steps 60 nm[280] in height. Fig. 5.5 shows an example of the influence of calendering on the S_q and S_{tr37} of a pigment coated sample (MLCC) fabricated by a curtain coating process.[S12,257] The first calendering significantly lowered the S_q roughness, especially at the longer correlation length values (Fig. 5.5.a). The second calendering further lowered the roughness, and the third calendering resulted in nearly a constant S_q value at the larger T_a values. Fig. 5.5b shows that the 0-2 times calendered samples can be considered to be isotropic at all length scales whereas the 3 times calendered substrate shows anisotropy at the longer length scale values. However, at small length scales roughness seems to be independent on the calendering because the S_{tr37} values remain high in all cases.

According to *ab initio* calculations the electrical conductivity of thin copper films was dramatically reduced already by atomic clusters, 1-3 atoms high.[281] As the smoothest and best conducting films are expected to form on flat substrates, solely from the roughness point of view e.g. the calandered substrates are expected to yield better conductivities than the uncalendered. Indeed, the resistance of printed wires and the line raggedness has been shown to decrease as a function of the calendering times of the MLCC paper substrate.[257] The same trend was observed with various other coated papers.[S14]

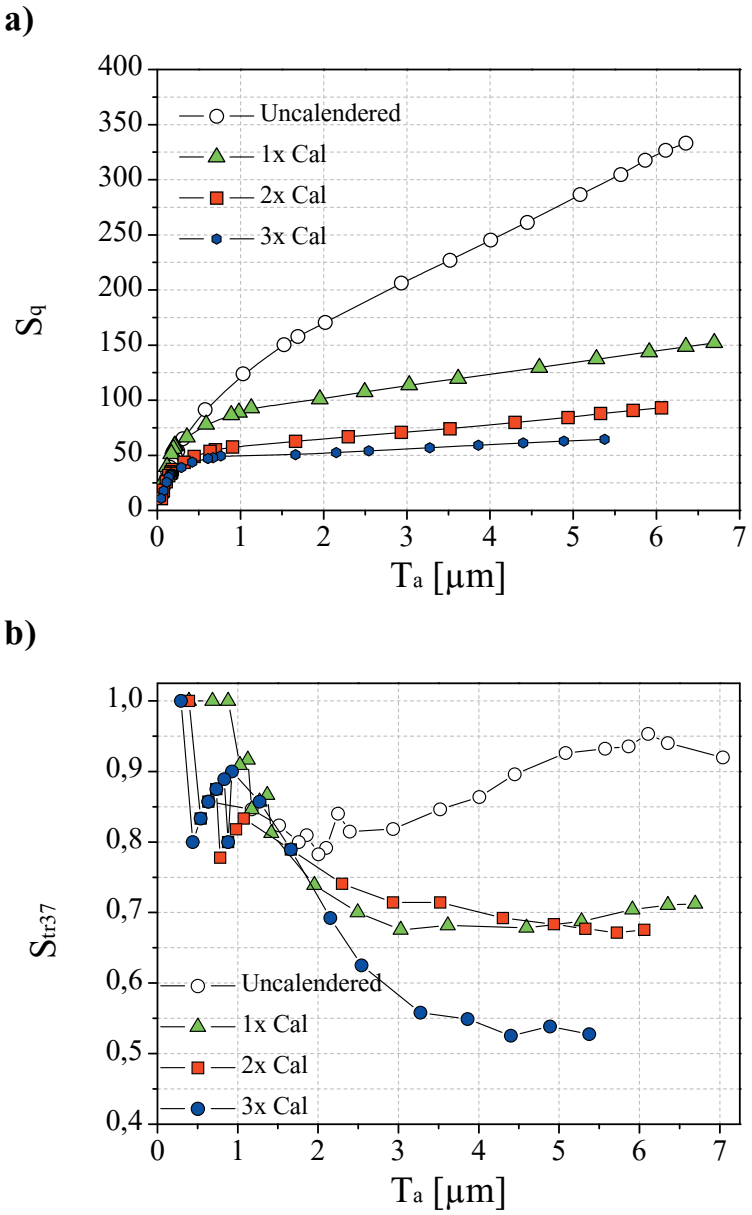

Fig. 5.5. Effect of calendering on the a) S_q roughness and b) S_{tr37} isotropy of a curtain coated paper (MLCC). The S_q vs T_a curves are compiled from 5 µm × 5 µm, 20 µm × 20 µm and 100 µm × 100 µm topographs and S_{tr37} vs T_a curves from 100 µm × 100 µm topographs.

5.2. Characterization of the print quality

5.2.1. Inkjet-printed silver and gold dots

An illustrative way to study the nanoscale effects of substrate roughness, porosity and chemistry on ink-surface interaction is to print individual dots and study their spreading and appearance (Fig. 5.6. and Fig. 5.7.).[282,S6] This enables also the estimation of a drop spacing value needed for achieving a thin but continuous ink film with the given fluid. Such critical drop spacing value is considerably different when printing e.g. a silver ink for example on a mica or a PET substrate with quite different surface properties.

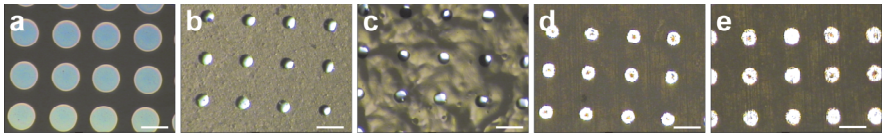

Fig. 5.6. Optical micrographs of printed Ag dots (wt. 40%, DS 150 µm) on different samples: a) Mica, b) PET, c) Latex 2, d) PCC and e) UVC treated PCC sample. The scale bar is 100 µm.

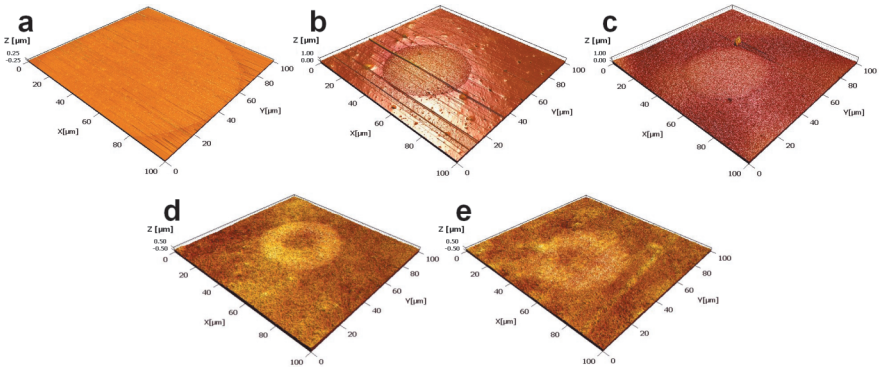

Fig. 5.7. AFM images of inkjet-printed Ag dots (wt.% 40) on a) Mica (Ag dot diameter, d = 110 µm), b) PET (d = 48.6 ± 0.4 µm), c) Latex 2 (d = 43.0 ± 1.0 µm), d) PCC (d = 51.7 ± 3.9 µm) and e) UVC treated PCC (d = 57.5 ± 3.6 µm).

On the atomically flat mica substrate with a high surface energy the printed dots are perfectly spherical and have a large diameter (Fig. 5.6.a and Fig. 5.7.a). On the contrary, the dots are much smaller on PET (Fig. 5.6.b and Fig. 5.7.b) and Latex 2 (Fig. 5.6.c and Fig. 5.7.c) representing samples with clearly lower a surface energy. By looking at the dots on the PCC coated samples (Fig. 5.6.d and 5.6.e) it can be concluded that the influence of the calendering lines on the dot shape doesn't seem to be large. However, in several dots some indication of a pinned contact line can be observed.

A UVC treatment of pigment coated samples has been shown to enhance wetting by making the substrates more polar without affecting the surface topography.[S6] The AFM topographical images (Fig. 5.7.d and 5.7.e.) reveal that in addition to the larger spreading of the ink on the UVC-treated sample the coffee ring formation is also slightly less pronounced. The dots were printed at once onto all the substrates. The form of the individual silver ink dots on Latex 2 sample was comparable to those on a PET film and more homogeneous than on the pigment coated papers where coffee ring formation was observed especially on the untreated PCC sample.

In case of the gold ink, the AFM topographical and phase images of individual dots on Latex 2 (Fig. 5.8.a-b) and Kaolin substrates (Fig. 5.8.c-f), reveal the more uniform ink coverage on the Kaolin sample. Considering that the diameters of the dots are of the same order (Fig. 5.8), one reason for the worse print quality on the Latex 2 sample might be the influence of the organic solvent on the structure of the Latex 2 coating as xylene dissolves latex and leads in a more irregular film (Fig. 5.9.).

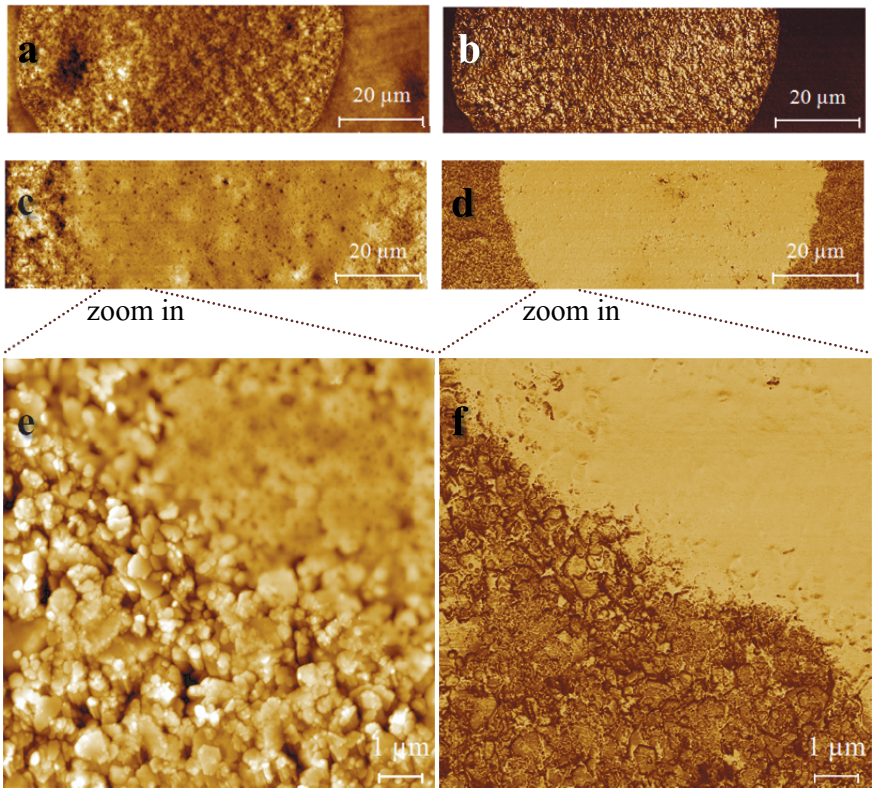

Fig. 5.8. AFM topographical (a, c, e) and phase (b, d, f) images of inkjet-printed Au dot on Latex 2 (a, b) and Kaolin (c-f) substrates (Figure modified from **Paper III**).

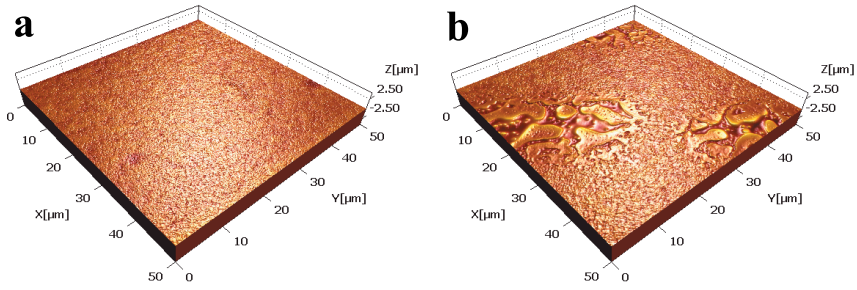

Fig. 5.9. AFM image of Latex 2 coating a) before and b) after exposure to xylene.

5.2.2. *Inkjet-printed silver and gold electrodes and IR sintering*

The inkjet-printed electrodes were made conducting by an IR treatment that vaporizes the solvent and burns away the organic material/stabilizing thiol layer surrounding the nanoparticles. The IR sintering process was efficient enough for melting the small AuNPs thus causing a phase transition from amorphous gold to crystalline gold (Fig. 5.10) indicated by the clear increase of the diffraction peak intensities (111) and (200) after IR-sintering. The required sintering time for the gold electrodes was approximately 5–15 s. The sintering resulted in a colour change from blackish to golden yellow. For the silver electrodes, the rather similar sintering kinetics on the Latex 2 and Kaolin-coated substrates is demonstrated in Fig. 5.11.

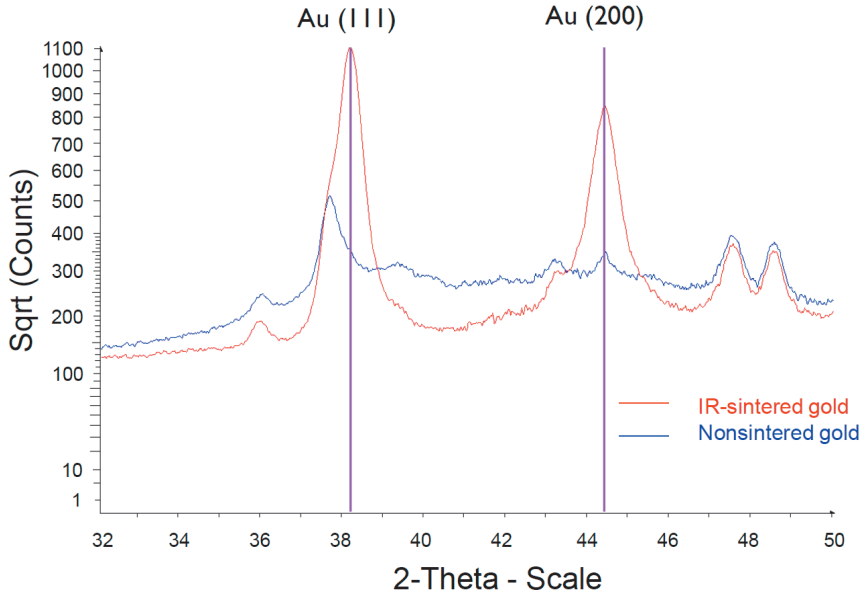

Fig. 5.10 Characterization of the gold electrodes by x-ray diffraction (XRD). The clear increase of the intensities of the diffraction peaks (111) and (200) as a result of IR-sintering indicates a phase transition from amorphous gold to crystalline gold. The diffraction patterns were collected with a Bruker-AXS D8 Discovery equipped with a HI-STAR 2D-detector.[283]

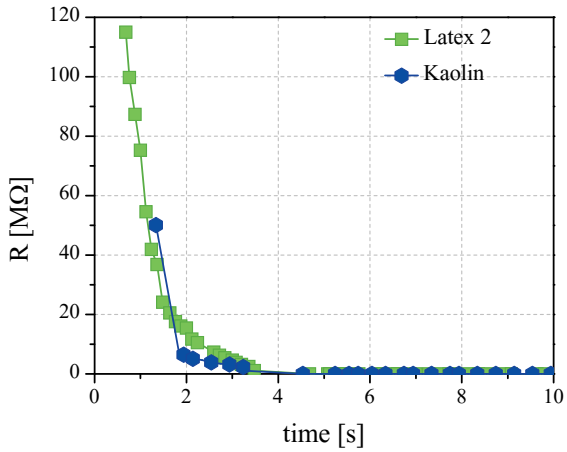

Fig. 5.11. The resistance of the inkjet-printed silver lines as a function of IR-sintering time on two different paper substrates.

Fig. 5.12a and Fig. 5.12b show digital photographs of IR sintered inkjet-printed interdigitated silver and gold electrodes on Kaolin coated paper. Fig. 5.12c-e show the test patterns that were used for resistance and resistivity measurements. Table 4 shows the line widths and resistance values obtained for the silver test patterns using different DS values for two different substrates. On the smoother $MLCC_{3x}$ substrate a clearly lower ink amount was required for achieving well conducting lines. The structures printed with DS 20 µm contained lines that were connected to each other also from the middle (Fig.5.12c) indicating a higher risk for short circuit. Small distances between the interdigitated electrodes are used e.g. in gas sensors[S12,S13,S17,S18] and between the source and drain electrodes in transistors[S14]. Also the edges were not as straight and precise (Fig.5.12c) when compared to the structures printed with larger DS values (Fig.5.12d). Therefore the printed silver electrodes with a small gap in **Paper IV**, were printed using a DS value of 25 µm. The conductivity of larger areas was not as sensitive to small local defects as the thin lines. However, when the inkjet-printed silver electrodes in **Paper V** were used to form the base for the quasi reference electrodes, the critical issue was the high enough thickness of the electrodes, since

part of the silver was consumed when the Ag/AgCl quasi reference electrode was fabricated by electrolysis. Therefore a DS value of 20 µm was used.

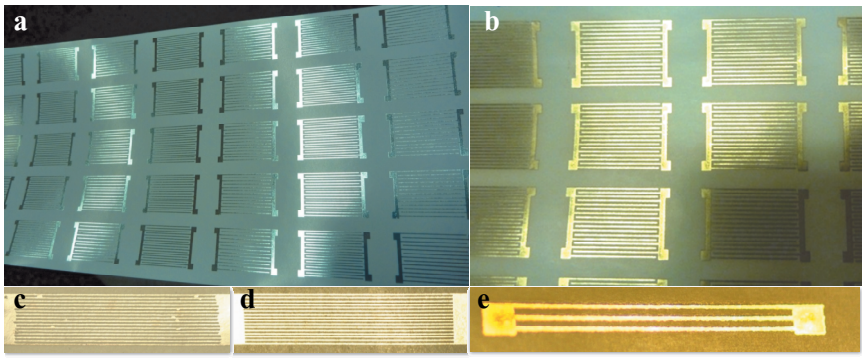

Fig. 5.12. Digital photographs of inkjet-printed interdigitated a) silver and b) gold electrodes and test patterns printed with c) silver, DS 20 µm, d) silver, DS 30 µm and e) gold, DS 30 µm.

Table 4. The effect of DS on line width and resistance of a test pattern printed with AgNP ink (wt.40%) on Kaolin coated paper and $MLCC_{3x}$ paper.

Substrate	DS [µm]	Line width [µm]	Resistance [Ω]
Kaolin	40	55 ± 5	OVLD
	30	61 ± 5	2360000 ± 2130000
	25	68 ± 6	52 ± 22
	20	78 ± 6	10 ± 3
$MLCC_{3x}$	40	51 ± 3	19.6 ± 3
	30	57 ± 4	11.5 ± 2.3
	25	63 ± 5	7.9 ± 0.5

Since the inkjet-printed gold electrodes were also used as substrates for self-assembly of thiol films, it was critical that the electrode surface was as smooth as possible. The effect of DS and the sintering method on the roughness of the gold films was studied by characterizing the prints by AFM and by calculating the S_q vs T curves (Fig. 5.13). The printed gold layer had a smaller roughness at all length scales compared to the

unprinted substrate. The unsintered (dried in air) gold print was clearly the smoothest. Rapid evaporation of xylene, burning of the thiols and annealing of the gold particles during IR-treatment increased the roughness of the films. Although conducting films were obtained even with a DS of 45 µm the roughness of the thin film was nearly as high as that of the unprinted paper substrate. Films that were made conducting by annealing in an oven were slightly smoother than the IR-sintered films, but the process was much slower and lead to brownish paper substrates. Therefore IR-sintering was preferred. DS 30 µm was found to provide an optimal amount of ink for obtaining a thick enough layer (>200 nm) that covers the pigment particles forming a smooth film.

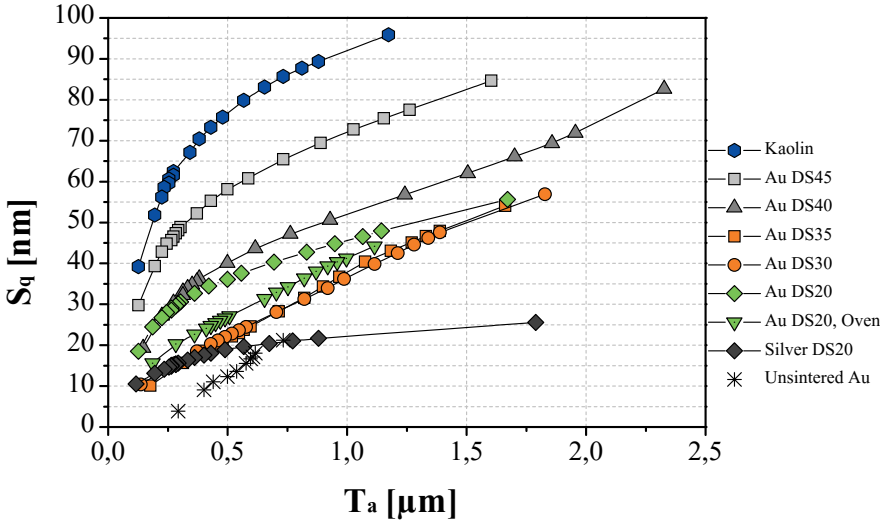

Fig. 5.13. S_q vs T_a curves for the unprinted Kaolin sample and various gold and silver prints (calculated from 20 µm × 20 µm topographs).

Fig. 5.14 shows AFM topographical images (isometric view) of the Kaolin substrate and the gold film (DS 30 µm) scanned at the same spot before and after IR treatment. Also by visual observation, the films printed with DS 30 µm appeared to be the smoothest. The cracking tendency was observed to increase when the drop spacing was decreased i.e. when the thickness of the film increased (**Paper III**). The divergencies in the thermal expansion and thermal conductivity between

the gold film and the substrate are reasons for the generated defects during cooling of the sintered films.[284]

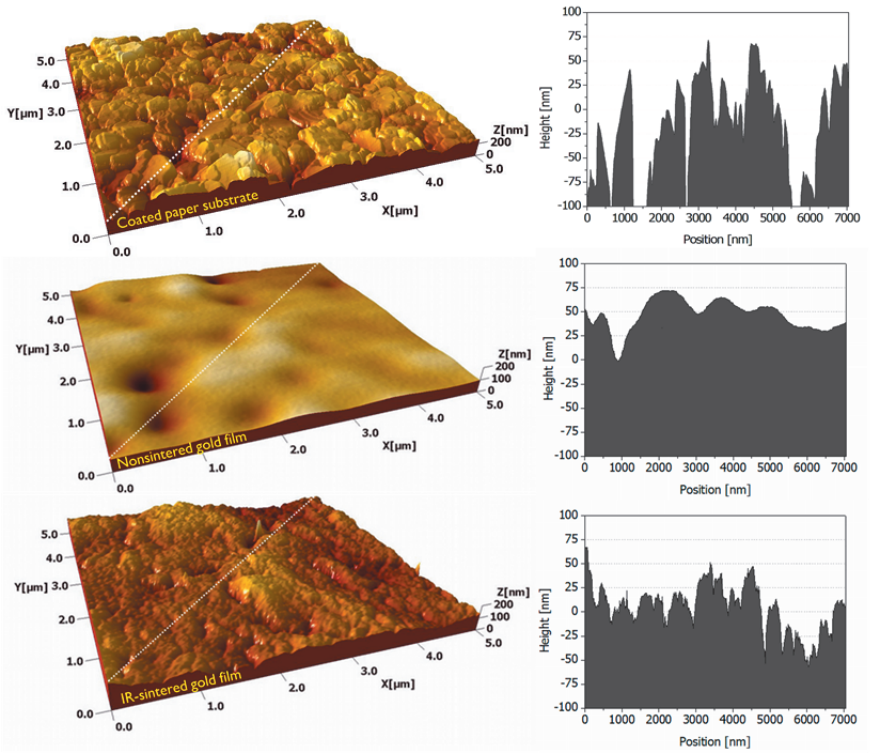

Fig. 5.14. AFM topographical images and corresponding line profiles of the Kaolin coated paper substrate, the nonsintered gold film and the IR-sintered gold film (Image modified from Supporting Information, **Paper III**).

The resistivity (ρ) was obtained by measuring the thickness (d), line width (W) (multiplied with the number of line(s) in the test pattern) and the length, (L) of the fingers and by inserting the values together with the resistance into equation 4.3. The obtained resistivity for silver was 2.6×10^{-7} Ωm and for gold 1.6×10^{-7} Ωm (**Paper III**). The resistivity values are based on the thickness of the metal films measured by AFM.

The resistivity of 1.6×10^{-7} Ωm was comparable to the previously reported values for gold tracks on a glass substrate[285]. However, the bulk

resistivity of silver and gold at 20°C is somewhat lower, 1.59×10^{-8} Ωm[286] and 2.44×10^{-8} Ωm[287], respectively.

Assuming that the printing parameters were optimized, the main reason for the lower conductivity obtained for the printed structures compared to bulk conductivity has been considered to be the porosity, holes and cavities of the film.[284] Other factors contributing to the conductivity are the properties of the substrate such as permeability of the coating structure and roughness.[288] Also the amount of organic insulating material remaining on the electrode surface after sintering is significant according to XPS results (Table 1 in **Paper III**).

The melting temperature of both silver[289,290] and gold[291] nanoparticles is dependent on the surface-to-volume ratio and decreasing with decreasing particle size, as expected.

Because the size of the printed silver particles (30–50 nm) is much larger than the size of the gold particles (2–5 nm) and therefore the melting point higher, the gold nanoparticles are annealing more easily during the sintering process and are expected to form a less porous film thus also having better barrier properties against liquid penetration. AFM topographical measurements carried out for the unsintered and sintered films confirm that the printed silver particles appear to remain unchanged whereas the gold nanoparticles form approximately 30 nm sized crystalline nanoclusters[292] that appear being melted together. The fact that the Ag nanoparticles pack nicely on the surface and the IR sintering has no adverse effect on the topography of the film, the roughness of the silver film is lower than that of the IR sintered gold film (Fig. 5.13). On the other hand, the porosity of the Ag electrodes is higher than that of the gold electrodes which may explain the better conductivity of the gold electrodes. Another reason that contributes to the better barrier properties of the gold film is the fact that the hydrophobic AuNPs are able to penetrate more easily into the top coating layer. This is especially well seen when the AuNPs are printed on the PCC coated paper (Fig. 5.15.a,b) which is more porous than the Kaolin coated paper. When electrodes such as those shown in Fig.

5.15.a are IR sintered the purple areas remain purple and unconducting [S16] and the lighter areas become golden indicating that the purple colour corresponds to gold nanoparticles that for the most part have penetrated inside the top coating layer. Fig. 5.15.b shows a cross section image of the IR sintered inkjet-printed gold electrode on a PCC-coated paper substrate.

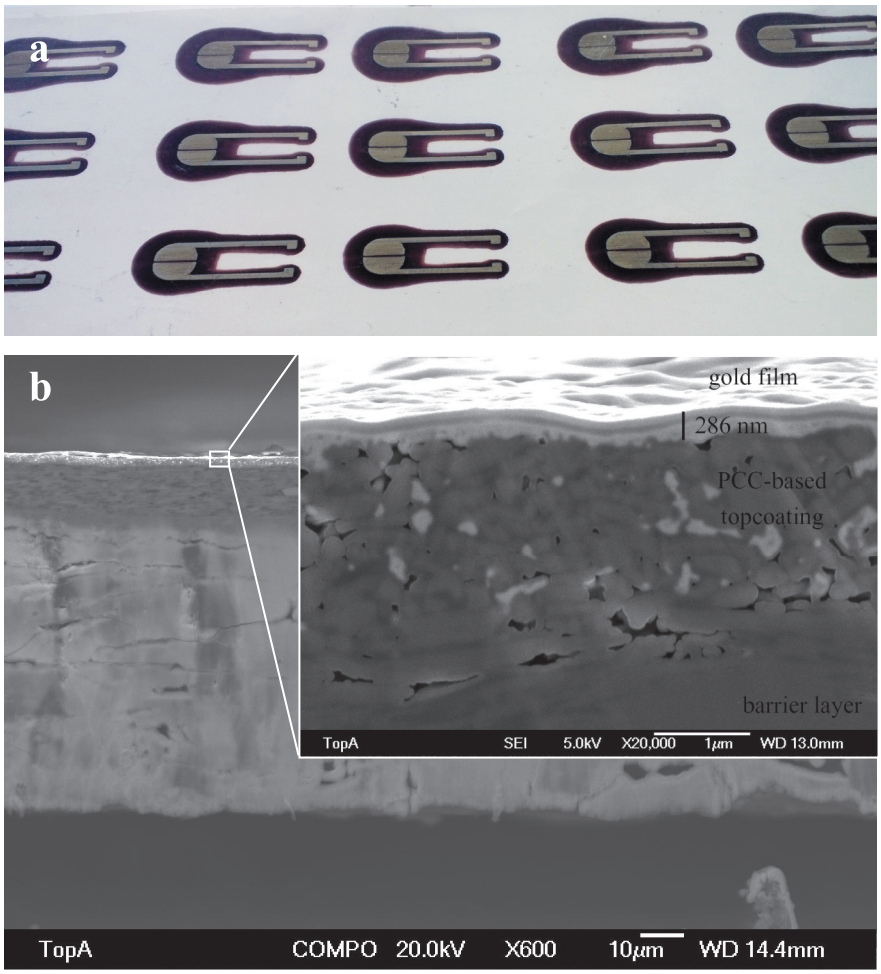

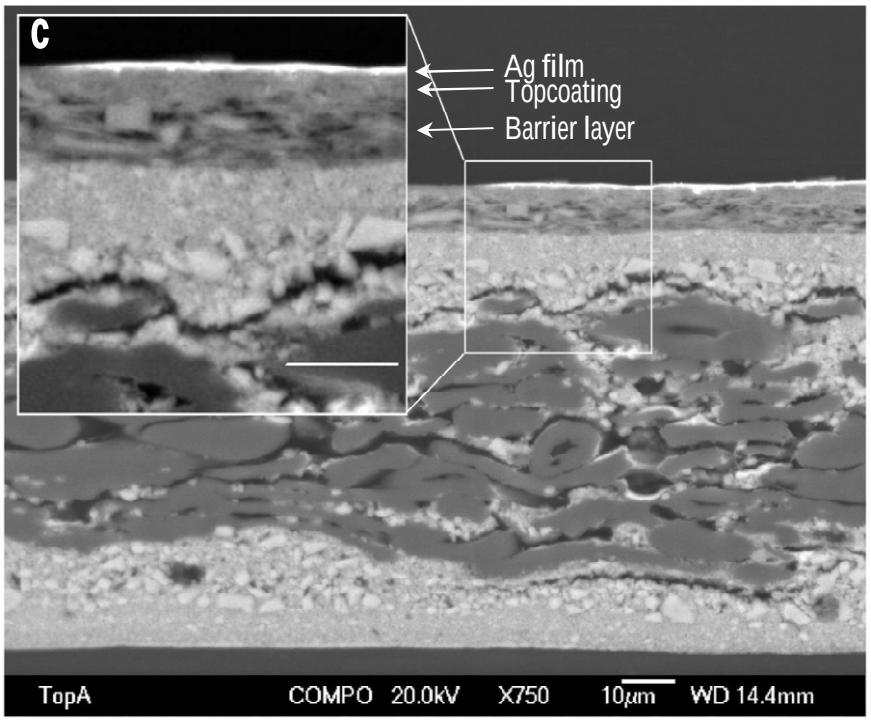

Fig. 5.15. a) A digital photograph of unsintered gold prints showing the penetration of the AuNPs (dark purple) inside the PCC-based topcoating layer. The intended printed area turns lighter in colour after a long drying period. b) A SEM image of the cross section of a gold print on PCC. c) A SEM image of the cross section of an Ag print on a curtain coated paper. The samples for the cross-section analysis were cut using a broad ion beam (BIB) technique at Top Analytica Oy Ab, Turku.[293]

The print quality and conductivity obtained with the AuNP ink is especially sensitive to the substrate properties. No conducting gold tracks were obtained on the Latex 2 sample although the printed gold remained on top of the surface and changed colour in a normal way during sintering. Small cracks and discontinuities in the printed gold films lead to resistance being high and beyond the measurable range (OVLD).

Neither was conducting gold patterns obtained on commercial paper substrates due to the penetration of the gold nanoparticles into the

coating structure. The print quality of gold or more specifically the adhesion was not optimal on glass either. PET on the other hand could not be used due to its poor thermal stability. For the paper substrates with a thin and porous topcoating layer of Kaolin or PCC and a barrier layer underneath the print quality and adhesion was good. The good coverage of the print layer is obviously a result of the small nanoparticles being able to slightly penetrate into the top coating layer (see inset of Fig. 5.15.b, left and right edge). Furthermore, the printed line was mechanically durable as a result of the sintering process. The adhesion of the printed gold layer on the pigment coated papers was strong enough for withstanding bending and twisting without loss of conductivity (Supplementary video, **Paper III**).

In contrast to the printing tests performed with the gold ink, it was observed that the permeability of the coating structure was not as critical for the silver ink. Conductive tracks were obtained since the silver particles were relatively large and remained on top of the coating structure (Fig. 5.15.c), even on papers without a barrier layer. However, it is beneficial if the solvents used in the silver ink can penetrate into the coating structure of the paper leaving less organic material on the surface to be removed during IR sintering. For example when the same test pattern was printed (wt. 20%, DS 20 μm) on a commercial double sided coated paper substrate with and without a PDMS barrier layer on the backside, the resistance values obtained with the PDMS-free substrate (30 Ω) were considerably lower than those with PDMS on the backside (130 Ω). The influence of the backside PDMS coating on the spreading/absorption of the inkjet-printed silver droplets is well seen when a higher DS value is used (Fig. 5.16.). The droplets remained separated in the areas having the backside coated with PDMS (Fig. 5.16.a). A more continuous film was obtained on that part of the paper where no PDMS was coated on the backside (Fig. 5.16.b). Water contact angle of the paper substrate with a PDMS backside stabilized to a value of approximately 80° being 10-20 degrees higher than that of the PDMS-free sample. This demonstrates that PDMS had penetrated

throught a double sided pigment coated paper that had no special barrier layer.

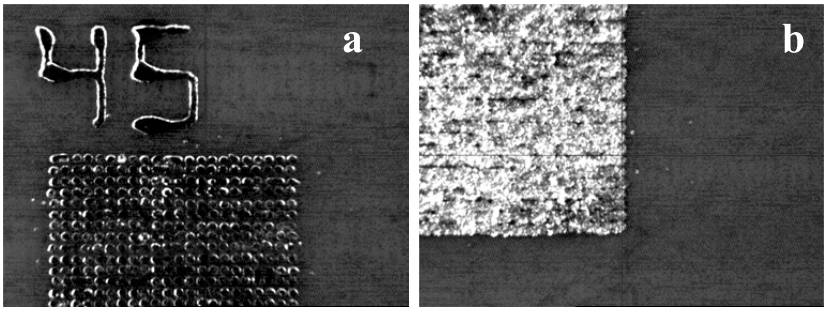

Fig. 5.16. Inkjet-printed silver pattern (DS 45 µm, 1 mm^2) on a commercial paper a) with and b) without a flexographically printed back side PDMS barrier film (3 layers).

5.2.3. Evaporated ultra thin gold electrodes on Latex 2

A vacuum evaporation technique was tested for the fabrication of ultra thin gold electrodes (<10 nm) on the Latex-based substrates. Fig. 5.17 shows topography and DMT[267] modulus images of the border of the evaporated gold film on Latex 2 substrate captured with peak force tapping mode AFM[268]. The left sides of the images correspond to the evaporated gold film. The border of the evaporated gold film is clearly seen in the images, especially on the DMT modulus image. Small gold grains that are typical for an evaporated gold film[294] are better discerned in the left-hand smaller scale image and they appear to cover both the higher and lower parts of the Latex 2 surface. The contrast in Fig. 5.17.b changes totally in the middle of the image and affirms that a continuous gold film is formed on the Latex 2 coating as can be expected also from the low resistivity value ($\rho = 8.15 \times 10^{-8}$ Ω m obtained for a gold track using the nominal thickness of 2×10^{-8} m, width of 1.54×10^{-3} m, length of 4.84×10^{-3} m and resistance of 12.8 Ω).

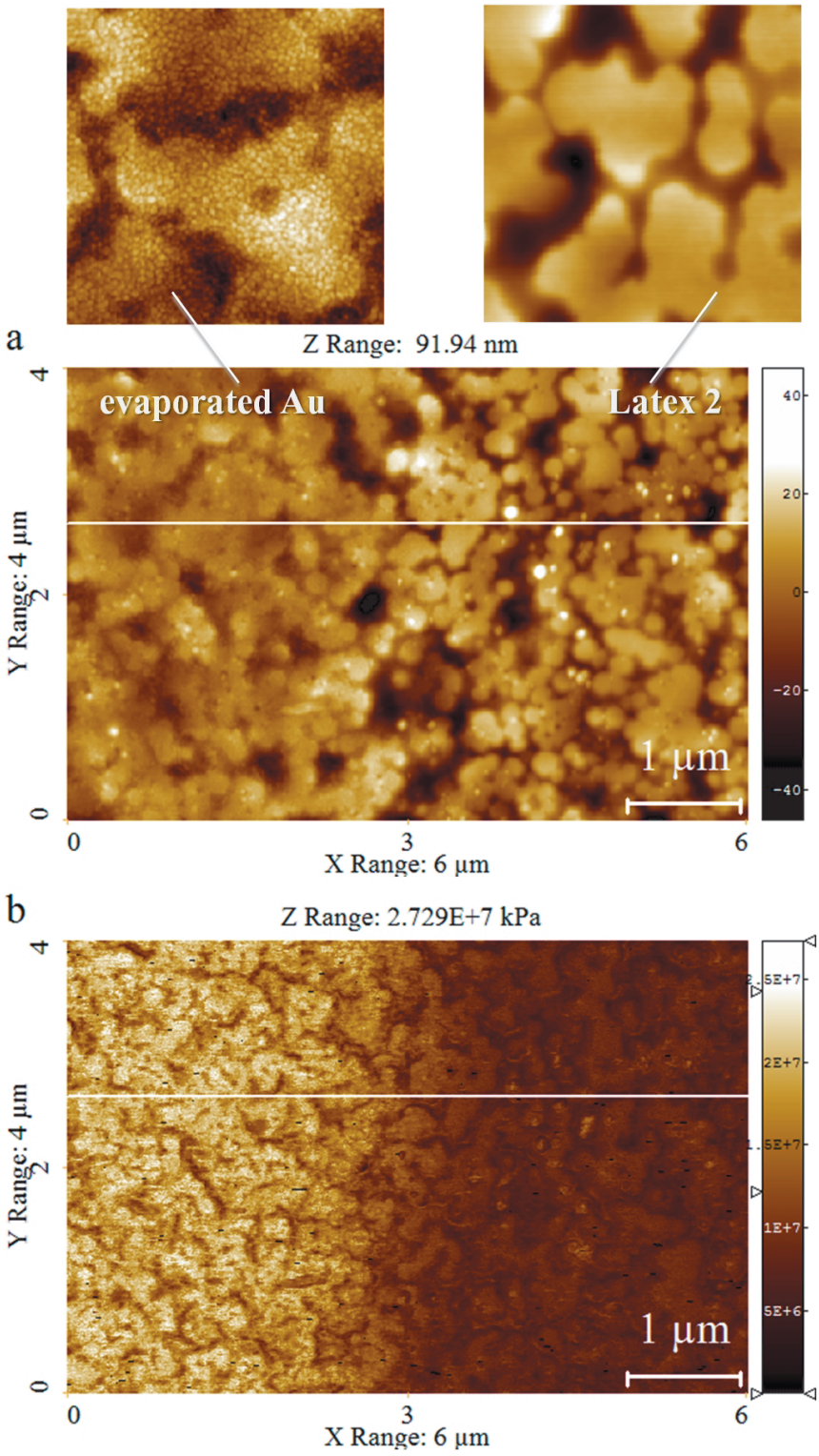
a
Z Range: 91.94 nm
evaporated Au
Latex 2
40
20
0
-20
-40
Y Range: 4 µm
4
2
0
1 µm
0
3
6
X Range: 6 µm
b
Z Range: 2.729E+7 kPa
2.5E+7
2E+7
1.5E+7
1E+7
5E+6
Y Range: 4 µm
4
2
0
1 µm
0
3
6
X Range: 6 µm

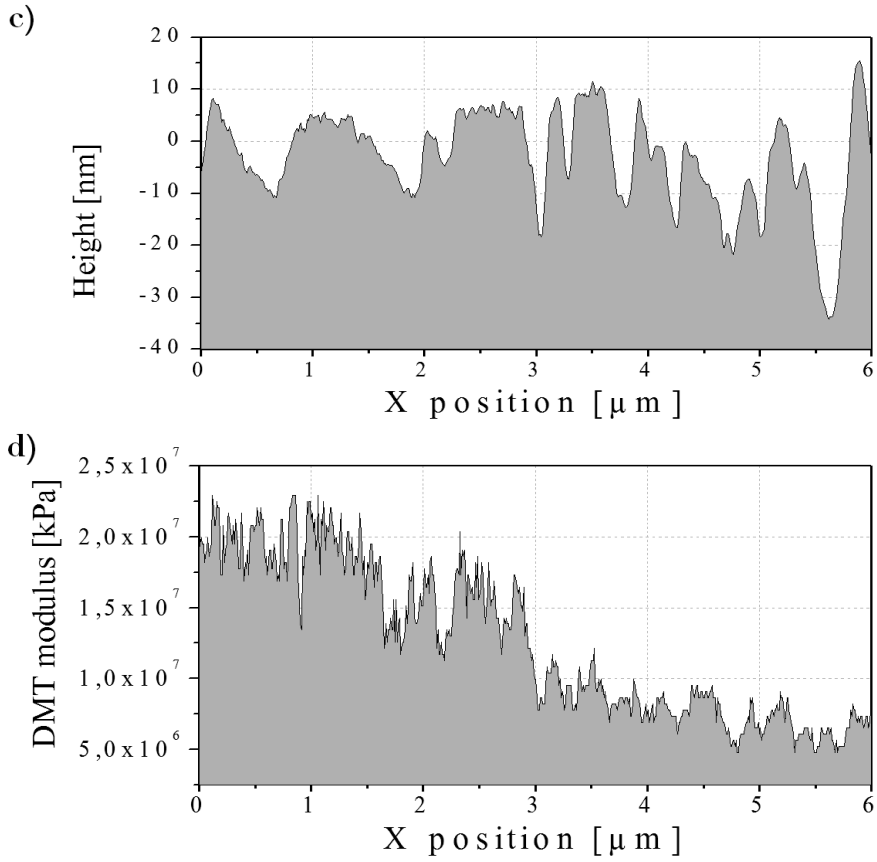

Fig. 5.17. a) AFM topographical and b) DMT modulus images of the border of the evaporated gold film on Latex 2 sample captured by the peak force tapping mode. The size of the high-resolution images are 1 µm × 1 µm. c) height and d) DMT modulus profiles drawn along the horizontal white lines in a) and b), respectively.

A good adhesion of the gold film is vital considering the sensing applications that are often carried out in liquid environment. Adhesion of evaporated gold has been an issue on e.g. SU-8, glass and silica substrates and studies have been carried out to improve the adhesion.[295] No adhesion problems were observed with the Latex 2 substrate.

5.3. Verification of the printed platforms

5.3.1. Planar printed microtiter plate

Fig. 5.18 shows a schematic illustration of the planar reaction arrays printed on a coated paper substrate with a barrier against liquid and on a highly permeable paper substrate. In the former case the analytes or samples in the reaction areas remain separated partly by the PDMS and partly by the barrier layer, and in the latter case solely by the hydrophobic PDMS. By the choice of the paper substrate and the easily changeable print pattern different platforms can be prepared for various purposes, e.g. for 2D or 3D bacterial and cell culture.[S19,296]

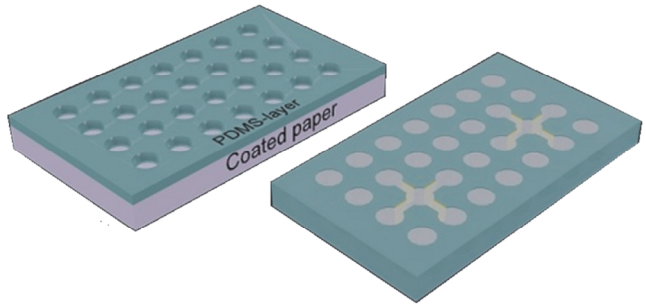

Fig. 5.18. Schematic images of the reaction array platforms (**Paper I**).

The commercial PDMS-based material has been optimized for coating paper and other substrates and has a suitably short curing time (10 s, 150°C). The platforms were fabricated in a simple and fast way by a roll-to-roll process with only two process steps i.e. printing and curing with IR-lamps, as shown in **Paper I**. The solventless ink has an oily consistency and good flow properties that promotes its penetration into permeable substrates and guarantees a smooth film on coated paper with adequate barrier properties and absence of large pores such as on uncoated copy paper for instance. Furthermore the material is relatively inexpensive and does not exhibit any ecotoxicological problems.[259]

Example photographs of the printed PDMS ink on coated and uncoated substrate are shown in Fig. 5.19.

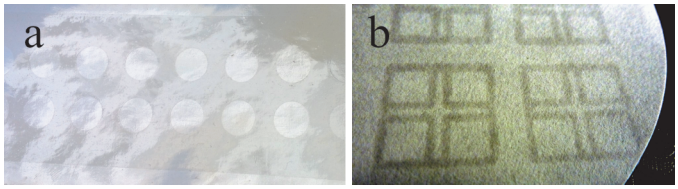

Fig. 5.19. Digital photographs of the PDMS prints a) flexographically printed on Latex 3 and b) inkjet printed on filter paper. The circular areas on the Latex 3 are the PDMS-free reaction areas and the darker and more translucent structures on the white filter paper against the dark background contain the printed ink.

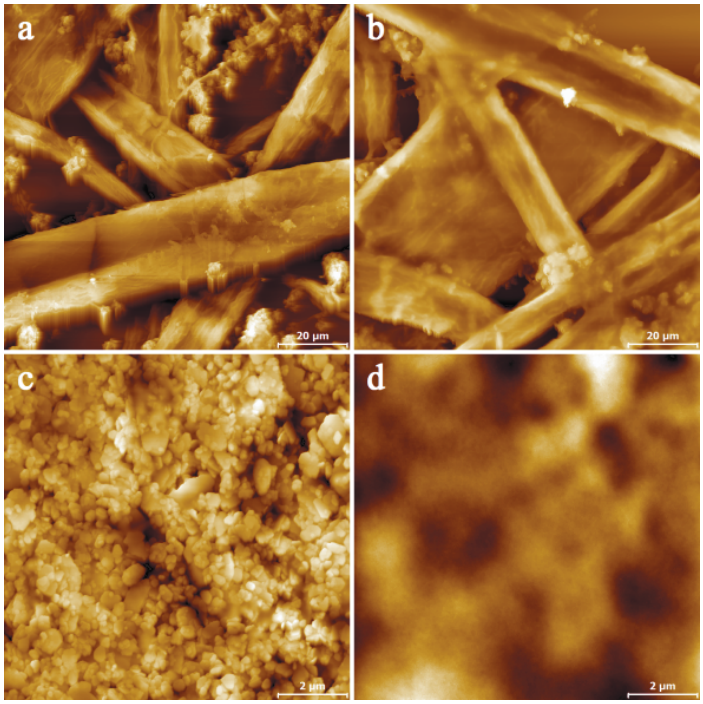

Fig. 5.20. Large scale (100 µm × 100 µm) AFM topographical images of a) unprinted copy paper and b) a PDMS film (3 flexographically printed layers) on copy paper. Respectively, the topographical image (10 µm × 10 µm) in c) represents a Kaolin coated paper (z-range 413 nm) on which a PDMS layer was flexographically printed (image d, z-range 82 nm) (Figure modified from **Paper I**).

The barrier properties of the substrates strongly influence the penetration and appearance of the PDMS ink film. The AFM topographical images of a copy paper and a copy paper with three flexographically printed PDMS layers appear rather similar, because the ink effectively absorbs into the substrate which has no barrier layer. The RMS roughness (S_q) value for the both surfaces was approximately 3 µm. In reality, the values are higer because the z-range limit was reached during the AFM measurements. In contrast, only 1 print layer of PDMS was enough to create a smooth film on a Kaolin-coated paper including a barrier layer underneath the top coating (Fig. 5.20.). The S_q value was 48.7 nm for the Kaolin-coated surface and 11.7 nm for the PDMS film.

The printed PDMS surface is strongly hydrophobic and non-absorptive. Contact angle measurements yielded values 141.6° ± 2.4° and 141.2° ± 2.0° for the frontside and backside of a PDMS-printed filter paper revealing that PDMS had penetrated throughout the thickness of the paper substrate. The patterned PDMS print thus enables the directing of analyte solutions into the predesigned, PDMS-free locations in a paper substrate (Fig. 5.21.) allowing e.g. microfluidic assays.

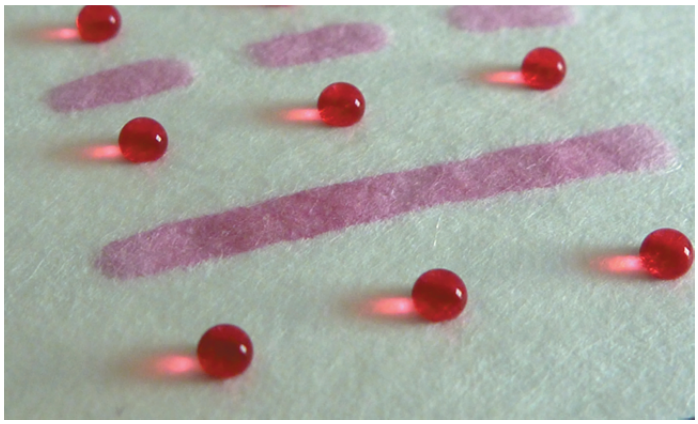

Fig. 5.21. A digital photograph of coloured water droplets applied on the PDMS-printed areas where they remain as droplets on the surface, while on the channel areas (free of PDMS) the liquid quickly absorps (**Paper III**).

On the other hand, if the backside of the pigment-coated paper (PCC) was coated with a PDMS film, the latex-based barrier layer prevented the penetration of the PDMS on the other side and the CA value for the top coating (front side) remained the same regardless if the backside was coated with PDMS or not. The contact angle of water on a PDMS film printed on coated paper and PET is approximately 110-114°. The theoretical maximum contact angle of water on a flat surface is approximately 120°.[297] Therefore it is logical that the smoother PDMS film on the coated paper has much lower a CA value compared to that on the much rougher filter paper.

5.3.2. Electrochemical platforms for electrochemical analyses

A schematic illustration and digital photographs of the electrochemical platforms with two (**Paper IV**) and three electrodes (**Paper V**) are shown in Fig 5.22. The planar three-electrode system consisted of an inkjet-printed gold working electrode (WE) and counter electrode (CE) and an inkjet-printed silver electrode, onto which an AgCl layer was deposited electrochemically resulting in an Ag/AgCl quasi-reference electrode (QRE). Both bare and functionalized gold electrodes were analyzed with several techniques in order to verify that the electrodes behave as expected, i.e. having a performance comparable with conventional or evaporated gold electrodes.

Thiolation is one of the simplest functionalization methods for gold electrodes. The quality of the thiol layer depends on the underlying electrode surface among other parameters, such as immersion time, concentration of the thiols, chain length, temperature and solvent. At regions where the topography of the substrate changes abruptly, the structure of the SAM might have defects, thus providing a tool for examining the quality of the printed electrodes.[189,298] It is important that a homogeneous thiol layer is obtained since thiolation is often the first step in the fabrication of e.g. immunosensors.[299,S16]

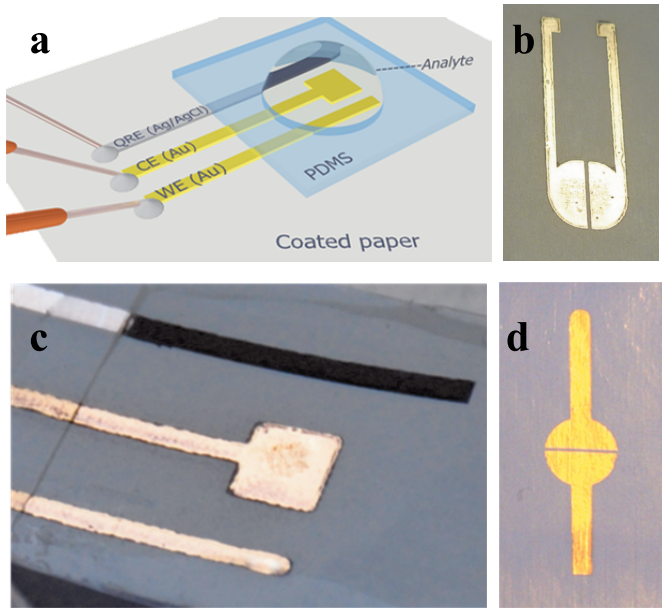

Fig. 5.22. a) A schematic illustration of the planar three electrode platform, b) a digital photograph of inkjet-printed gold electrodes on Kaolin coated paper, c) a digital photograph of the three electrode platform and d) a digital photograph of evaporated gold electrodes (nominal thickness 30 nm) on Latex 3.

The SP measurements revealed that thiolation of the plasma-cleaned inkjet-printed gold electrodes by using 1-octadecanethiol induced a +406 mV shift in contact potential difference. The corresponding value for the evaporated gold electrodes on a plastic substrate was nearly the same, +436 mV. The values are in good agreement with the magnitude of the shift, which according to the literature should be about 20 mV/CH_2 unit for an alkanethiol monolayer on gold.[300]

Impedance spectroscopy measurements provide a sensitive method for studying the quality of the thiol layer on the printed and evaporated electrodes.[301] Despite the highly varying capacitance values (C_{real}) obtained for the bare electrodes (Fig. 5.23.a), the capacitance values for the thiolated electrodes (Fig. 5.23.b), apart from one (AgNP+ODT), were nearly equal and saturated after a short stabilization time. The result shows that uniform thiol layers were formed on inkjet-printed

gold electrodes that could further be used for the fabrication of immunosensors.[S16]

The C_{real} versus frequency curve that was obtained for the thiolated silver electrodes printed on paper was unstable and considerably different from the other curves. Fig. 5.24 shows C_{real} vs frequency curves measured at different times after thiolation of the inkjet-printed silver electrodes. Shortly after thiolation the C_{real} value appears to be saturating, but then gradually starts to approach the curve that was obtained for the bare silver without a thiol layer. This indicates a poor SAM quality and the ability of the liquid to penetrate through the silver electrode all the way through the topcoating and inside it. Similar problematic behaviour was not observed for the nonporous PEN.

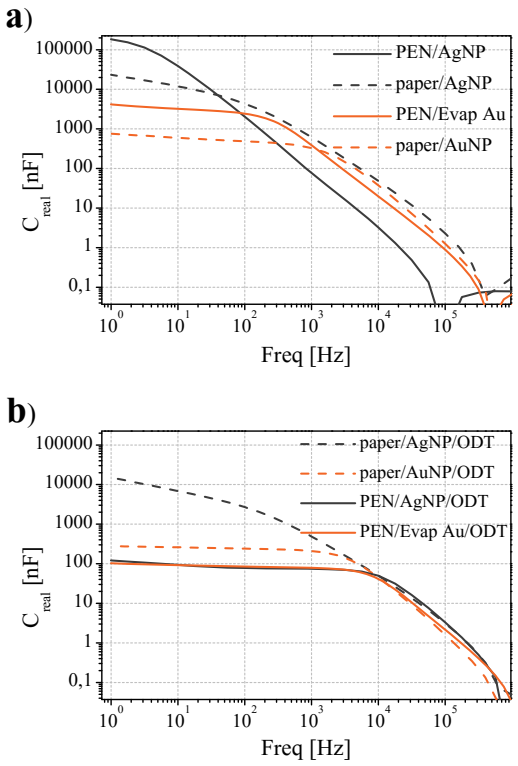

Fig. 5.23. Real capacitance (C_{real}) of the electrodes as a function of the frequency a) before and b) after thiolation (**Paper IV**).

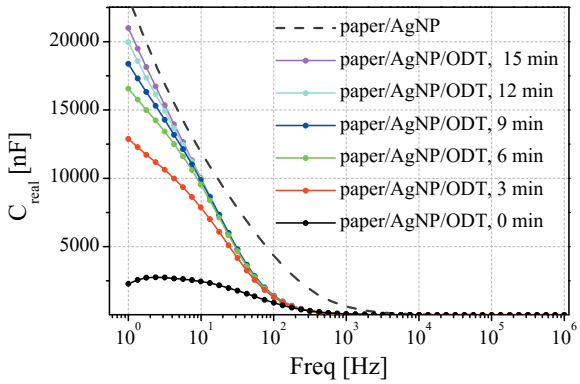

Fig. 5.24. C_{real} vs Freq curves measured 0-15 min after thiolation of the inkjet-printed silver electrodes on paper reveal the deterioration.

Cyclic voltammetry measurements were carried out to characterize the printed three-electrode platform on paper and to compare its performance to a conventional electrochemical cell. The shapes of the CVs recorded with the paper-based three electrode platform (Fig. 5.25.a) appear similar to the ones obtained with the commercial gold-disk electrodes (Fig. 5.25.b). The influence of the scan rate and thiolation of the WE on the peak currents for the paper-based platform is shown in Fig. 5.26. As predicted by the Randles-Sevcik equation (Eq.2.12), the peak currents increase as a function of the scan rate. The ODT-modified gold electrode showed lower peak values and larger separations as expected due to the hindered access of the redox couple on the electrode surface. The peak separation values obtained with the gold electrodes were comparable with previously reported highly polished gold discs and commercial screen-printed electrodes.[54,302,303] The ratio of the peak currents ($|I_{pa}/I_{pc}|$) obtained with the printed gold electrodes on paper (1.080 ± 0.044) was slightly higher than the one obtained for the conventional gold disk electrode (1.001 ± 0.025) but fairly close to the theoretical value, 1.

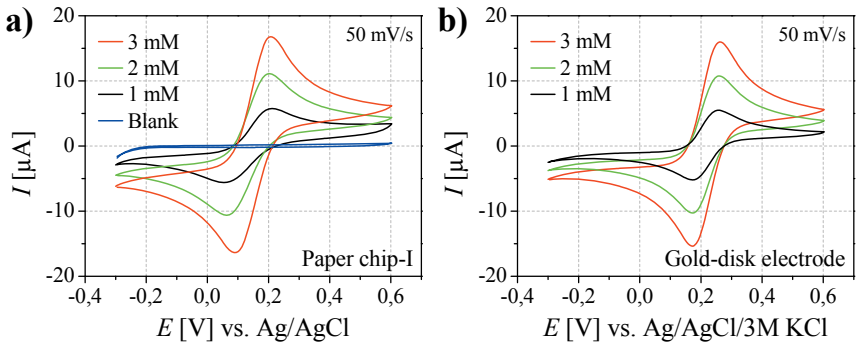

Fig. 5.25. Cyclic voltammograms of $K_3Fe(CN)_6/K_4Fe(CN)_6$ redox couple in 0.1 M KCl as a function of the analyte concentration measured with a) a paper-based platform and b) a conventional cell (**Paper V**).

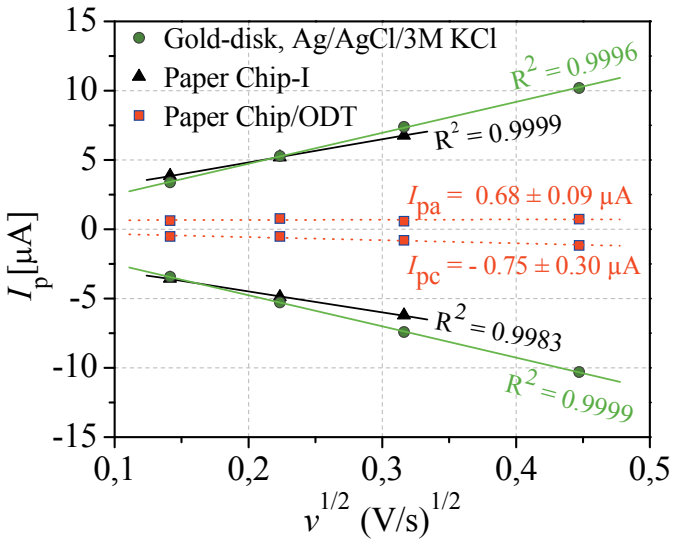

Fig. 5.26. The variation of anodic I_{pa} and cathodic I_{pc} peak currents as a function of the square root of the potential scan rate (**Paper V**).

The detailed mechanism of electropolymerization of conducting polymers remain still not fully understood.[304] Despite that, electropolymerization is a common way to functionalize electrodes and by that way broaden their application areas. Therefore the suitability of the printed electrode platform for electropolymerization was tested.

Polyaniline being an important conducting polymer was selected as the functional material. The growth of a PANI layer on the paper-based platform and on a commercial gold electrode is compared in Fig. 5.27. With both systems continuously increasing oxidation and reduction peak currents in the CVs were observed indicating that the polymer films were formed on the surfaces. The growth of the film and the redox reactions were also evident due to the electrochromic properties of PANI. During the forward scan the films oxidize i.e. the leucoemeraldine/emeraldine transition takes place and during the reverse scans reduction takes place. The film on the printed gold working electrode appeared green in the oxidized form and colourless in the reduced form.

Since the potential of the polyaniline film is known to be sensitive to pH, the suitability of the electropolymerized films as a solid-state pH-sensor was tested (Fig. 5.28). The obtained slope was fairly close to the theoretical value –59 mV per pH unit.

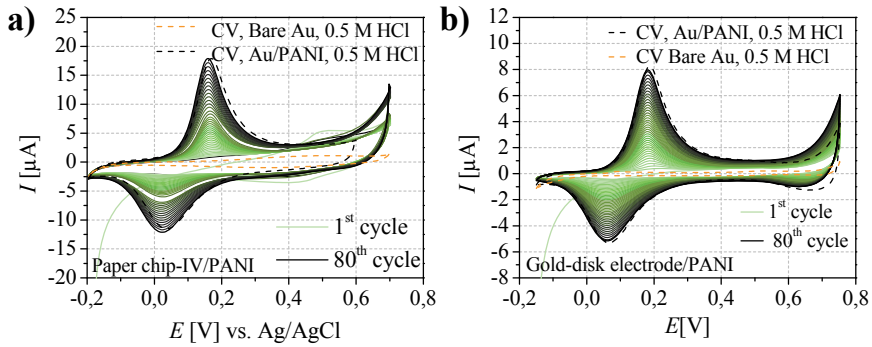

Fig. 5.27. An electropolymerization curve of PANI and the measured cyclic voltammograms in monomer-free 0.5 M HCl before and after the polymerization on the (a) paper chip-IV and (b) gold-disk electrode (**Paper V**).

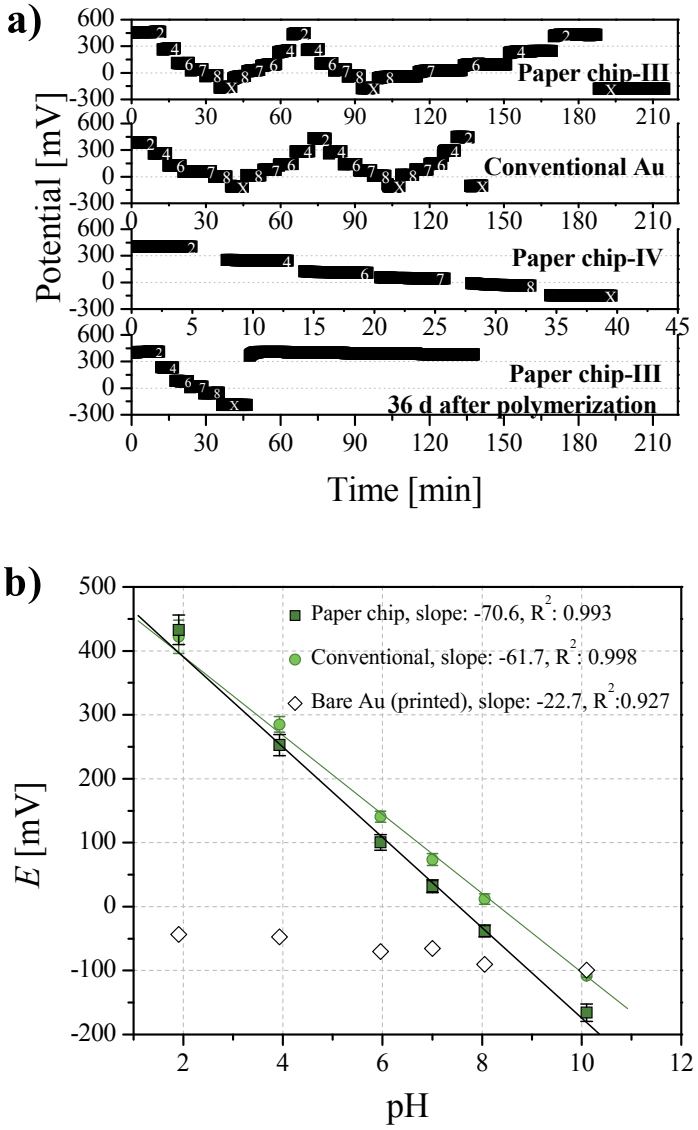

Fig. 5.28. a) Potential vs. time curves for the conventional Au-disk/PANI and paper-based Au/PANI electrode. The pH of the buffer solution is indicated by the numbers (2, 4, 6, 7, 8, X (=pH 10)) at the points that also correspond to the potential values measured after 5 min of the application of the subsequent buffer solution. b) Calibration curves obtained with modified conventional Au-disk/PANI, a paper-based Au/PANI electrode (average of 2 chips and 6 calibrations) and a bare paper/Au electrode (**Paper V**).

5.4. Applications and demonstrations

5.4.1. Biofilm formation and screening of anti-biofilm agents

Microtiter plates[180], and actual implant materials (e.g. Ti based materials [305,306]) are typically used as substrates in biofilm studies.[307,308,309] In **Paper II**, the possibility of using the planar paper-based platforms for biofilm formation was explored (Fig. 5.29.).

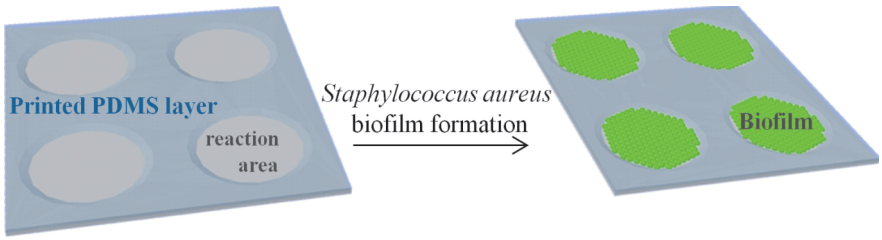

Fig. 5.29. A schematic illustration of the biofilm formation on the PDMS-free reaction areas on a paper substrate.

The adhesion of *S. aureus* on the printed PDMS film was very low, therefore the biofilm formation was concentrated on the unprinted reaction areas. The physicochemical properties of the different coated paper substrates were found to impact the biofilm formation. The coatings with relatively high polar surface energy component and S_{dr} (Kaolin and Latex 2) were the ones that were most susceptible for biofilm formation according to colony forming unit (CFU) calculations (Fig. 5.30.). The AFM topographical measurements also revealed that a dense biofilm formed on these substrates, whereas the biofilm on the other substrates was sparce or only partially covering the reaction area (Fig. 5.31.).

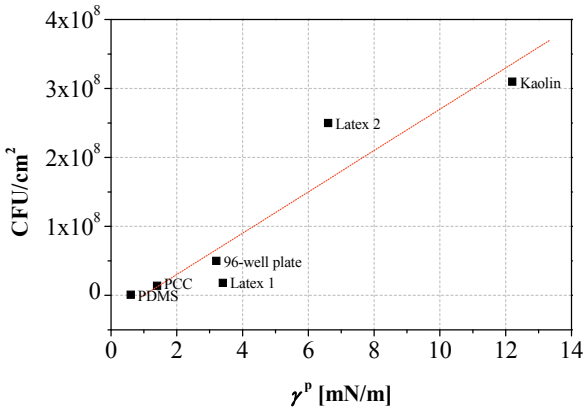

Fig. 5.30. Bacterial concentration values plotted as a function of the polar surface energy component (**Paper II**).

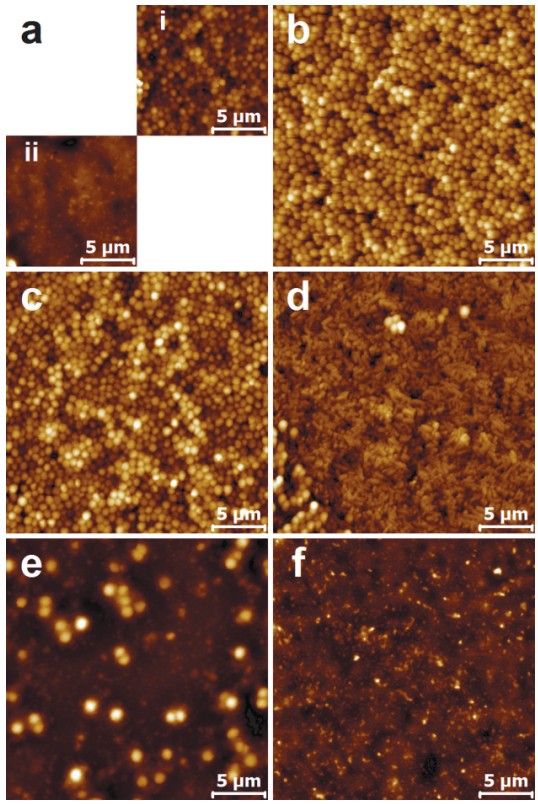

Fig. 5.31. AFM topographical images (25 µm × 25 µm) of a) Latex 1, b) Latex 2, c) Kaolin, d) PCC, e) PS, and f) PDMS exposed to *S. aureus* for 18 h. The z-ranges are: a i) 768.1 nm, ii) 469.2 nm, b) 1168 nm, c) 748.6 nm, d) 907.2 nm, e) 780.3 nm and f) 158 nm. The scale bar in each image is 5 µm (**Paper II**).

Compared to the other paper substrates the biofilm growth on the Latex 2 sample was easily recognizable using an optical microscope. The contrast change (from light to dark) resulting from the biofilm formation inside the reaction area is shown in Fig.5.32.a and 5.32.b. The biofilm growth on the Latex 2 sample is explained by the moderate roughness that increases the contact area between the substrate and bacterium.[177] The Latex 2 substrate was selected for demonstrating the suitability of the platform e.g. in screening of potential anti-biofilm agents. Fig. 5.32.c shows that when the 18 h grown biofilm was exposed to (+)-dehydroabietic acid, an anti-biofilm agent that inhibits *S. aureus* biofilms[310], the contrast changed back from dark to light apart from the edges of the reaction area. AFM measurements together with the decreased CFU value confirm the destruction of the biofilm (Fig. 5.33).

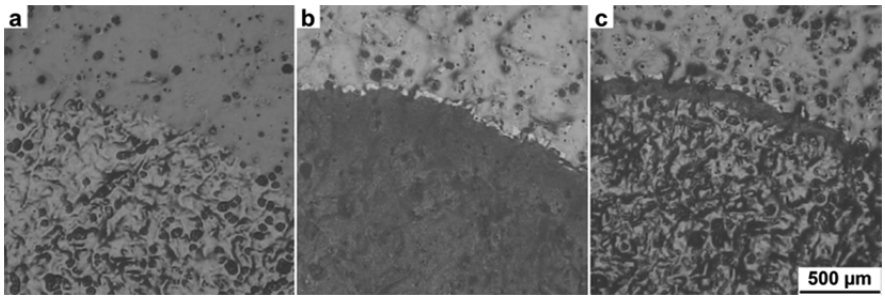

Fig. 5.32. Optical micrographs of Latex 2 sample a) before and b) after biofilm formation and c) after the 18 h grown biofilm was exposed to anti-biofilm agent (+)-dehydroabietic acid for 24 h (**Paper II**).

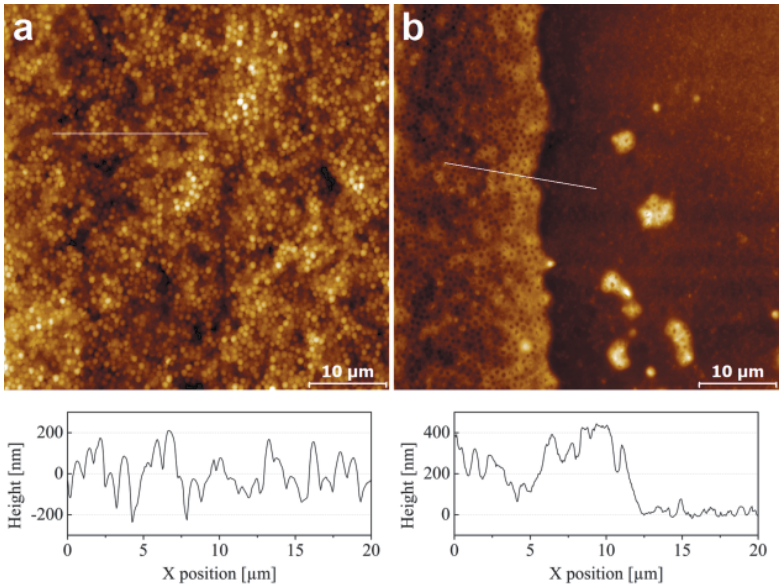

Fig. 5.33. AFM topographical images of a) a *S. aureus* biofilm on Latex 2 and b) *S. aureus* biofilm exposed to anti-biofilm agent (+)-dehydroabietic acid for 24 h. The thickness of the viable biofilm is higher that the thickness of the remaining biofilm near the edge of the reaction area (**Paper II**).

The flexibility and planarity of the platforms enables another strategy for high-throughput screening of potential anti-biofilm agents (or substances that enhance biofilm formation). According to preliminary tests, inkjet printing looks to be a promising technique for printing anti-biofilm compounds on the reaction areas prior to the biofilm formation for screening of the anti-biofilm activity.

5.4.2. Glucose sensors

Rapid and accurate determination of glucose concentration in blood is of great importance for diabetic persons. A typical level of glucose (fasting) in blood, urine, and tear is around 4.2 mM, 0.33 mM and 0.20 mM, respectively.[76,311] Elevated glucose levels e.g. above 7.0 mM in blood (fasting)[312], above 1.4 mM in urine[313] and higher than 0.66 mM in

tear after a postprandial phase or glucose load[311] are indicative of a disease.

Since the first biosensor introduced by Clark and Lyons[314] the development of glucose sensors has been immense.[315,316,317] The extremely good stability of GOx[318], the bulk of information available of the characteristics of GOx[319,320,321] and the commercial importance of the glucose sensors mean that a glucose assay is often the preferred choice for verifying the performance of novel microfluidic devices. The convenient thing about the highly developed methods for glucose measurements is that the existing knowledge and e.g. glucometers can be applicable also for the detection of a range of other analytes.[51]

In **Paper I** PDMS was flexographically printed on two commercial paper substrates for creating planar platforms that were used for constructing printed glucose indicators. The reagents were added on the reaction wells by screen printing and the glucose solutions either by drop-casting or dip-casting. The glucose concentration dependent intensity of the colour (Fig. 5.34.) resulting from the enzymatic reaction (Schema 2) was analysed by a combination of a desk top scanner and image analysis program. The response was not linear, but Fig. 5.35 shows the results in logaritmic scale. Reported linear ranges for paper-based glucose sensors in previous studies have ranged from 0 to 5 mg/mL[37], from 0.09 to 5.76 mg/mL and from 0 to 0.9 mg/mL[38]. The results demonstrate that a normal copy paper can be used as a print substrate for creating low-cost platforms for colorimetric assays.

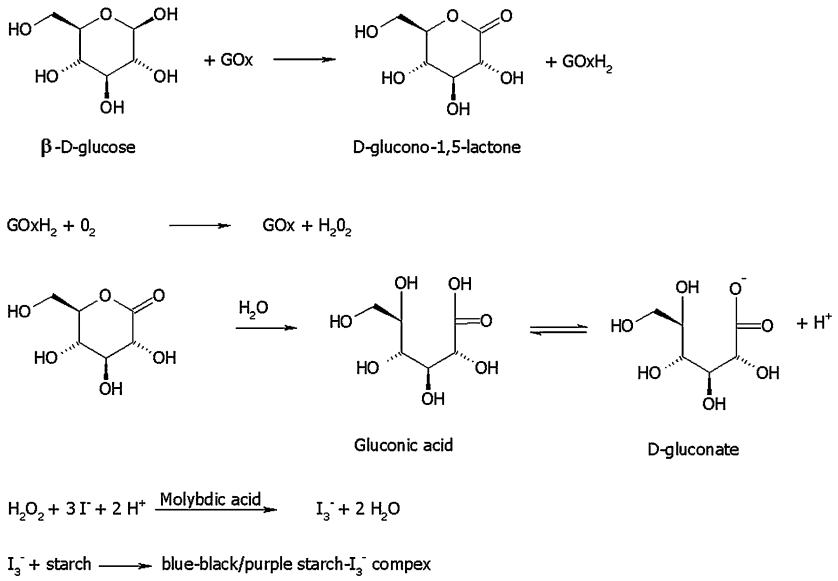

Schema 2. The principle of colour formation in a glucose assay.

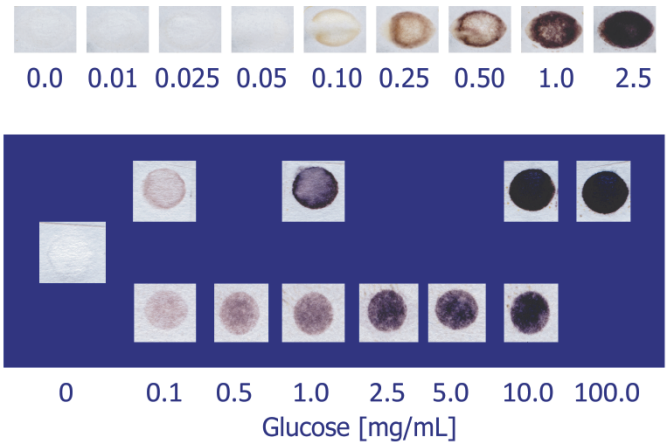

Fig. 5.34. Glucose indicators on coated paper (white background) and copy paper (purple background) (**Paper I**).

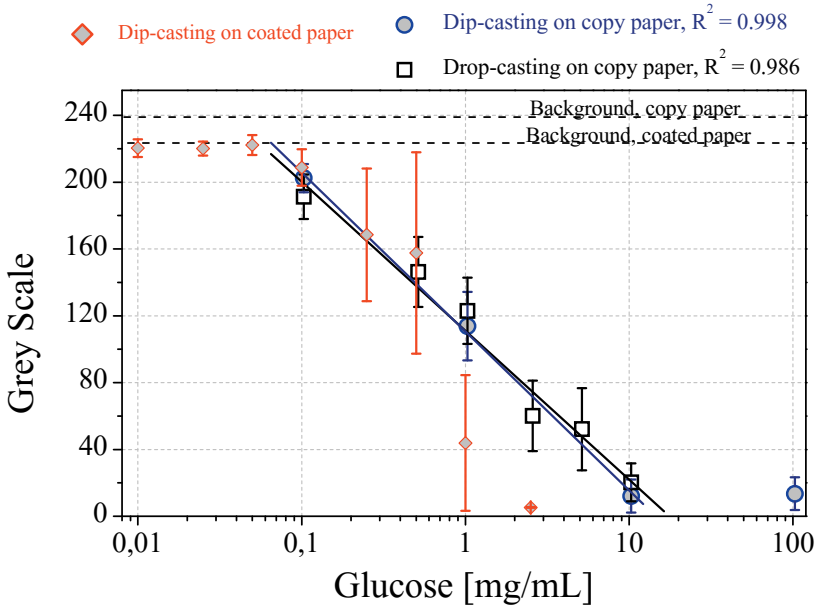

Fig. 5.35. Colour intensities as a function of glucose concentration. The dashed lines indicate the background grey scale values of water (**Paper I**).

In **Paper V** the glucose sensing was carried out with a three-electrode platform with GOx-modified WE by measuring the current response toward solutions with different glucose concentrations (Fig. 5.36.). A typical calibration plot was obtained.[100,322,323] The response was linear up till 5 mM (0.9 mg/mL) and mannose (substrate for GOx at low glucose concentrations[324]) showed practically no current increase for a concentration as high as 20 mM. Various linear ranges, e.g. 0-100[52], 1-22.2[53], 1.5-9.7[325], 2.5-25.0[51], 0.01-1.5 mM[326] have been reported in literature for glucose determination using μPADs.

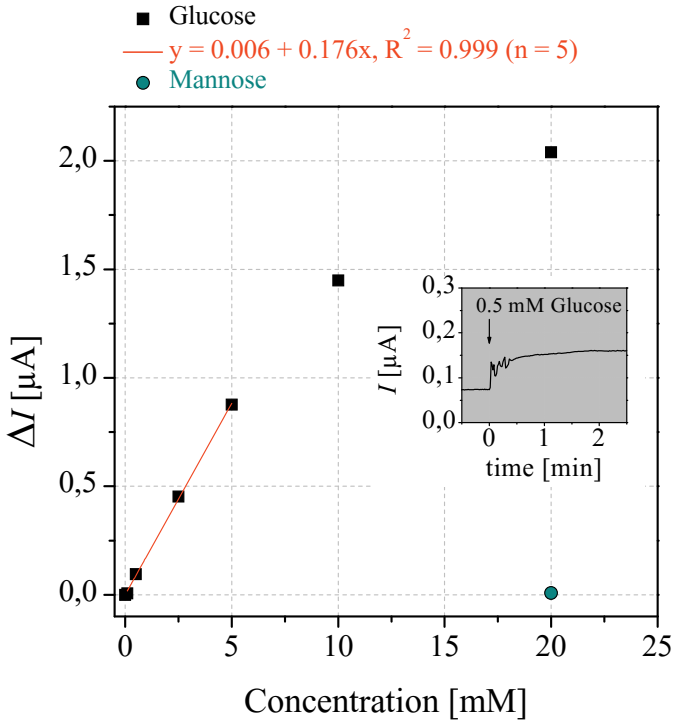

Fig. 5.36. Current response of the glucose sensor towards different concentrations of glucose solutions and a high-concentration mannose solution (**Paper V**).

6. CONCLUSIONS AND OUTLOOK

The main focus in this thesis was set on the development of platforms to be used in paper-based analytical applications. Light weight, low-cost and recyclable/disposable nature of paper are properties that motivate its use. In addition, the physicochemical surface properties of paper can be readily adjusted by the choice of the used coating materials and different surface treatments. This enables the use of paper not only as the substrate but also as a component that improves the functionality and performance of the device. On the other hand, the complex nature of paper surfaces requires that the physicochemical properties of paper surfaces as well as the performance of the printed functionalities are carefully characterized.

In **Paper I**, a simple procedure for manufacturing paper-based reaction arrays and microfluidic channels was demonstrated both by conventional flexographic and digital inkjet printing methods. A hydrophobic PDMS layer was printed on different paper substrates by using a patterned printing plate. This resulted in an array structure including PDMS-free areas, so called reaction areas in which the reagents and analytes of interest could be introduced. For the fabrication of microfluidic channels, highly absorbent paper substrates with good liquid wicking characteristics were used. The printed PDMS ink readily penetrated into such permeable substrates creating liquid guiding barrier structures. The use of the fast curing PDMS ink allowed a straightforward roll-to-roll production of the reaction arrays, which is an advantage compared to other methods, e.g. photolithography that requires several fabrication steps.

Proof-of-concept demonstrations were presented for the reaction arrays. In **Paper I,** a colorimetric glucose sensor was fabricated by printing the assay reagents onto the reaction areas. In **Paper II** the platforms were used in biofilm formation studies. In addition to the control of wetting behavior, the extremely low polarity, surface energy and elastic modulus of the PDMS-based material make it an unfavourable material for

bacterial adhesion. Thus the *S. aureus* biofilm preferably formed on the PDMS-free reaction areas. Measurements of the density of viable biofilm bacteria on the substrates showed that the susceptibility for *S. aureus* biofilm formation grown in static conditions increased as a function of the polarity of the studied substrates. For example, an infrared treated nanopatterned latex substrate was shown to be prone for biofilm formation. The grown biofilms were denser than those grown on plastic microplates. These printed arrays open up future possibilities for high-throughput screening of antimicrobial agents. The planarity of the platform enables e.g. the use of printing techniques for dispensing potential antimicrobial agents into the reaction areas before or after the biofilm formation. This was successfully demonstrated by printing penicillin on the reaction arrays before biofilm formation experiments and by exposing biofilms to an efficient antimicrobial agent, (+)-dehydroabietic acid.

The focus in **Papers III–V** was set on the development and characterization of paper-based platforms for electrochemical applications. Coated paper substrates provided the best platform for applications where good print resolution and barrier properties are required.

The platforms were built on a recently patented multilayer coated mineral pigment based substrate that was developed for printed electronics. The substrate contains a barrier layer that prevents functional inks from penetrating deep into the paper structure. The barrier layer is covered by a few micrometers thick pigment-based top coating, with adjustable surface characteristics such as pore volume, pore size, topography, roughness, stiffness and surface energy.

Compared to the fabrication of the silver electrodes using an ink with ~30 nm sized Ag nanoparticles, fabrication of defect-free and conductive inkjet-printed gold electrodes was a challenging task. The use of organic solvents and extremely small 3-5 nm sized Au nanoparticles set high demands for the barrier properties. On the other hand, the lower melting point of the small nanoparticles enabled fusing

of the particles by a roll-to-roll compatible IR-sintering method. The achieved conductivity (6.25×10^6 S/m) of the crystalline gold surfaces was comparable with previously reported values obtained for printed Au electrodes on glass substrates. This shows that the relatively rough and porous surface of the paper substrate was not an obstacle but it could be utilized to improve e.g. the adhesion of the sintered gold electrodes to the substrate. Compared to glass, the adhesion on paper was excellent and the electrodes withstood washing, abrasion and bending without losing their functionality.

The planarity of the reaction platforms means that not only the transport and storing is simple, but also handling and e.g. surface characterization is easy. Electrochemical analyses were straightforward to perform because of the predetermined and fixed placing of the electrodes that helped to avoid e.g. contact problems. In addition, only low sample volumes are required if compared to a traditional three-electrode cell. Cyclic voltammetry experiments were carried out to verify the performance of the printed electrochemical platforms. The platforms behaved as expected and gave systematic results that were comparable with the ones obtained with the traditional electrochemical cells showing no holdback for advanced applications. To this end, different methods were tested to functionalize the gold working electrode surfaces. PEDOT-GOx films were electropolymerized for fabrication of an electrochemical glucose sensor. Respectively, PANI films were electropolymerized for pH monitoring purpose. Thiolation of the gold electrodes was done using octadecanethiol self-assembled monolayers. Both chemical and electrochemical characterization indicated that the electrodes can be successfully functionalized by various methods and materials. This opens up a wide range of possibilities in the field of analytical applications.

The material costs for the gold ink, the most expensive ink used in this thesis, were 0.04 €/cm^2, which is fairly low compared to the price of a commercial gold disk electrode (120 €)[327]. In order to achieve high volume manufacturing and even lower production costs the platforms

ought to be fabricated in a roll-to-roll process. This is a really interesting future prospect due to the good solution-processability and fast annealing times of the silver, gold and PDMS-based inks.

Other related and interesting future prospects include testing of new electrode materials, functionalization of the electrodes by inkjet printing with the aim to fabricate fully inkjet-printed sensors, optimization of the printing processes for providing guaranteed device-to-device reproducibility and determination of the recommended device lifetime by systematic testing and calibrations. Eventually, real onsite analysis and coupling to portable readers could be investigated.

7. REFERENCES

1. Liana DD, Raguse B, Gooding JJ, Chow E. Recent advances in paper-based sensors. *Sensors* 2012;12:11505-11526. doi:10.3390/s120911505.

2. Yager P, Edwards T, Fu E, et al. Microfluidic diagnostic technologies for global public health. *Nature* 2006;442(7101):412-418. doi:10.1038/nature05064.

3. Stiene M, Bilitewski U. Electrochemical characterization of screen-printed carbonaceous electrodes for the determination of peroxidase activity in novel screen-printed flow-through modules. Anal. Bioanal. Chem. 2002;372(2):240-247. doi:10.1007/s00216-001-1208-4.

4. Fu E, Liang T, Spicar-Mihalic P, Houghtaling J, Ramachandran S, Yager P. Two-dimensional paper network format that enables simple multistep assays for use in low-resource settings in the context of malaria antigen detection. Anal. Chem. 2012;84(10):4574-4579. doi:10.1021/ac300689s.

5. Ballerini DR, Li X, Shen W. Patterned paper and alternative materials as substrates for low-cost microfluidic diagnostics. Microfluid. Nanofluidics 2012;13(5):769-787. doi:10.1007/s10404-012-0999-2.

6. Martinez AW, Phillips ST, Whitesides GM, Carrilho E. Diagnostics for the developing world: microfluidic paper-based analytical devices. Anal. Chem. 2010;82(1):3-10. doi:10.1021/ac9013989.

7. Abe K, Suzuki K, Citterio D. Inkjet-printed microfluidic multianalyte chemical sensing paper. Anal. Chem. 2008;80(18):6928-6934. doi:10.1021/ac800604v.

8. Hüser J, Mannhold R, Kubinyi H, Folkers G. High-throughput screening in drug discovery (Methods and principles in medicinal chemistry). 1st ed. Weinheim, Germany: Wiley-VCH Verlagsgesellschaft mbH & Co. KGaA; 2006.

9. Astle TW. Microplate standardization. Mol. Online 1997;1(9):106-113.

10. Buchholz K, Burke TA, Williamson KC, Wiegand RC, Wirth DF, Marti M. A High-throughput screen targeting malaria transmission stages opens new avenues for drug development. J. Infect. Dis. 2011;203(10):1445-1453. doi:10.1093/infdis/jir037.

11. Atiq N, Ahmed S, Ali IM, Andleeb S, Ahmad B, Robson G. Isolation and identification of polystyrene biodegrading bacteria from soil. Afr. J. Microbiol. Res. 2010;4(14):1537-1541.

12. Bacteria turn styrofoam into biodegradable plastic: Scientific American. Available at: http://www.scientificamerican.com/article.cfm?id=bacteria-turn-styrofoam-i. Accessed May 28, 2014.

13. Carrilho E, Phillips ST, Vella SJ, Martinez AW, Whitesides GM. Paper microzone plates. Anal. Chem. 2009;81(15):5990-5998. doi:10.1021/ac900847g.

14. Abgrall P, Conedera V, Camon H, Gue A-M, Nguyen N-T. SU-8 as a structural material for labs-on-chips and microelectromechanical systems. Electrophoresis 2007;28(24):4539–4551. doi:10.1002/elps.200700333.

15. Li XJ, Nie ZH, Cheng C-M, Goodale AB, Whitesides GM. Paper-based electrochemical ELISA. In: Groningen, The Netherlands; 2010:1487-1489. Available at: http://www.rsc.org/binaries/LOC/2010/PDFs/Papers/507_0930.pdf.

16. Bracher PJ, Gupta M, Whitesides GM. Shaped films of ionotropic hydrogels fabricated using templates of patterned paper. Adv. Mater. 2009;21(4):445–450. doi:10.1002/adma.200801186.

17. Bracher PJ, Gupta M, Whitesides GM. Patterned paper as a template for the delivery of reactants in the fabrication of planar materials. Soft Matter 2010;6(18):4303-4309. doi:10.1039/C0SM00031K.

18. Ellerbee AK, Phillips ST, Siegel AC, et al. Quantifying colorimetric assays in paper-based microfluidic devices by measuring the transmission of light through paper. Anal. Chem. 2009;81(20):8447-8452. doi:10.1021/ac901307q.

19. Carrilho E, Martinez AW, Whitesides GM. Understanding wax printing: A simple micropatterning process for paper-based microfluidics. Anal. Chem. 2009;81(16):7091-7095. doi:10.1021/ac901071p.

20. Yager P, Fu E, Liang T, Lutz B, Osborn JL. A two-dimensional paper network for comprehensive dengue detection at the point of care. In: Seattle, Washington, USA; 2011:2092-2095. Available at: http://www.rsc.org/images/LOC/2011/PDFs/Papers/698_8000.pdf.

21. Apilux A, Ukita Y, Chikae M, Chailapakul O, Takamura Y. Development of automated paper-based devices for sequential multistep sandwich enzyme-linked immunosorbent assays using inkjet printing. Lab. Chip 2012;13(1):126-135. doi:10.1039/C2LC40690J.

22. Orelma H, Filpponen I, Johansson L-S, Osterberg M, Rojas OJ, Laine J. Surface functionalized nanofibrillar cellulose (NFC) film as a platform for immunoassays and diagnostics. Biointerphases 2012;7(1-4):61. doi:10.1007/s13758-012-0061-7.

23. Mark D, Haeberle S, Roth G, von Stetten F, Zengerle R. Microfluidic lab-on-a-chip platforms: requirements, characteristics and applications. Chem. Soc. Rev. 2010;39(3):1153. doi:10.1039/b820557b.

24. Müller RH, Clegg DL. Automatic Paper Chromatography. Anal. Chem. 1949;21(9):1123-1125. doi:10.1021/ac60033a032.

25. Glad C, Grubb AO. Immunocapillarymigration—A new method for immunochemical quantitation. Anal. Biochem. 1978;85(1):180-187. doi:10.1016/0003-2697(78)90288-9.

26. Martinez AW, Phillips ST, Butte MJ, Whitesides GM. Patterned paper as a platform for inexpensive, low-volume, portable bioassays. Angew. Chem. Int. Ed Engl. 2007;46(8):1318-1320. doi:10.1002/anie.200603817.

27. Li X, Ballerini DR, Shen W. A perspective on paper-based microfluidics: Current status and future trends. Biomicrofluidics 2012;6(1):011301. doi:10.1063/1.3687398.

28. Fenton EM, Mascarenas MR, López GP, Sibbett SS. Multiplex lateral-flow test strips fabricated by two-dimensional shaping. ACS Appl. Mater. Interfaces 2009;1(1):124-129. doi:10.1021/am800043z.

29. Li X, Tian J, Nguyen T, Shen W. Paper-based microfluidic devices by plasma treatment. *Anal. Chem.* 2008;80(23):9131-9134. doi:10.1021/ac801729t.

30. Chitnis G, Ding Z, Chang C-L, Savran CA, Ziaie B. Laser-treated hydrophobic paper: an inexpensive microfluidic platform. *Lab. Chip* 2011;11(6):1161-1165. doi:10.1039/C0LC00512F.

31. Li X, Tian J, Garnier G, Shen W. Fabrication of paper-based microfluidic sensors by printing. *Colloids Surf. B Biointerfaces* 2010;76(2):564-570. doi:10.1016/j.colsurfb.2009.12.023.

32. Maejima K, Tomikawa S, Suzuki K, Citterio D. Inkjet printing: an integrated and green chemical approach to microfluidic paper-based analytical devices. *RSC Adv.* 2013;3(24):9258-9263. doi:10.1039/C3RA40828K.

33. Dungchai W, Chailapakul O, Henry CS. A low-cost, simple, and rapid fabrication method for paper-based microfluidics using wax screen-printing. *The Analyst* 2011;136:77. doi:10.1039/c0an00406e.

34. Bruzewicz DA, Reches M, Whitesides GM. Low-cost printing of poly(dimethylsiloxane) barriers to define microchannels in paper. *Anal. Chem.* 2008;80(9):3387-3392. doi:10.1021/ac702605a.

35. Lu Y, Shi W, Jiang L, Qin J, Lin B. Rapid prototyping of paper-based microfluidics with wax for low-cost, portable bioassay. *Electrophoresis* 2009;30(9):1497-1500. doi:10.1002/elps.200800563.

36. Olkkonen J, Lehtinen K, Erho T. Flexographically printed fluidic structures in paper. *Anal. Chem.* 2010;82(24):10246-10250. doi:10.1021/ac1027066.

37. Songjaroen T, Dungchai W, Chailapakul O, Laiwattanapaisal W. Novel, simple and low-cost alternative method for fabrication of paper-based microfluidics by wax dipping. *Talanta* 2011;85(5):2587-2593. doi:10.1016/j.talanta.2011.08.024.

38. Martinez AW, Phillips ST, Carrilho E, Thomas SW, Sindi H, Whitesides GM. Simple telemedicine for developing regions: Camera phones and paper-based microfluidic devices for real-time, off-site diagnosis. *Anal. Chem.* 2008;80(10):3699-3707. doi:10.1021/ac800112r.

39. Li M, Tian J, Al-Tamimi M, Shen W. Paper-based blood typing device that reports patient's blood type "in writing." *Angew. Chem. Int. Ed.* 2012;51(22):5497–5501. doi:10.1002/anie.201201822.

40. Dunfield EM, Wu YY, Remcho TP, Koesdjojo MT, Remcho VT. Simple and rapid fabrication of paper microfluidic devices utilizing Parafilm®. 2012. Available at: http://blogs.rsc.org/chipsandtips/2012/04/10/simple-and-rapid-fabrication-of-paper-microfluidic-devices-utilizing-parafilm%C2%AE/.

41. Gillespie T. The capillary rise of a liquid in a vertical strip of filter paper. *J. Colloid Sci.* 1959;14(2):123-130. doi:10.1016/0095-8522(59)90036-4.

42. Hodgson KT, Berg JC. The effect of surfactants on wicking flow in fiber networks. *J. Colloid Interface Sci.* 1988;121(1):22-31. doi:10.1016/0021-9797(88)90404-3.

43. Washburn EW. The dynamics of capillary flow. *Phys. Rev.* 1921;17(3):273-283. doi:10.1103/PhysRev.17.273.

44. Jahanshahi-Anbuhi S, Chavan P, Sicard C, et al. Creating fast flow channels in paper fluidic devices to control timing of sequential reactions. *Lab. Chip* 2012;12(23):5079-5085. doi:10.1039/C2LC41005B.

45. Fu E, Lutz B, Kauffman P, Yager P. Controlled reagent transport in disposable 2D paper networks. *Lab. Chip* 2010;10(7):918-920. doi:10.1039/B919614E.

46. Fu E, Kauffman P, Lutz B, Yager P. Chemical signal amplification in two-dimensional paper networks. *Sens. Actuators B Chem.* 2010;149(1):325-328. doi:10.1016/j.snb.2010.06.024.

47. Renedo OD, Alonso-Lomillo MA, Martínez MJA. Recent developments in the field of screen-printed electrodes and their related applications. *Talanta* 2007;73(2):202-219. doi:10.1016/j.talanta.2007.03.050.

48. Falciola L, Pifferi V, Mascheroni E. Platinum-based and carbon-based screen printed electrodes for the determination of benzidine by differential pulse voltammetry. *Electroanalysis* 2012;24(4):767–775. doi:10.1002/elan.201200007.

49. Kröger S, Setford SJ, Turner APF. Electrochemical assay method for the rapid determination of oxidase enzyme activities. *Biotechnol. Tech.* 1998;12(2):123-127. doi:10.1023/A:1008836416656.

50. DropSens/Screen-printed electrodes. Available at: http://www.dropsens.com/en/screen_printed_electrodes_pag.html. Accessed June 18, 2013.

51. Nie Z, Deiss F, Liu X, Akbulut O, Whitesides GM. Integration of paper-based microfluidic devices with commercial electrochemical readers. *Lab. Chip* 2010;10(22):3163-3169. doi:10.1039/c0lc00237b.

52. Dungchai W, Chailapakul O, Henry CS. Electrochemical detection for paper-based microfluidics. *Anal. Chem.* 2009;81(14):5821-5826. doi:10.1021/ac9007573.

53. Nie Z, Nijhuis CA, Gong J, et al. Electrochemical sensing in paper-based microfluidic devices. *Lab Chip* 2010;10(4):477-483. doi:10.1039/B917150A.

54. García-González R, Fernández-Abedul MT, Pernía A, Costa-García A. Electrochemical characterization of different screen-printed gold electrodes. *Electrochimica Acta* 2008;53(8):3242-3249. doi:10.1016/j.electacta.2007.07.059.

55. Hu C, Bai X, Wang Y, Jin W, Zhang X, Hu S. Inkjet printing of nanoporous gold electrode arrays on cellulose membranes for high-sensitive paper-like electrochemical oxygen sensors using ionic liquid electrolytes. *Anal. Chem.* 2012;84(8):3745-3750. doi:10.1021/ac3003243.

56. Labib M, Martić S, Shipman PO, Kraatz H-B. Electrochemical analysis of HIV-1 reverse transcriptase serum level: Exploiting protein binding to a functionalized nanostructured surface. *Talanta* 2011;85(1):770-778. doi:10.1016/j.talanta.2011.04.070.

57. Tan SN, Ge L, Wang W. Paper disk on screen printed electrode for one-step sensing with an internal standard. *Anal. Chem.* 2010;82(21):8844-8847. doi:10.1021/ac1015062.

58. Paul D. Biosensors in clinical chemistry. *Clin. Chim. Acta* 2003;334(1-2):41-69. doi:10.1016/S0009-8981(03)00241-9.

59. Reference ranges for blood tests. Available at: http://upload.wikimedia.org/wikipedia/commons/8/84/Blood_values_sorted_by_mass_and_molar_concentration.svg. Accessed September 4, 2013.

60. Chen J-C, Chung H-H, Hsu C-T, Tsai D-M, Kumar AS, Zen J-M. A disposable single-use electrochemical sensor for the detection of uric acid in human whole blood. *Sens. Actuators B Chem.* 2005;110(2):364-369. doi:10.1016/j.snb.2005.02.026.

61. Quadros ME, Marr LC. Environmental and human health risks of aerosolized silver nanoparticles. *J. Air Waste Manag. Assoc.* 2010;60(7):770-781. doi:10.3155/1047-3289.60.7.770.

62. Kumar S, Aaron J, Sokolov K. Directional conjugation of antibodies to nanoparticles for synthesis of multiplexed optical contrast agents with both delivery and targeting moieties. *Nat. Protoc.* 2008;3(2):314-320. doi:10.1038/nprot.2008.1.

63. Moreno M, González VM, Rincón E, Domingo A, Domínguez E. Aptasensor based on the selective electrodeposition of protein-linked gold nanoparticles on screen-printed electrodes. *The Analyst* 2011;136(9):1810-1815. doi:10.1039/c1an15070g.

64. Mandler D, Kraus-Ophir S. Self-assembled monolayers (SAMs) for electrochemical sensing. *J. Solid State Electrochem.* 2011;15:1535-1558.

65. Abad-Valle P, Fernández-Abedul MT, Costa-García A. Genosensor on gold films with enzymatic electrochemical detection of a SARS virus sequence. *Biosens. Bioelectron.* 2005;20(11):2251-2260. doi:10.1016/j.bios.2004.10.019.

66. Salam F, Tothill IE. Detection of Salmonella typhimurium using an electrochemical immunosensor. *Biosens. Bioelectron.* 2009;24(8):2630-2636. doi:10.1016/j.bios.2009.01.025.

67. Bonanni A, Pumera M, Miyahara Y. Influence of gold nanoparticle size (2-50 nm) upon its electrochemical behavior: an electrochemical impedance spectroscopic and voltammetric study. *Phys. Chem. Chem. Phys. PCCP* 2011;13(11):4980-4986. doi:10.1039/c0cp01209b.

68. De la Escosura-Muñiz A, Parolo C, Maran F, Mekoçi A. Size-dependent direct electrochemical detection of gold nanoparticles: application in magnetoimmunoassays. *Nanoscale* 2011;3(8):3350-3356. doi:10.1039/c1nr10377f.

69. Regiart M, Fernández-Baldo MA, Spotorno VG, Bertolino FA, Raba J. Ultra sensitive microfluidic immunosensor for determination of clenbuterol in bovine hair samples using electrodeposited gold nanoparticles and magnetic micro particles as bio-affinity platform. *Biosens. Bioelectron.* 2013;41:211-217. doi:10.1016/j.bios.2012.08.020.

70. Pereira SV, Bertolino FA, Fernández-Baldo MA, et al. A microfluidic device based on a screen-printed carbon electrode with electrodeposited gold nanoparticles for the detection of IgG anti-Trypanosoma cruzi antibodies. *Analyst* 2011;136(22):4745-4751. doi:10.1039/C1AN15569E.

71. Loaiza OA, Lamas-Ardisana PJ, Jubete E, et al. Nanostructured disposable impedimetric sensors as tools for specific biomolecular interactions: sensitive recognition of concanavalin A. *Anal. Chem.* 2011;83(8):2987-2995. doi:10.1021/ac103108m.

72. Carvalhal RF, Simão Kfouri M, de Oliveira Piazetta MH, Gobbi AL, Kubota LT. Electrochemical detection in a paper-based separation device. *Anal. Chem.* 2010;82(3):1162-1165. doi:10.1021/ac902647r.

73. Apilux A, Dungchai W, Siangproh W, Praphairaksit N, Henry CS, Chailapakul O. Lab-on-paper with dual electrochemical/colorimetric detection for simultaneous determination of gold and iron. *Anal. Chem.* 2010;82(5):1727-1732. doi:10.1021/ac9022555.

74. Jokerst JC, Adkins JA, Bisha B, Mentele MM, Goodridge LD, Henry CS. Development of a paper-based analytical device for colorimetric detection of select foodborne pathogens. *Anal. Chem.* 2012;84(6):2900-2907. doi:10.1021/ac203466y.

75. Development of a paper microfluidic platform for detection of viral gastroenteritis. *West. Reg. Cent. Excell. Biodefense Emerg. Infect. Dis. Res. - Individ. Proj. CD007*. Available at: http://www.utmb.edu/wrce/CD007.html. Accessed May 28, 2014.

76. Dungchai W, Chailapakul O, Henry CS. Use of multiple colorimetric indicators for paper-based microfluidic devices. *Anal. Chim. Acta* 2010;674(2):227-233. doi:10.1016/j.aca.2010.06.019.

77. Mentele MM, Cunningham J, Koehler K, Volckens J, Henry CS. Microfluidic paper-based analytical device for particulate metals. *Anal. Chem.* 2012;84(10):4474-4480. doi:10.1021/ac300309c.

78. Hossain SMZ, Brennan JD. ß-Galactosidase-based colorimetric paper sensor for determination of heavy metals. *Anal. Chem.* 2011;83(22):8772-8778. doi:10.1021/ac202290d.

79. Klasner SA, Price AK, Hoeman KW, Wilson RS, Bell KJ, Culbertson CT. Paper-based microfluidic devices for analysis of clinically relevant analytes present in urine and saliva. *Anal. Bioanal. Chem.* 2010;397(5):1821-1829. doi:10.1007/s00216-010-3718-4.

80. Cheng C-M, Martinez AW, Gong J, et al. Paper-based ELISA. *Angew. Chem. Int. Ed.* 2010;49(28):4771–4774. doi:10.1002/anie.201001005.

81. Agostini E, Hernández-Ruiz J, Arnao MB, Milrad SR, Tigier HA, Acosta M. A peroxidase isoenzyme secreted by turnip (Brassica napus) hairy-root cultures: inactivation by hydrogen peroxide and application in diagnostic kits. *Biotechnol. Appl. Biochem.* 2002;35(Pt 1):1-7.

82. Hale PD, Boguslavsky LI, Inagaki T, et al. Amperometric glucose biosensors based on redox polymer-mediated electron transfer. *Anal. Chem.* 1991;63(7):677-682. doi:10.1021/ac00007a006.

83. Avrameas S. Coupling of enzymes to proteins with glutaraldehyde. Use of the conjugates for the detection of antigens and antibodies. *Immunochemistry* 1969;6(1):43-52.

84. Engvall E, Perlmann P. Enzyme-linked immunosorbent assay (ELISA). Quantitative assay of immunoglobulin G. *Immunochemistry* 1971;8(9):871-874.

85. Van Weemen BK, Schuurs AHWM. Immunoassay using antigen-enzyme conjugates. *FEBS Lett.* 1971;15(3):232-236.

86. Hamid M, Khalil-ur-Rehman. Potential applications of peroxidases. *Food Chem.* 2009;115(4):1177-1186. doi:10.1016/j.foodchem.2009.02.035.

87. *ELISA Technical Guide and Protocols*. Thermo Scientific Available at: http://www.piercenet.com/files/TR0065-ELISA-guide.pdf.

88. Maruthamuthu M, Kishore S. Bromocresol green as a new spectrophotometric probe for serum albumins. *Proc. Indian Acad. Sci. - Chem. Sci.* 1988;100(6):525-533. doi:10.1007/BF02841127.

89. Pugia MJ, Lott JA, Profitt JA, Cast TK. High-sensitivity dye binding assay for albumin in urine. *J. Clin. Lab. Anal.* 1999;13(4):180–187. doi:10.1002/(SICI)1098-2825(1999)13:4<180::AID-JCLA7>3.0.CO;2-R.

90. Lau ALY. Method for assaying for proteins using a dual indicator reagent composition. 1991. Available at: https://docs.google.com/a/google.com/viewer?url=www.google.com/patents/US5077222.pdf.

91. *Albumin - BCG*. Available at: http://www.spectrum-diagnostics.com/data/Albumin.pdf.

92. Al-Tamimi M, Shen W, Zeineddine R, Tran H, Garnier G. Validation of paper-based assay for rapid blood typing. *Anal. Chem.* 2012;84(3):1661-1668. doi:10.1021/ac202948t.

93. Zuman P. Principles of applications of polarography and voltammetry in the analysis of drugs. *FABAD J Pharm Sci* 2006;31:97-115.

94. D'Orazio P. Biosensors in clinical chemistry. *Clin. Chim. Acta Int. J. Clin. Chem.* 2003;334(1-2):41-69.

95. Bard AJ, Faulkner LR. Electrochemical Methods: Fundamentals and Applications. Wiley; 2001.

96. Matysik F-M. Experimental characterization of end-column electrochemical detection in conjunction with nonaqueous capillary electrophoresis. *Anal. Chem.* 2000;72(11):2581-2586. doi:10.1021/ac991326x.

97. Rao SP, Singh SR, Bandakavi SR. Formal redox potentials of ferricyanide ferrocyanide couple in certain non-aqueouswater mixtures. *Proc Indian Natl Sci Acad Part A* 1978;44(6):333-335.

98. Ye B, Zhou X. Direct electrochemistry of hemoglobin at a bare silver electrode promoted by cetyl pyridinium chloride and its application in analysis. *Electroanalysis* 1996;8(12):1165–1168. doi:10.1002/elan.1140081218.

99. Bott AW. Electrochemical methods for the determination of glucose. *Curr. Sep.* 1998;17:25-31.

100. Zhu J, Zhu Z, Lai Z, et al. Planar amperometric glucose sensor based on glucose oxidase immobilized by chitosan film on Prussian blue layer. *Sensors* 2002;2(4):127-136. doi:10.3390/s20400127.

101. Wring SA, Hart JP. Chemically modified, carbon-based electrodes and their application as electrochemical sensors for the analysis of biologically important compounds. A review. *Analyst* 1992;117(8):1215-1229. doi:10.1039/AN9921701215.

102. Tian F, Zhu G. Bienzymatic amperometric biosensor for glucose based on polypyrrole/ceramic carbon as electrode material. *Anal. Chim. Acta* 2002;451(2):251-258. doi:10.1016/S0003-2670(01)01405-2.

103. Guisán JM. *Immobilization of enzymes and cells*. Totowa, New Jersey: Humana Press; 2010.

104. Tischer W, Wedekind F. Immobilized enzymes: Methods and applications. In: Fessner PDW-D, Archelas A, Demirjian DC, et al., eds. *Biocatalysis - From Discovery to Application*. Topics in Current Chemistry. Springer Berlin Heidelberg; 1999:95-126.

105. Mosbach K, ed. Immobilized enzymes and cells part D in Methods in enzymology. New York: Academic Press; 1988.

106. Guilbault GE. *Handbook of immobilized enzymes*. New York: Marcel-Dekker; 1984.

107. Ganesh V, Muthurasu A. Strategies for an enzyme immobilization on electrodes: Structural and electrochemical characterizations. *J. Phys. Conf. Ser.* 2012;358(1):012003. doi:10.1088/1742-6596/358/1/012003.

108. Anandan V, Gangadharan R, Zhang G. Role of SAM chain length in enhancing the sensitivity of nanopillar modified electrodes for glucose detection. *Sensors* 2009;9(3):1295-1305. doi:10.3390/s90301295.

109. Alonso Lomillo MA, Ruiz JG, Pascual FJM. Biosensor based on platinum chips for glucose determination. *Anal. Chim. Acta* 2005;547(2):209-214. doi:10.1016/j.aca.2005.05.037.

110. Kochius S, Magnusson AO, Hollmann F, Schrader J, Holtmann D. Immobilized redox mediators for electrochemical NAD(P)+ regeneration. *Appl. Microbiol. Biotechnol.* 2012;93(6):2251-2264. doi:10.1007/s00253-012-3900-z.

111. Zoski CG. *Handbook of electrochemistry*. Elsevier; 2007.

112. *Educator's reference guide for electrochemistry*. Grove City, Pennsylvania: Pine Instrument Company; 2000. Available at: http://www.pineinst.com/echem/files/lmcbp-prof1.pdf.

113. Avramescu A., Noguer T., Magearu V., Marty J.-L. Chronoamperometric determination of d-lactate using screen-printed enzyme electrodes. *Anal. Chim. Acta* 2001;433(1):81-88. doi:10.1016/S0003-2670(00)01386-6.

114. Settle FA. Handbook of instrumental techniques for analytical chemistry. Prentice Hall PTR; 1997.

115. Drake KF, Van Duyne RP, Bond AM. Cyclic differential pulse voltammetry: a versatile instrumental approach using a computerized system. *J Electroanal Chem* 1978;89:231-246.

116. Yu J-S, Zhang Z-X. Double potential-step chronoamperometry and chronocoulometry at an ultramicrodisk electrode: Theory and experiment. *J. Electroanal. Chem.* 1997;439(1):73-80. doi:10.1016/S0022-0728(97)00258-1.

117. Kissinger PT, Heineman WR. Cyclic voltammetry. *J Chem Educ* 1983;60(9):702-706. doi:10.1021/ed060p702.

118. Volpe G, Compagnone D, Draisci R, Palleschi G. 3,3',5,5' -Tetramethylbenzidine as electrochemical substrate for horseradish peroxidase based enzyme immunoassays. A comparative study. *Analyst* 1998;123:1303-1307.

119. He Z, Jin W. Capillary electrophoretic enzyme immunoassay with electrochemical detection for thyroxine. *Anal. Biochem.* 2003;313(1):34-40. doi:10.1016/S0003-2697(02)00508-0.

120. White RJ, Kallewaard HM, Hsieh W, et al. Wash-free, electrochemical platform for the quantitative, multiplexed detection of specific antibodies. *Anal. Chem.* 2012;84(2):1098-1103. doi:10.1021/ac202757c.

121. Kong F-Y, Xu B-Y, Du Y, Xu J-J, Chen H-Y. A branched electrode based electrochemical platform: towards new label-free and reagentless simultaneous detection of two biomarkers. *Chem. Commun.* 2013;49(11):1052-1054. doi:10.1039/C2CC37675J.

122. Wang ZF, Stein R, Sharkey RM, Goldenberg DM. Carcinoembryonic antigen and alpha-fetoprotein expression and monoclonal antibody targeting in a human hepatoma/nude mouse model. *Cancer Res.* 1990;50(3_Supplement):869s-872s.

123. Novell M, Parrilla M, Crespo GA, Rius FX, Andrade FJ. Paper-based ion-selective potentiometric sensors. *Anal. Chem.* 2012;84(11):4695-4702. doi:10.1021/ac202979j.

124. A guide to pH measurement - the theory and practice of laboratory pH applications. Available at: http://uk.mt.com/gb/en/home/supportive_content/tips_and_tricks/Guide_pH_meas/jcr:content/download/file/file.res/51300047_pH-Guide_E.pdf and http://www.alliancets.com/site/files/408/29497/109873/159912/Guide_to_pH_Measurement.pdf.

125. Macdonald JR. Impedance spectroscopy. *Ann. Biomed. Eng.* 1992;20(3):289-305. doi:10.1007/BF02368532.

126. Dulay S, Lozano-Sánchez P, Iwuoha E, Katakis I, O'Sullivan CK. Electrochemical detection of celiac disease-related anti-tissue transglutaminase antibodies using thiol based surface chemistry. *Biosens. Bioelectron.* 2011;26(9):3852-3856. doi:10.1016/j.bios.2011.02.045.

127. Helali S. Impedimetric Immunosensor for Pesticide Detection. In: Rinken T, ed. *State of the Art in Biosensors - Environmental and Medical Applications*. InTech; 2013. Available at: http://www.intechopen.com/books/state-of-the-art-in-biosensors-environmental-and-medical-applications/impedimetric-immunosensor-for-pesticide-detection. Accessed June 19, 2013.

128. Mansfeld F. *An introduction to electrochemical impedance measurement*. Los Angeles, CA, USA: Solartron; 1999. Available at: http://www.korozja.pl/html/eis/technote26.pdf.

129. *Basics of electrochemical impedance spectroscopy*. Gamry Instruments Available at: http://www.gamry.com/assets/Application-Notes/Basics-of-EIS.pdf.

130. Valera E, Ramón-Azcón J, Rodríguez Á, Castañer LM, Sánchez F-J, Marco M-P. Impedimetric immunosensor for atrazine detection using interdigitated μ-electrodes (IDμE's). *Sens. Actuators B Chem.* 2007;125(2):526-537. doi:10.1016/j.snb.2007.02.048.

131. Chen Y-S, Wu C-C, Tsai J-J, Wang G-J. Electrochemical impedimetric biosensor based on a nanostructured polycarbonate substrate. *Int. J. Nanomedicine* 2012;7:133-140. doi:10.2147/IJN.S27225.

132. Bataillard P, Gardies F, Jaffrezic-Renault N, Martelet C, Colin B, Mandrand B. Direct detection of immunospecies by capacitance measurements. *Anal. Chem.* 1988;60(21):2374-2379. doi:10.1021/ac00172a011.

133. Upstone SL. Ultraviolet/visible light absorption spectrophotometry in clinical chemistry in Encyclopedia of Analytical Chemistry, R.A. Meyers (Ed.). Chichester: ohn Wiley & Sons Ltd; 2000. Available at: http://www.perkinelmer.com/CMSResources/Images/44-74382ATL_UVVisInClinicalChemistry.pdf.

134. Hemmilä I, Dakubu S, Mukkala V-M, Siitari H, Lövgren T. Europium as a label in time-resolved immunofluorometric assays. *Anal. Biochem.* 1984;137(2):335-343. doi:10.1016/0003-2697(84)90095-2.

135. Yu J, Wang S, Ge L, Ge S. A novel chemiluminescence paper microfluidic biosensor based on enzymatic reaction for uric acid determination. *Biosens. Bioelectron.* 2011;26(7):3284-3289. doi:16/j.bios.2010.12.044.

136. Wang S, Ge L, Song X, et al. Paper-based chemiluminescence ELISA: Lab-on-paper based on chitosan modified paper device and wax-screen-printing. *Biosens. Bioelectron.* 2012;31(1):212-218. doi:10.1016/j.bios.2011.10.019.

137. Delaney JL, Hogan CF, Tian J, Shen W. Electrogenerated chemiluminescence detection in paper-based microfluidic sensors. *Anal. Chem.* 2011;83(4):1300-1306. doi:10.1021/ac102392t.

138. Ge L, Yan J, Song X, Yan M, Ge S, Yu J. Three-dimensional paper-based electrochemiluminescence immunodevice for multiplexed measurement of biomarkers and point-of-care testing. *Biomaterials* 2012;33(4):1024-1031. doi:10.1016/j.biomaterials.2011.10.065.

139. Rabe M, Verdes D, Seeger S. Understanding protein adsorption phenomena at solid surfaces. *Adv. Colloid Interface Sci.* 2011;162(1–2):87-106. doi:10.1016/j.cis.2010.12.007.

140. Vogler EA. Protein adsorption in three dimensions. *Biomaterials* 2012;33(5):1201-1237. doi:10.1016/j.biomaterials.2011.10.059.

141. Parhi P, Golas A, Barnthip N, Noh H, Vogler EA. Volumetric interpretation of protein adsorption: Capacity scaling with adsorbate molecular weight and adsorbent surface energy. *Biomaterials* 2009;30(36):6814-6824. doi:10.1016/j.biomaterials.2009.09.005.

142. Treuel L. How protein adsorption shapes the biological identity of NPs – Where do we stand? *J Phys Chem Biophys* 2013;3(2):1000e113.

143. Thevenot P, Hu W, Tang L. Surface chemistry influence implant biocompatibility. *Curr. Top. Med. Chem.* 2008;8(4):270-280.

144. Lee W-H, Loo C-Y, Zavgorodniy AV, Ghadiri M, Rohanizadeh R. A novel approach to enhance protein adsorption and cell proliferation on hydroxyapatite: citric acid treatment. *RSC Adv.* 2013;3(12):4040-4051. doi:10.1039/C3RA22966A.

145. J. M. Kleijn WN. The adsorption of proteins from aqueous solution on solid surfaces. *Heterog. Chem. Rev. 2 1995 157-172*. doi:WebQuery/wurpubs/29857.

146. Norde W. Colloids and interfaces in life sciences and bionanotechnology, Second Edition. CRC Press; 2011.

147. Chen S, Liu L, Zhou J, Jiang S. Controlling antibody orientation on charged self-assembled monolayers. *Langmuir* 2003;19(7):2859-2864. doi:10.1021/la026498v.

148. Jeyachandran YL, Mielczarski JA, Mielczarski E, Rai B. Efficiency of blocking of non-specific interaction of different proteins by BSA adsorbed on hydrophobic and hydrophilic surfaces. *J. Colloid Interface Sci.* 2010;341(1):136-142. doi:10.1016/j.jcis.2009.09.007.

149. Bremer MGEG, Duval J, Norde W, Lyklema J. Electrostatic interactions between immunoglobulin (IgG) molecules and a charged sorbent. *Colloids Surf. Physicochem. Eng. Asp.* 2004;250(1–3):29-42. doi:10.1016/j.colsurfa.2004.05.026.

150. Nakanishi K, Sakiyama T, Imamura K. On the adsorption of proteins on solid surfaces, a common but very complicated phenomenon. *J. Biosci. Bioeng.* 2001;91(3):233-244.

151. Soderquist M., Walton A. Structural changes in proteins adsorbed on polymer surfaces. *J. Colloid Interface Sci.* 1980;75(2):386-397. doi:10.1016/0021-9797(80)90463-4.

152. Sivaraman B, Fears KP, Latour RA. Investigation of the effects of surface chemistry and solution concentration on the conformation of adsorbed proteins using an improved circular dichroism method. *Langmuir ACS J. Surf. Colloids* 2009;25(5):3050-3056. doi:10.1021/la8036814.

153. Hartvig RA, van de Weert M, Østergaard J, Jorgensen L, Jensen H. Protein Adsorption at Charged Surfaces: The role of electrostatic interactions and interfacial charge regulation. *Langmuir* 2011;27(6):2634-2643. doi:10.1021/la104720n.

154. Raffaini G, Ganazzoli F. Surface topography effects in protein adsorption on nanostructured carbon allotropes. *Langmuir ACS J. Surf. Colloids* 2013;29(15):4883-4893. doi:10.1021/la3050779.

155. Gombotz WR, Guanghui W, Horbett TA, Hoffman AS. Protein adsorption to poly(ethylene oxide) surfaces. *J. Biomed. Mater. Res.* 1991;25(12):1547–1562. doi:10.1002/jbm.820251211.

156. Andrade JD, Hlady V, Wei AP. Adsorption of complex proteins at interfaces. *Pure Appl. Chem.* 1992;64(11):1777-1781. doi:10.1351/pac199264111777.

157. Chapman RG, Ostuni E, Takayama S, Holmlin RE, Yan L, Whitesides GM. Surveying for surfaces that resist the adsorption of proteins. *J Am Chem Soc* 2000;122:8303-8304.

158. Scopelliti PE, Borgonovo A, Indrieri M, et al. The effect of surface nanometre-scale morphology on protein adsorption. *PLoS ONE* 2010;5(7):e11862. doi:10.1371/journal.pone.0011862.

159. Rechendorff K, Hovgaard MB, Foss M, Zhdanov VP, Besenbacher F. Enhancement of protein adsorption induced by surface roughness. *Langmuir ACS J. Surf. Colloids* 2006;22(26):10885-10888. doi:10.1021/la0621923.

160. Dunne WM. Bacterial adhesion: Seen any good biofilms lately? *Clin. Microbiol. Rev.* 2002;15(2):155-166. doi:10.1128/CMR.15.2.155-166.2002.

161. Zobell CE. The influence of solid surface on the physiological activities of bacteria in sea water. *J Bacteriol* 1937;33:86.

162. Costerton JW, Lewandowski Z, Caldwell DE, Korber DR, Lappin-Scott HM. Microbial biofilms. *Annu.Rev.Microbiol.* 1995;49:711-745.

163. An YH, Friedman RJ. Laboratory methods for studies of bacterial adhesion. *J. Microbiol. Methods* 1997;30(2):141-152. doi:10.1016/S0167-7012(97)00058-4.

164. Otto M. Staphylococcal infections: mechanisms of biofilm maturation and detachment as critical determinants of pathogenicity. *Annu. Rev. Med.* 2013;64:175-188. doi:10.1146/annurev-med-042711-140023.

165. Busscher HJ, Ploeg RJ, van der Mei HC. SnapShot: Biofilms and biomaterials; mechanisms of medical device related infections. *Biomaterials* 2009;30(25):4247-4248.

166. Rachakonda S, Cartee L. Challenges in antimicrobial drug discovery and the potential of nucleoside antibiotics. *Curr. Med. Chem.* 2004;11(6):775-793.

167. Darouiche RO. Treatment of infections associated with surgical implants. *N. Engl. J. Med.* 2004;350(14):1422-1429. doi:10.1056/NEJMra035415.

168. Zimmerli W, Trampuz A, Ochsner PE. Prosthetic-joint infections. *N. Engl. J. Med.* 2004;351(16):1645-1654. doi:10.1056/NEJMra040181.

169. Fux CA, Costerton JW, Stewart PS, Stoodley P. Survival strategies of infectious biofilms. *Trends Microbiol.* 2005;13(1):34-40. doi:10.1016/j.tim.2004.11.010.

170. Anderson GG, O'Toole GA. Innate and induced resistance mechanisms of bacterial biofilms. *Curr. Top. Microbiol. Immunol.* 2008;322:85-105.

171. Furukawa S, Kuchma SL, O'Toole GA. Keeping their options open: Acute versus persistent infections. *J. Bacteriol.* 2006;188(4):1211-1217. doi:10.1128/JB.188.4.1211-1217.2006.

172. Filloux A, Vallet I. [Biofilm: set-up and organization of a bacterial community]. *Médecine Sci. MS* 2003;19(1):77-83. doi:10.1051/medsci/200319177.

173. Tiller JC, Hartmann L, Scherble J. Reloadable antimicrobial coatings based on amphiphilic silicone networks. *Surf. Coat. Int. Part B Coat. Trans.* 2005;88(1):49-53. doi:10.1007/BF02699707.

174. Lilja M, Forsgren J, Welch K, Astrand M, Engqvist H, Strømme M. Photocatalytic and antimicrobial properties of surgical implant coatings of titanium dioxide deposited though cathodic arc evaporation. *Biotechnol. Lett.* 2012;34(12):2299-2305. doi:10.1007/s10529-012-1040-2.

175. Hendricks DW, Post FJ, Khairnar DR, Jurinak JJ. *Bacterial absorption on soils--Thermodynamics*.; 1970. Available at: http://digitalcommons.usu.edu/water_rep/433/.

176. Stevik TK, Aa K, Ausland G, Hanssen JF. Retention and removal of pathogenic bacteria in wastewater percolating through porous media: a review. *Water Res.* 2004;38(6):1355-1367. doi:10.1016/j.watres.2003.12.024.

177. Katsikogianni M, Missirlis YF. Concise review of mechanisms of bacterial adhesion to biomaterials and of techniques used in estimating bacteria-material interactions. *Eur. Cell. Mater.* 2004;8:37-57.

178. Gabi M, Hefermehl L, Lukic D, Zahn R, Vörös J, Eberli D. Electrical microcurrent to prevent conditioning film and bacterial adhesion to urological stents. *Urol. Res.* 2011;39(2):81-88. doi:10.1007/s00240-010-0284-3.

179. Costerton JW. The etiology and persistence of cryptic bacterial infections: A hypothesis in reviews of infectious diseases. Oxford University Press; 1984.

180. Rode TM, Langsrud S, Holck A, Møretrø T. Different patterns of biofilm formation in Staphylococcus aureus under food-related stress conditions. *Int. J. Food Microbiol.* 2007;116(3):372-383. doi:10.1016/j.ijfoodmicro.2007.02.017.

181. Bellamy WD, Hendricks DW, Logsdon SG. Slow sand filtration: Influences of selected process variables. *J Am Water Well Assoc* 1985;12:62-66.

182. Jucker BA, Harms H, Zehnder AJ. Adhesion of the positively charged bacterium Stenotrophomonas (Xanthomonas) maltophilia 70401 to glass and teflon. *J. Bacteriol.* 1996;178(18):5472-5479.

183. Fattom A, Shilo M. Hydrophobicity as an adhesion mechanism of benthic cyanobacteria. *Appl. Environ. Microbiol.* 1984;47(1):135-143.

184. Mceldowney S, Fletcher M. Effect of growth conditions and surface characteristics of aquatic bacteria on their attachment to solid surfaces. *J. Gen. Microbiol.* 1986;132(2):513-523. doi:10.1099/00221287-132-2-513.

185. Tang P, Zhang W, Wang Y, et al. Effect of superhydrophobic surface of titanium on *Staphylococcus aureus* adhesion. *J. Nanomater.* 2011;2011. doi:10.1155/2011/178921.

186. Sjoblad RD, Doetsch RN. Adsorption of polarly flagellated bacteria to surfaces. *Curr. Microbiol.* 1982;7(3):191-194. doi:10.1007/BF01568974.

187. Adler J. Chemotaxis in bacteria. *Science* 1966;153(3737):708-716.

188. Bain CD, Troughton EB, Tao YT, Evall J, Whitesides GM, Nuzzo RG. Formation of monolayer films by the spontaneous assembly of organic thiols from solution onto gold. *J. Am. Chem. Soc.* 1989;111(1):321-335. doi:10.1021/ja00183a049.

189. Love JC, Estroff LA, Kriebel JK, Nuzzo RG, Whitesides GM. Self-assembled monolayers of thiolates on metals as a form of nanotechnology. *Chem. Rev.* 2005;105(4):1103-1169. doi:10.1021/cr0300789.

190. Rouhana LL, Moussallem MD, Schlenoff JB. Adsorption of short-chain thiols and disulfides onto gold under defined mass transport conditions: Coverage, kinetics, and mechanism. *J. Am. Chem. Soc.* 2011;133(40):16080-16091. doi:10.1021/ja2041833.

191. Majumder C. Adsorption of thiols on the Pd(111) surface: A first principles study. *Langmuir* 2008;24(19):10838-10842. doi:10.1021/la801439q.

192. Carr JA, Wang H, Abraham A, Gullion T, Lewis JP. l-Cysteine interaction with Au_{55} nanoparticle. *J. Phys. Chem. C* 2012;116(49):25816-25823. doi:10.1021/jp308215n.

193. Matthiesen JE, Jose D, Sorensen CM, Klabunde KJ. Loss of hydrogen upon exposure of thiol to gold clusters at low temperature. *J. Am. Chem. Soc.* 2012;134(22):9376-9379. doi:10.1021/ja302339d.

194. Calvente JJ, López-Pérez G, Jurado JM, Andreu R, Molero M, Roldán E. Reorientation of thiols during 2D self-assembly: Interplay between steric and energetic factors. *Langmuir* 2010;26(4):2914-2923. doi:10.1021/la902981n.

195. Cohen-Atiya M, Mandler D. Studying thiol adsorption on Au, Ag and Hg surfaces by potentiometric measurements. *J. Electroanal. Chem.* 2003;550–551:267-276. doi:10.1016/S0022-0728(02)01145-2.

196. Chaki NK, Vijayamohanan K. Self-assembled monolayers as a tunable platform for biosensor applications. *Biosens. Bioelectron.* 2002;17(1–2):1-12. doi:10.1016/S0956-5663(01)00277-9.

197. Michael KE, Vernekar VN, Keselowsky BG, Meredith JC, Latour RA, García AJ. Adsorption-induced conformational changes in fibronectin due to interactions with well-defined surface chemistries. *Langmuir* 2003;19(19):8033-8040. doi:10.1021/la034810a.

198. Ostuni E, Yan L, Whitesides GM. The interaction of proteins and cells with self-assembled monolayers of alkanethiolates on gold and silver. *Colloids Surf. B Biointerfaces* 1999;15(1):3-30. doi:10.1016/S0927-7765(99)00004-1.

199. Chen Z, He Y, Luo S, et al. Label-free colorimetric assay for biological thiols based on ssDNA/silver nanoparticle system by salt amplification. *The Analyst* 2010;135(5):1066-1069. doi:10.1039/b925683k.

200. Jensen GC, Krause CE, Sotzing GA, Rusling JF. Inkjet-printed gold nanoparticle electrochemical arrays on plastic. Application to immunodetection of a cancer biomarker protein. *Phys. Chem. Chem. Phys.* 2011;13(11):4888. doi:10.1039/c0cp01755h.

201. Wilson R. The use of gold nanoparticles in diagnostics and detection. *Chem. Soc. Rev.* 2008;37(9):2028-2045. doi:10.1039/B712179M.

202. Arvizo R, Bhattacharya R, Mukherjee P. Gold nanoparticles: opportunities and challenges in nanomedicine. *Expert Opin. Drug Deliv.* 2010;7(6):753-763. doi:10.1517/17425241003777010.

203. Chen PC, Mwakwari SC, Oyelere AK. Gold nanoparticles: From nanomedicine to nanosensing. *Nanotechnol. Sci. Appl.* 2008;1:45-66.

204. Plateau J. *Experimental and theoretical statics of liquids subject to molecular forces only*.; 1873. Available at: https://www.irphe.fr/~clanet/otherpaperfile/articles/Plateau/Plateau-Eng.pdf.

205. Rayleigh L. On the instability of jets. *Proc. Lond. Math. Soc.* 1878;s1-10(1):4-13. doi:10.1112/plms/s1-10.1.4.

206. Elmqvist R. Measuring instrument of the recording type. 1951. Available at: http://www.freepatentsonline.com/2566443.pdf.

207. Sweet RG. High frequency recording with electrostatically deflected ink jets. *Rev. Sci. Instrum.* 1965;36(2):131. doi:10.1063/1.1719502.

208. Wang Y, Bokor J. Ultra-high-resolution monolithic thermal bubble inkjet print head. *J. MicroNanolithography MEMS MOEMS* 2007;6(4):043009-043009-10. doi:10.1117/1.2816449.

209. How inkjet printers are helping scientists discover new drugs. *Pop. Sci.* 2013. Available at: http://www.popsci.com/science/article/2013-03/how-inkjet-printers-are-helping-scientists-discover-new-drugs.

210. Calvert P. Printing cells. *Science* 2007;318:208-209.

211. Kamyshny A. Metal-based inkjet inks for printed electronics. *Open Appl. Phys. J.* 2011;4(1):19-36. doi:10.2174/1874183501104010019.

212. Komuro N, Takaki S, Suzuki K, Citterio D. Inkjet printed (bio)chemical sensing devices. *Anal. Bioanal. Chem.* 2013;405(17):5785-5805. doi:10.1007/s00216-013-7013-z.

213. Jones N. Science in three dimensions: The print revolution. *Nature* 2012;487(7405):22-23. doi:10.1038/487022a.

214. Yamaguchi S, Ueno A, Akiyama Y, Morishima K. Cell patterning through inkjet printing of one cell per droplet. *Biofabrication* 2012;4(4):045005. doi:10.1088/1758-5082/4/4/045005.

215. Le HP. Progress and trends in ink-jet printing technology. *J. Imaging Sci. Technol.* 1998;42:49-62.

216. Derby B. Bioprinting: inkjet printing proteins and hybrid cell-containing materials and structures. *J. Mater. Chem.* 2008;18(47):5717-5721. doi:10.1039/B807560C.

217. Epson micro piezo technology. Available at: http://www.epson.co.in/sites/epson_india/explore_epson/innovation/epson_micro_piezo_technology.page.

218. Öhlund T, Örtegren J, Forsberg S, Nilsson H-E. Paper surfaces for metal nanoparticle inkjet printing. *Appl. Surf. Sci.* 2012;259:731-739. doi:10.1016/j.apsusc.2012.07.112.

219. Jang D, Kim D, Moon J. Influence of fluid physical properties on ink-jet printability. *Langmuir* 2009;25(5):2629-2635. doi:10.1021/la900059m.

220. Meixner R, Cibis D, Krueger K, Goebel H. Characterization of polymer inks for drop-on-demand printing systems. *Microsyst. Technol.* 2008;14(8):1137-1142. doi:10.1007/s00542-008-0639-7.

221. McKinley GH, Renardy M. Wolfgang von Ohnesorge. *Phys. Fluids* 2011;23(12):127101. doi:10.1063/1.3663616.

222. Dimatix directions.indd - Dimatix tutorial.pdf. Available at: http://seeen.spidergraphics.com/cnf5/doc/Dimatix%20tutorial.pdf. Accessed August 12, 2013.

223. Gómez AM. A historical essay on the development of flexography. 2000. Available at: https://ritdml.rit.edu/handle/1850/14139.

224. *The future of flexographic printing to 2016*. Available at: http://www.google.fi/url?sa=t&rct=j&q=flexo%20to%202016&source=web&cd=4&ved=0CDgQFjAD&url=http%3A%2F%2Fwww.smitherspira.com%2Fcore%2Fdownloaddoc.aspx%3Fdocumentid%3D10874&ei=6NNiULKOD_P14QSJk4HgAQ&usg=AFQjCNHwRCEr65hQIc2jn711tV0Q6QMZFQ&cad=rja.

225. Harris D. *HD flexo - Quality on qualified plates*.; 2009. Available at: http://www.monochrom.gr/UserFiles/HD_Flexo___Quality_on_Qualified_Plates_v5.pdf.

226. Søndergaard RR, Hösel M, Krebs FC. Roll-to-roll fabrication of large area functional organic materials. *J. Polym. Sci. Part B Polym. Phys.* 2013;51(1):16-34. doi:10.1002/polb.23192.

227. Krebs FC, Fyenbo J, Jørgensen M. Product integration of compact roll-to-roll processed polymer solar cell modules: methods and manufacture using flexographic printing, slot-die coating and rotary screen printing. *J. Mater. Chem.* 2010;20(41):8994. doi:10.1039/c0jm01178a.

228. Yu J-S, Kim I, Kim J-S, et al. Silver front electrode grids for ITO-free all printed polymer solar cells with embedded and raised topographies, prepared by thermal imprint, flexographic and inkjet roll-to-roll processes. *Nanoscale* 2012;4(19):6032-6040. doi:10.1039/C2NR31508D.

229. Tobjörk D, Österbacka R. Paper Electronics. *Adv. Mater.* 2011;23(17):1935–1961. doi:10.1002/adma.201004692.

230. Sangoi R, Smith CG, Seymour MD, et al. Printing radio frequency identification (RFID) tag antennas using inks containing silver dispersions. *J. Dispers. Sci. Technol.* 2004;25(4):513-521. doi:10.1081/DIS-200025721.

231. Ewins R. Proto-Polynesian art? The cliff paintings of Vatulele, Fiji. *J. Polyn. Soc.* 1995;104:23-74.

232. Savage J. Factors affecting the quality of screen-printed conductors. *Thin Solid Films* 1969;4(2):137-148. doi:10.1016/0040-6090(69)90044-3.

233. Fleck I, Chouta P. A new dimension in stencil print optimization. *J. SMT* 2003;16(1):24-33.

234. Cao K, Cheng K, Wang Z. Optimization of screen printing process. In: *7th International Conference on Electronic Packaging Technology, 2006. ICEPT '06*.; 2006:1 -4. doi:10.1109/ICEPT.2006.359881.

235. Yen Y-T, Fang T-H, Lin Y-C. Optimization of screen-printing parameters of SN9000 ink for pinholes using Taguchi method in chip on film packaging. *Robot Comput-Integr Manuf* 2011;27(3):531–537. doi:10.1016/j.rcim.2010.09.008.

236. Guilbault GG, Lubrano GJ, Gray DN. Glass-metal composite electrodes. *Anal. Chem.* 1973;45:2255-2258.

237. Jabbour GE, Radspinner R, Peyghambarian N. Screen printing for the fabrication of organic light-emitting devices. *IEEE J. Sel. Top. Quantum Electron.* 2001;7(5):769 -773. doi:10.1109/2944.979337.

238. The Yasui Seiki " Micro Gravure™ " Coating Method. Available at: http://www.yasui.com/2004/MicroGravure.pdf.

239. Johansson K, Lundberg P, Ryberg R. *A Guide to graphic print production*. John Wiley & Sons; 2011.

240. D Antonio P, Lasalvia M, Perna G, Capozzi V. Scale-independent roughness value of cell membranes studied by means of AFM technique. *Biochim. Biophys. Acta BBA - Biomembr.* 2012;1818(12):3141-3148. doi:10.1016/j.bbamem.2012.08.001.

241. Whitehouse DJ. *Handbook of surface and nanometrology*. 2 nd. Boca Raton, FL: CRC Press; 2011.

242. Järnström J. Topography and wetting of pigment coated substrates. 2010.

243. Fubel A, Zech M, Leiderer P, Klier J, Shikin V. Analysis of roughness of Cs surfaces via evaluation of the autocorrelation function. *Surf. Sci.* 2007;601(7):1684-1692. doi:10.1016/j.susc.2007.01.040.

244. Järnström J, Ihalainen P, Lemström A, Toivakka M, Peltonen J. The influence of different roughness scales of pigment coated papers on print gloss. *Nord. Pulp Pap. Res. J.* 2009;24(3):327-334.

245. Bietsch A, Michel B. Conformal contact and pattern stability of stamps used for soft lithography. *J. Appl. Phys.* 2000;88:4310-4318.

246. Robertson GL. Food packaging: Principles and practice, Third Edition. CRC Press; 2012.

247. Woodward RP. *Contact angle measurements using the drop shape method*. Available at: http://web.engr.oregonstate.edu/~rochefsk/MSI%20CH%20668/Polymer%20Labs/Contact%20Angle%20Analysis%20FTA/ContactAngleMeasurements.pdf.

248. Young T. An essay on the cohesion of fluids. *Philos. Trans. R. Soc. Lond.* 1805;95:65-87. doi:10.1098/rstl.1805.0005.

249. Owens DK, Wendt RC. Estimation of the surface free energy of polymers. *J. Appl. Polym. Sci.* 1969;13(8):1741–1747. doi:10.1002/app.1969.070130815.

250. Kaelble DH. Dispersion-polar surface tension properties of organic solids. *J. Adhes.* 1970;2(2):66-81. doi:10.1080/0021846708544582.

251. Girifalco LA, Good RJ. A Theory for the estimation of surface and interfacial energies. I. Derivation and application to interfacial tension. *J. Phys. Chem.* 1957;61(7):904-909. doi:10.1021/j150553a013.

252. Janssen D, De Palma R, Verlaak S, Heremans P, Dehaen W. Static solvent contact angle measurements, surface free energy and wettability determination of various self-assembled

monolayers on silicon dioxide. *Thin Solid Films* 2006;515(4):1433-1438. doi:10.1016/j.tsf.2006.04.006.

253. Wenzel R. Resistance of solid surfaces to wetting by water. *Ind. Eng. Chem.* 1936;28(8):988-994.

254. Peltonen J, Järn M, Areva S, Linden M, Rosenholm JB. Topographical parameters for specifying a three-dimensional surface. *Langmuir ACS J. Surf. Colloids* 2004;20(22):9428-9431. doi:10.1021/la0400252.

255. Van Oss CJ, Chaudhury MK, Good RJ. Monopolar surfaces. *Adv. Colloid Interface Sci.* 1987;28(C):35-64.

256. Van Oss CJ, Chaudhury MK, Good RJ. Interfacial Lifshitz-van der Waals and polar interactions in macroscopic systems. *Chem Rev* 1988;88(6):927-941. doi:10.1021/cr00088a006.

257. Bollström R, Pettersson F, Dolietis P, Preston J, Österbacka R, Toivakka M. Impact of humidity on functionality of on-paper printed electronics. *Nanotechnology* 2014;25:094003.

258. *Learning by Doing - Schools Experiments with Wacker-Products*. Wacker Silicones; 2004:pp. 42. Available at: http://technology5.net/l/learning-by-doing-school-experiments-with-wacker-silicones-w2017.html.

259. DEHESIVE® 920; Functional Silicone Polymers. Available at: http://www.wacker.com/cms/en/products-markets/products/product.jsp?product=8989&country=FI&language=en.

260. SpecialChem; Adhesives sealants formulation; Mowiol® 10-98. Available at: http://www.specialchem4adhesives.com/tds/selector/additives/15066/index.aspx?did=1&lr=google&gclid=COzfk6f04bsCFURc3godyVAABQ.

261. Matilainen K, Hämäläinen T, Savolainen A, et al. Performance and penetration of laccase and ABTS inks on various printing substrates. *Colloids Surf. B Biointerfaces* 2012;90:119-128. doi:10.1016/j.colsurfb.2011.10.015.

262. Hostetler MJ, Wingate JE, Zhong C-J, et al. Alkanethiolate gold cluster molecules with core diameters from 1.5 to 5.2 nm: Core and monolayer properties as a function of core size. *Langmuir* 1998;14(1):17-30. doi:10.1021/la970588w.

263. Binnig, Quate, Gerber. Atomic force microscope. *Phys. Rev. Lett.* 1986;56(9):930-933.

264. Binnig G. Atomic force microscope and method for imaging surfaces with atomic resolution. 1986.

265. Binnig G, Rohrer H, Gerber C, Weibel E. Surface studies by scanning tunneling microscopy. *Phys. Rev. Lett.* 1982;49(1):57-61. doi:10.1103/PhysRevLett.49.57.

266. García R, Pérez R. Dynamic atomic force microscopy methods. *Surf. Sci. Rep.* 2002;47(6-8):197-301. doi:10.1016/S0167-5729(02)00077-8.

267. Young TJ, Monclus MA, Burnett TL, Broughton WR, Ogin SL, Smith PA. The use of the PeakForceTM quantitative nanomechanical mapping AFM-based method for high-resolution Young's modulus measurement of polymers. *Meas. Sci. Technol.* 2011;22(12):125703. doi:10.1088/0957-0233/22/12/125703.

268. Adamcik J, Berquand A, Mezzenga R. Single-step direct measurement of amyloid fibrils stiffness by peak force quantitative nanomechanical atomic force microscopy. *Appl. Phys. Lett.* 2011;98(19):193701. doi:10.1063/1.3589369.

269. Merrett K, Cornelius RM, McClung WG, Unsworth LD, Sheardown H. Surface analysis methods for characterizing polymeric biomaterials. *J. Biomater. Sci. Polym. Ed.* 2002;13(6):593-621.

270. Bollström R, Tobjörk D, Dolietis P, et al. Reel to reel printed transistors on multilayer curtain coated paper. In: *ECS 11 Proceedings*. Turku, Finland; 2011:66-69.

271. Bollström R, Tobjörk D, Dolietis P, et al. Printability of functional inks on multilayer curtain coated paper. *Chem. Eng. Process. Process Intensif.* 2013;68:13-20. doi:10.1016/j.cep.2012.07.007.

272. Bollström R. Paper for printed electronics and functionality. 2013. Available at: http://www.doria.fi/bitstream/handle/10024/92181/bollstrom_roger.pdf?sequence=2.

273. Kang JF, Jordan R, Ulman A. Wetting and Fourier transform infrared spectroscopy studies of mixed self-assembled monolayers of 4′-methyl-4-mercaptobiphenyl and 4′-hydroxy-4-mercaptobiphenyl. *Langmuir* 1998;14:3983-3985.

274. Chibowski E, Staszczuk P. Determination of surface free energy of kaolinite. *Clays Clay Miner.* 1988;36(5):455-461.

275. Yang Y-C, Jeong S-B, Yang S-Y, Chae Y-B, Kim H-S. The changes in surface properties of the calcite powder with stearic acid treatment. *Mater. Trans.* 2009;50:695-701.

276. Tegethoff FW, Rohleder JW, Kroker E. Calcium carbonate: From the cretaceous period into the 21st century. Springer; 2001.

277. Backfolk K, Lagerge S, Rosenholm JB. The influence of stabilizing agents on the interaction between styrene/butadiene latex and calcium carbonate: a calorimetric and a dynamic electrokinetic study. *J. Colloid Interface Sci.* 2002;254(1):8-16.

278. Juvonen H, Määttänen A, Ihalainen P, Peltonen J. Modification of surface properties of latex coatings for enhanced print quality of silver nanoparticle ink. In: *Poster Presentation*. Malmö, Sweden; 2012.

279. Cole M, Hiralal P, Ying K, et al. Dry-Transfer of Aligned Multiwalled Carbon Nanotubes for Flexible Transparent Thin Films. *J. Nanomater.* 2012;2012. doi:10.1155/2012/272960.

280. Mori YH, van de Ven TGM, Mason SG. Resistance to spreading of liquids by sharp edged microsteps. *Colloids Surf.* 1982;4(1):1-15. doi:10.1016/0166-6622(82)80085-1.

281. Timoshevskii V, Ke Y, Guo H, Gall D. The influence of surface roughness on electrical conductance of thin Cu films: An ab initio study. *J. Appl. Phys.* 2008;103(11):113705. doi:10.1063/1.2937188.

282. Shin K-Y, Lee S-H, Oh JH. Solvent and substrate effects on inkjet-printed dots and lines of silver nanoparticle colloids. *J. Micromechanics Microengineering* 2011;21(4):045012. doi:10.1088/0960-1317/21/4/045012.

283. Määttänen A, Ihalainen P, Majumdar H, et al. Printed gold nanoparticle-based electrodes on paper. In: *Poster Presentation*. Malmö, Sweden; 2012.

284. Nur HM, Song JH, Evans JRG, Edirisinghe MJ. Ink-jet printing of gold conductive tracks. *J. Mater. Sci. Mater. Electron.* 2002;13:213-219.

285. R. Samarasinghe S, Pastoriza-Santos I, Edirisinghe MJ, et al. Electric-jet assisted layer-by-layer deposition of gold nanoparticles to prepare conducting tracks. *Nat. Sci.* 2009;01(02):142-150. doi:10.4236/ns.2009.12018.

286. Lazar MA. *Let's review: Physics-- the physical setting*. Barron's educational series; 2004.

287. Lide DR. *Handbook of chemistry and physics*. 75th ed. New York: CRC Press; 1996.

288. Elsom KC, Sambles JR. Macroscopic surface roughness and the resistivity of thin metal films. *J. Phys. F Met. Phys.* 1981;11(3):647. doi:10.1088/0305-4608/11/3/012.

289. Jakobovic M, ed. *Silver nanoparticles*. Croatia: In-Teh; 2010. Available at: http://www.zums.ac.ir/files/research/site/ebooks/Nanotechnology%20and%20Nanomaterials/Silver%20Nanoparticles.pdf.

290. Asoro M, Damiano J, Ferreira P. Size effects on the melting temperature of silver nanoparticles: In-situ TEM observations. *Microsc. Microanal.* 2009;15(Supplement S2):706-707. doi:10.1017/S1431927609097013.

291. Buffat P, Borel J-P. Size effect on the melting temperature of gold particles. *Phys. Rev. A* 1976;13(6):2287-2298. doi:10.1103/PhysRevA.13.2287.

292. Gupta A, Mandal S, Katiyar M, Mohapatra YN. Film processing characteristics of nano gold suitable for conductive application on flexible substrates. *Thin Solid Films* 2012;520(17):5664-5670. doi:10.1016/j.tsf.2012.04.017.

293. Broad Ion Beam Cross Sectioning. Available at: http://www.topanalytica.com/files/160/Broad_Ion_Beam_Cross_Sectioning.pdf.

294. Rogers B, Manning L, Sulchek T, Adams J. Improving tapping mode atomic force microscopy with piezoelectric cantilevers. *Ultramicroscopy* 2004;100(3-4):267-276. doi:10.1016/j.ultramic.2004.01.016.

295. Moazzez B, O'Brien SM, Merschrod S. EF. Improved adhesion of gold thin films evaporated on polymer resin: Applications for sensing surfaces and MEMS. *Sensors* 2013;13(6):7021-7032. doi:10.3390/s130607021.

296. Deiss F, Mazzeo A, Hong E, Ingber DE, Derda R, Whitesides GM. Platform for high-throughput testing of the effect of soluble compounds on 3D cell cultures. *Anal. Chem.* 2013;85(17):8085-8094. doi:10.1021/ac400161j.

297. Barbieri L, Wagner E, Hoffmann P. Water wetting transition parameters of perfluorinated substrates with periodically distributed flat-top microscale obstacles. *Langmuir* 2007;23(4):1723-1734. doi:10.1021/la0617964.

298. Aizenberg J, Black AJ, Whitesides GM. Controlling local disorder in self-assembled monolayers by patterning the topography of their metallic supports. *Nature* 1998;394(6696):868-871. doi:10.1038/29730.

299. Tlili A, Abdelghani A, Hleli S, Maaref MA. Electrical characterization of a thiol SAM on gold as a first step for the fabrication of immunosensors based on a quartz crystal microbalance. *Sensors* 2004;4(6):105-114. doi:10.3390/s40670105.

300. Ferreira VC, Silva F, Abrantes LM. Electrochemical and STM study of α, ω-alkanedithiols self-assembled monolayers. *Chem Biochem Eng Q* 2009;23:99-106.

301. Ihalainen P, Majumdar H, Viitala T, et al. Application of paper-supported printed gold electrodes for impedimetric immunosensor development. *Biosensors* 2012;3(1):1-17. doi:10.3390/bios3010001.

302. Kadara RO, Jenkinson N, Banks CE. Characterisation of commercially available electrochemical sensing platforms. *Sens. Actuators B Chem.* 2009;138(2):556-562. doi:10.1016/j.snb.2009.01.044.

303. Moulton S., Barisci J., Bath A, Stella R, Wallace G. Studies of double layer capacitance and electron transfer at a gold electrode exposed to protein solutions. *Electrochimica Acta* 2004;49(24):4223-4230. doi:10.1016/j.electacta.2004.03.034.

304. Heinze J, Frontana-Uribe BA, Ludwigs S. Electrochemistry of conducting polymers—Persistent models and new concepts†. *Chem. Rev.* 2010;110(8):4724-4771. doi:10.1021/cr900226k.

305. Mendonça G, Mendonça DBS, Aragão FJL, Cooper LF. Advancing dental implant surface technology–from micron- to nanotopography. *Biomaterials* 2008;29(28):3822-3835. doi:10.1016/j.biomaterials.2008.05.012.

306. Hannig M, Hannig C. Nanomaterials in preventive dentistry. *Nat. Nanotechnol.* 2010;5(8):565-569. doi:10.1038/nnano.2010.83.

307. Geetha M, Singh AK, Asokamani R, Gogia AK. Ti based biomaterials, the ultimate choice for orthopaedic implants – A review. *Prog. Mater. Sci.* 2009;54(3):397-425. doi:10.1016/j.pmatsci.2008.06.004.

308. Brunette DM, Tengvall P, Textor M, Thomsen P. Titanium in medicine: Material science, surface science, engineering, biological responses, and medical applications. Springer; 2001.

309. Singh AV, Vyas V, Salve TS, et al. Biofilm formation on nanostructured titanium oxide surfaces and a micro/nanofabrication-based preventive strategy using colloidal lithography. *Biofabrication* 2012;4(2):025001. doi:10.1088/1758-5082/4/2/025001.

310. Fallarero A, Skogman M, Kujala J, et al. (+)-Dehydroabietic acid, an abietane-type diterpene, inhibits *Staphylococcus aureus* biofilms in vitro. *Int. J. Mol. Sci.* 2013;14(6):12054-12072. doi:10.3390/ijms140612054.

311. Sen DK, Sarin GS. Tear glucose levels in normal people and in diabetic patients. *Br. J. Ophthalmol.* 1980;64(9):693-695.

312. American Diabetes Association. Diagnosis and classification of diabetes mellitus. *Diabetes Care* 2009;33(Supplement_1):S62-S69. doi:10.2337/dc10-S062.

313. Davidson JK, ed. Clinical diabetes mellitus: A problem-oriented approach. New York: Thieme; 2000.

314. Clark Jr. LC, Lyons C. Electrode systems for continuous monitoring in cardiovascular surgery. *Ann. N. Y. Acad. Sci.* 1962;102(1):29-45. doi:10.1111/j.1749-6632.1962.tb13623.x.

315. Gough DA, Kumosa LS, Routh TL, Lin JT, Lucisano JY. Function of an implanted tissue glucose sensor for more than 1 year in animals. *Sci. Transl. Med.* 2010;2(42):42ra53-42ra53. doi:10.1126/scitranslmed.3001148.

316. AWARD - Health Care: C8 MediSensors' glucose monitor eliminates needle from daily blood testing - Silicon Valley Business Journal. Available at: http://www.bizjournals.com/sanjose/print-edition/2012/02/17/c8-medisensors-glucose-monitor.html?page=all. Accessed September 5, 2013.

317. Guo D, Zhang D, Li N. Monitor blood glucose levels via breath analysis system and sparse representation approach. In: *2010 IEEE Sensors*.; 2010:1238-1241. doi:10.1109/ICSENS.2010.5690611.

318. Yu J, Ge L, Dai P, Ge S, Liu S. A novel enzyme biosensor for glucose based on rhodanine derivative chemiluminescence system and mesoporous hollow silica microspheres receptor. *Biosens. Bioelectron.* 2010;25(9):2065-2070. doi:10.1016/j.bios.2010.02.001.

319. Odebunmi EO, Owalude SO. Kinetic and thermodynamic studies of glucose oxidase catalysed oxidation reaction of glucose. *J. Appl. Sci. Environ. Manag.* 2007;11:95-100. doi:ja07103.

320. Wilson R, Turner APF. Glucose oxidase: an ideal enzyme. *Biosens. Bioelectron.* 1992;7(3):165-185. doi:10.1016/0956-5663(92)87013-F.

321. Keilin D, Hartree EF. Specificity of glucose oxidase (notatin). *Biochem. J.* 1952;50(3):331-341.

322. Yu J, Yu D, Zhao T, Zeng B. Development of amperometric glucose biosensor through immobilizing enzyme in a Pt nanoparticles/mesoporous carbon matrix. *Talanta* 2008;74(5):1586-1591. doi:10.1016/j.talanta.2007.10.005.

323. Fabiano S, Tran-Minh C, Piro B, Dang LA, Pham MC, Vittori O. Poly 3,4-ethylenedioxythiophene as an entrapment support for amperometric enzyme sensor. *Mater. Sci. Eng. C* 2002;21(1-2):61-67. doi:10.1016/S0928-4931(02)00060-7.

324. Etchison JR, Freeze HH. Enzymatic assay of D-mannose in serum. *Clin. Chem.* 1997;43(3):533-538.

325. Cui G, Kim SJ, Choi SH, Nam H, Cha GS, Paeng K-J. A Disposable amperometric sensor screen printed on a nitrocellulose strip: A glucose biosensor employing lead oxide as an interference-removing agent. *Anal. Chem.* 2000;72(8):1925-1929. doi:10.1021/ac991213d.

326. Santhiago M, Kubota LT. A new approach for paper-based analytical devices with electrochemical detection based on graphite pencil electrodes. *Sens. Actuators B Chem.* 2013;177:224-230. doi:10.1016/j.snb.2012.11.002.

327. Gold disk electrode. *EDAQ Data Rec. Made Simple*. Available at: http://www.edaq.com/ET076-1_Gold-Disk-Electrode.

Åbo Akademis förlag | ISBN 978-952-12-3119-3